

THESIS FOR THE DEGREE OF LICENTIATE OF ENGINEERING

**Time series of mesospheric species  
measured using ground-based microwave  
spectrometry: Retrieval and Error  
estimation**

Ole Martin Christensen



Department of Earth and Space Sciences  
**CHALMERS UNIVERSITY OF TECHNOLOGY**  
Gothenburg, Sweden 2013

**Time series of mesospheric species measured using ground-based microwave spectrometry: Retrieval and Error estimation**

Ole Martin Christensen

© Ole Martin Christensen, 2013.

Technical Report 54L,  
Department of Earth and Space Sciences  
Global Environmental Measurements and Modelling  
Chalmers University of Technology  
SE - 412 96 Gothenburg, Sweden  
Phone + 46 (0)31 772 1000

Printed by Chalmers Reproservice  
Chalmers University of Technology  
Gothenburg, Sweden 2013



The text of this work is licensed under a Creative Commons Attribution 3.0 Unported License. All pictures and figures are property of their respective owners.

Cover: Left: Temporal averaging kernels from the 22 GHz radiometer at the Onsala Space Observatory. Right: Mean difference between the CO concentration measured by the 115 GHz radiometer at the Onsala Space Observatory and four satellite instruments. Both figures are taken from the two papers appended to this thesis.

# **Time series of mesospheric species measured using ground-based microwave spectrometry: Retrieval and Error estimation**

Ole Martin Christensen

Department of Earth and Space Sciences

Chalmers University of Technology

## **Abstract**

As the human emission of greenhouse gases continue to increase, the atmosphere is changing. The mesosphere region is particularly interesting as the magnitude of temperature change in this region is expected to be larger, than in the lower layers of the atmosphere. However, there is still much uncertainty related to the long-term effects of these changes. It is therefore important to have instruments that can provide long-term monitoring of the dynamics and chemistry of the middle atmosphere.

Species with long photochemical lifetime can be used to study the dynamics of the mesosphere. At the Onsala Space Observatory two such species, CO and H<sub>2</sub>O, have been measured over a number of years with microwave spectrometers. These instruments can provide us with continuous measurements of the mesosphere over long time periods. This thesis concerns characterising and improving the measurements and retrievals from the two microwave spectrometers.

This thesis puts forth a possible improvement in the inversion algorithm used for retrieving time-series from ground-based microwave spectrometers. By using a two dimensional retrieval method, the inversions can take into account the temporal correlation of the atmospheric state. The new method was tested on the 22 GHz spectrometer measuring mesospheric water vapour at OSO. The result is a more flexible retrieval that removes the problem of ad-hoc selecting data averaging times before performing an inversion. An additional improvement offered by the new method is the ability to consistently interpolate the retrieved data in order to close measurement gaps or re-grid the data.

The thesis also compares a six year long time series of mesospheric CO from the 115 GHz spectrometer at OSO to measurements from contemporary satellite instruments. The systematic errors of the instrument are estimated to  $\pm 40\%$  from 2002-2004 and  $\pm 20\%$  from 2004-2008. Compared to the satellite measurements, the measurements from the OSO radiometer have a mean difference of less than or equal to 25%. This is consistent with the combined systematic errors of both the ground-based and satellite instruments.

The thorough error characterisation, and the improved retrieval method, presented in this thesis ensure that the data produced by the microwave spectrometers at OSO remain relevant and important for the future study of the middle atmosphere.

**Keywords:** remote sensing, mesosphere, retrieval, microwave spectrometry, carbon monoxide, water vapour

---

## APPENDED PAPERS

---

The thesis is based on the following articles:

- P. Forkman, O.M. Christensen, P. Eriksson, J. Urban, B. Funke. Six years of mesospheric CO estimated from ground-based frequency-switched microwave radiometry at 57° N compared with satellite instruments *Atmos. Meas. Tech.*, 5, 2827-2841, doi:10.5194/amt-5-2827-2012, 2012.
- O.M. Christensen, P. Eriksson. Time series inversion of spectra from ground-based spectrometers *Atmos. Meas. Tech.*, submitted, 2012.

---

# CONTENTS

---

CHAPTER 1 – INTRODUCTION	1
1.1 Observing the earth . . . . .	1
1.2 The current state of earth observation . . . . .	2
CHAPTER 2 – ATMOSPHERE	5
2.1 The vertical structure of the atmosphere . . . . .	5
2.2 General Circulation . . . . .	6
2.3 The changing middle atmosphere . . . . .	8
2.4 The chemistry of mesospheric CO . . . . .	9
CHAPTER 3 – MEASUREMENT PRINCIPLES	11
3.1 Blackbody radiation . . . . .	11
3.2 Absorption and emission from gases . . . . .	13
3.3 The radiative transfer equation . . . . .	14
3.4 Retrieval . . . . .	15
3.5 Limitations of an retrieval . . . . .	19
3.6 Instrumental error sources . . . . .	21
CHAPTER 4 – INSTRUMENTS	22
4.1 The microwave spectrometer . . . . .	22
4.2 Calibration . . . . .	23
4.3 The old CO radiometer at OSO . . . . .	26
4.4 The water vapour radiometer at OSO . . . . .	26
4.5 Satellites instruments . . . . .	27
CHAPTER 5 – SUMMARY AND OUTLOOK	29
5.1 Summary Paper A . . . . .	29
5.2 Summary Paper B . . . . .	29
5.3 Outlook . . . . .	30
REFERENCES	33
PAPER A	36
PAPER B	52

---

# ACKNOWLEDGMENTS

---

First I would like to thank my main supervisor Prof. Patrick Eriksson and my co-supervisor Peter Forkman for providing challenging tasks, interesting opportunities and helpful advice whenever needed. Furthermore, I thank Prof. Donal Murtagh for giving me the opportunity to be a PhD student at the department of Earth and Space Sciences, as well as always being kind and supportive.

A special thanks to my fellow students Marston Johnston, Kazutoshi Sagi, Maryam Khosravi for all the help, laughs, and interesting discussions you have provided me with over the last two and a half years. I thank my two office mates, Mathias Andersson and Johan Lodin, for surviving my humming and thinking out loud over the course of this thesis work.

Finally, I want to thank the Swedish taxpayers for understanding the importance of basic science and funding my work.

---

# CHAPTER 1

---

## Introduction

The study of the atmosphere dates back to the ancient civilisations. The Greeks wrote theses on empirical weather prediction and introduced such popular rules as *Red sky at night, sailor's delight*. During the middle ages the Muslim astronomer Ibn Al-Haitham estimated the height of the atmosphere to 79 km from his studies of scattered light at twilight, an impressive feat considering the limited instrumentation available [Frisinger, 1973].

Today we have a myriad of observation methods reaching from worldwide coordinated weather balloons launches, research instruments on balloons and rockets, to satellites orbiting the earth. Data from these instruments are processed using powerful computers, used in advanced weather prediction models, and compared to climate models. Despite of this the atmosphere still offers unanswered scientific questions, and as the evidence of human influence on climate becomes ever clearer, our need for understanding the atmosphere has never been greater.

### 1.1 Observing the earth

We all have the ability to make observations of the atmosphere, and we do so every day by staring at clouds or enjoying a beautiful sunset. For detailed atmospheric science, however, a range of sensors and platforms have been developed. In earth observations we differentiate between two types of measurement techniques. In-situ measurements samples the atmosphere directly at the desired position, whereas in remote sensing electromagnetic (EM) radiation is used to gather information about the atmosphere, possibly far away from the position of the instrument. An overview of some of different remote sensing instrument platforms is shown in figure 1.1. Each instrument platform has its advantages and disadvantages, and depending on the phenomenon studied, one particular system, or combination of systems, is advantageous. This thesis will focus on the middle atmosphere, which is the atmosphere between roughly 10 to 100 km, and instruments designed for studying this part of the atmosphere are thus of particular interest.

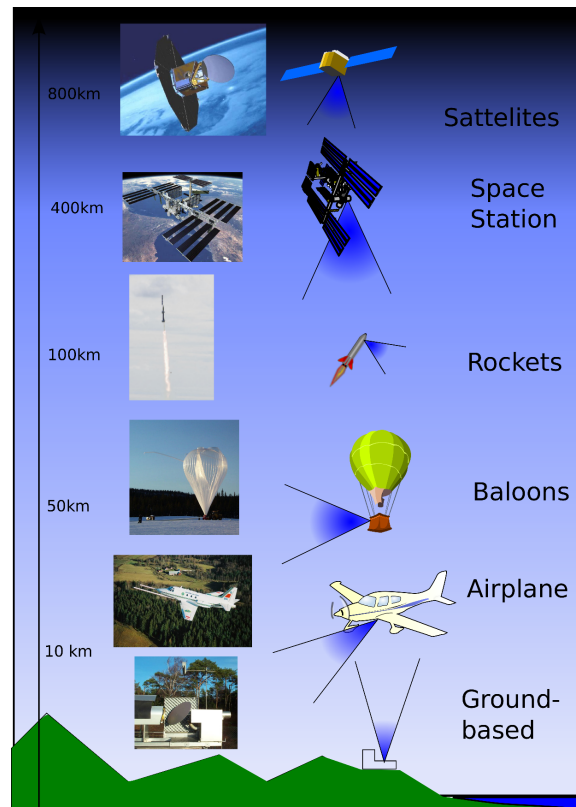


**Figure 1.1:** Overview of instrument platforms used for studying the atmosphere. The altitudes for the different platforms are approximate.

Ground-based instruments used to study the middle atmosphere include UV-, IR-, and microwave spectrometers, lidars and radars. These are located on the ground and look upwards into the atmosphere. These instruments are usually cheaper and easier to maintain than similar instruments on other platforms. This means that they have the possibility to continuously measure and monitor the atmosphere above a specific location over long time periods. Their main limitation is that the instruments cover a limited geographic area, compared to air-borne or satellite-borne instruments.

On the opposite side of the scale are instruments orbiting the planet on space-stations or satellites. These provide the ultimate geographical coverage as they, in principle, can measure the entire globe. In practice however, their geographical coverage is limited by orbit and type of instrument. Satellite-borne instruments that use an orbit designed to give global coverage, will lack in the ability to measure local or short term transient phenomena.

## 1.2 The current state of earth observation

One of the most pressing scientific questions in atmospheric science is the determination of the magnitude of, and reasons for, long term changes in the atmosphere.

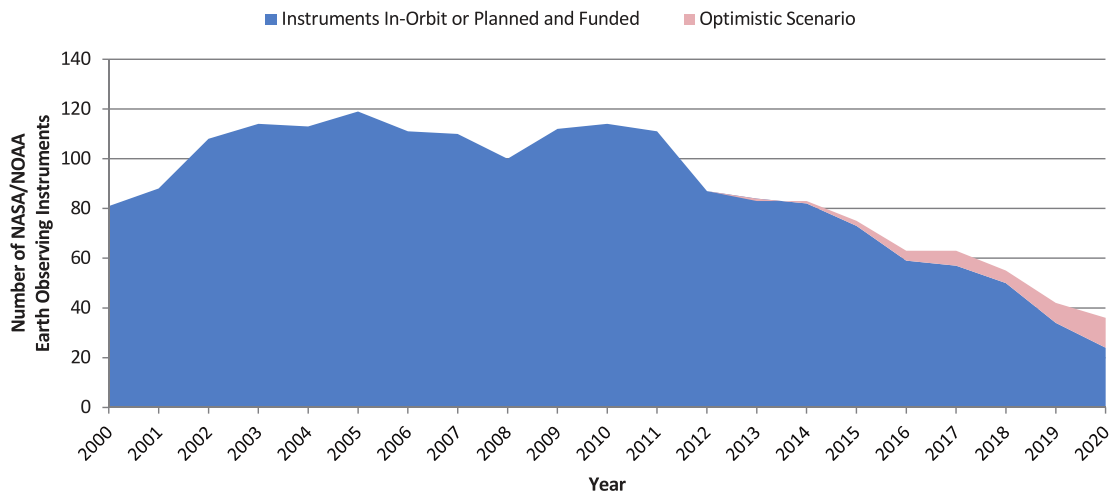


**Figure 1.2:** Number of future earth observing instruments from NASA and NOAA. The two curves represent two different funding scenarios, with the red being the most optimistic [Committee on the Assessment of NASA’s Earth Science Program et al., 2012].

To investigate such changes, global long term measurements are needed. Satellite systems have global coverage, but unfortunately these systems have inherently short lifetimes as repairing them is impossible once something goes wrong.

The last 10 years, scientists interested in the middle atmosphere have been fortunate as numerous satellites launched to study it in the early 2000s have exceeded their life expectancy multiple times. This has allowed accurate multi-instrument assessments of phenomena and trends in the middle atmosphere (e.g. Hegglin and Tegtmeier [2011]).

With the “death” of ENVISAT, the largest European earth observing satellite in April 2012, this “golden era” seems to be going towards an end. Ideally replacement satellites should have been launched to provide overlapping measurements, but rather the opposite is happening. Figure 1.2 shows the expected number of future earth observing satellite instruments from NASA and NOAA. A sharp decline can be seen after 2011. Though this is not the whole picture, it is telling that in a world where knowledge about the earth system is ever more important, our ability to measure it is declining rapidly.

With the loss off continuity in satellite measurements, our ability to distinguish between long term climate changes and short term variations will be severely hampered. Ground-based instruments offer an alternative set of measurements that can be used to study the middle atmosphere. The Network for the Detection of Atmospheric Composition Change (NDACC) is an organisation that works with coordinating ground-based measurements to create a global database of atmospheric data. Figure 1.3 shows the more than 70 remote sensing research stations contributing to the network. Though the network was originally founded to the study long term

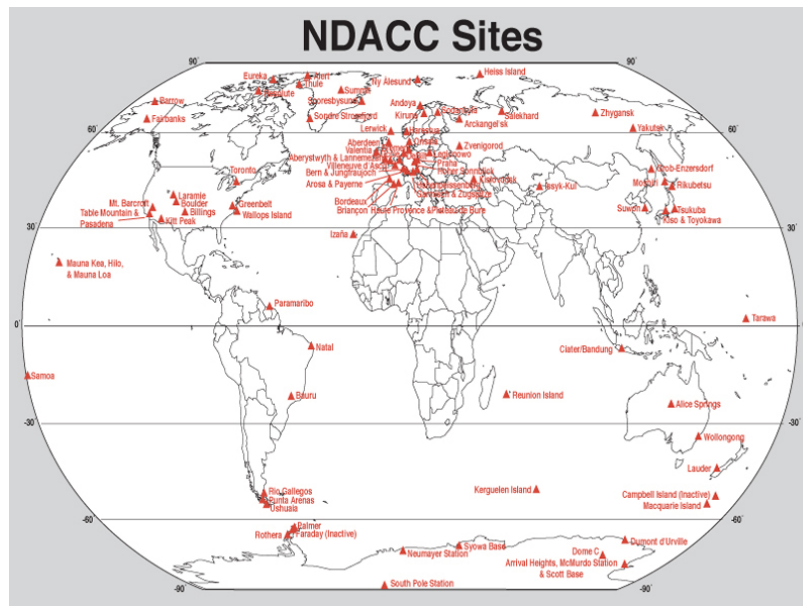


**Figure 1.3:** An overview of the stations in the NDACC network. [NDACC]

changes in the ozone layer, its mission has broadened to detection of trends in overall atmospheric composition, and understanding of their impact on the atmosphere [NDACC]. The advantage of combining data from several independent ground-based instruments using different methods is that it offers a redundancy and robustness that is hard to achieve with satellite instruments due to their high cost and limited numbers.

To ensure the quality of measurement databases, it is important that the data from the instruments are analysed in a consistent matter, and that the uncertainties and errors are well characterised. The two articles, on which this thesis is based, focus on these two problems. The first paper, “Six years of mesospheric CO estimated from ground-based frequency-switched microwave radiometry at 57° N compared with satellite instruments”, provides a thorough error analysis of the ground based microwave radiometer measuring carbon monoxide above Onsala Space Observatory (OSO). The second paper, “Time series inversion of spectra from ground-based spectrometers”, presents a novel way of extracting time series from measurement data. By including temporal averaging directly into the retrieval algorithm, we remove need for a single instrument to have multiple datasets to cover different altitudes. The method simplifies validation of measurements from the instrument, and makes comparisons between instruments easier.

The first part of this thesis will provide the reader with the background knowledge needed to understand the methods, results and significance of the two papers, whereas the second part will present the two aforementioned research articles.

---

## CHAPTER 2

---

# Atmosphere

The atmosphere is the layer of air surrounding the earth. It constitutes less than one millionth the mass of the earth, but is essential for all land-based life. It provides fresh water through the hydrological cycle, its ozone layer protects us from dangerous UV radiation, and greenhouse gases trap heat in the atmosphere resulting in a mild and temperate climate. Understanding how the atmosphere works helps us answer interesting scientific question ranging from why the dinosaur became extinct, to what the weather will be tomorrow, and how the climate will look in 100 years.

The middle atmosphere, which is the atmospheric layer between roughly 10-100 km, is interesting as it offers many unique atmospheric phenomena to study. The depletion of the ozone layer has illustrated that humans can have large scale impact on the atmosphere, understanding the dynamics of the middle atmosphere can give an indication of how accurately climate models represent small scale phenomena such as atmospheric waves, and the strong influence of solar radiation has on it can provide insights into how solar variations affect the climate. This chapter will provide a short introduction to the processes important to the middle atmosphere, and highlight some of the important scientific questions relevant to the middle atmosphere with a particular focus on the mesosphere.

### 2.1 The vertical structure of the atmosphere

The atmosphere extends from sea-level and all the way to space. It is kept in place around earth by the gravitational force. At large, the atmosphere is in the state of hydrostatic equilibrium. This means that the gravitational force is balanced by the vertical pressure gradient, or buoyancy, force. A result of this is that the pressure decreases exponentially with altitude, as does the density due to the compressibility of air.

It is customary to divide the atmosphere into layers based on the vertical temperature gradient. Figure 2.1 shows the temperature structure of the atmosphere. The

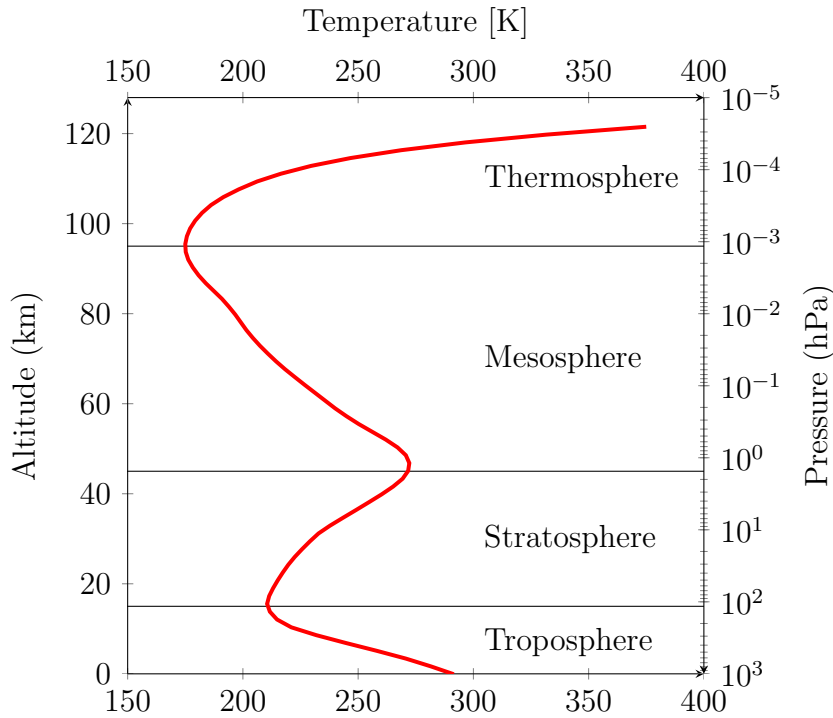


**Figure 2.1:** Temperature and layers of the atmosphere. The temperature data is taken from the COSPAR International Reference Atmosphere (CIRA-86), at 40° N, June [Rees et al., 1990].

lowermost layer is called the troposphere and is characterised by a decrease in temperature with altitude. Within this layer we find most of the common atmospheric phenomena such as clouds and precipitation. At around 10-15 km the increased photolysis of ozone causes the temperature to increase with height. The resulting layer is called the stratosphere. This part of the atmosphere is home to the ozone layer which protects the ground from DNA damaging UV radiation. Above 50 km, in the layer known as the mesosphere, the temperature is declining with altitude again. This layer is home to the coldest place on earth, the summer mesopause. The middle atmosphere is a collective term for both the stratosphere and mesosphere. Above the mesopause, in the thermosphere, the temperature increases with height.

## 2.2 General Circulation

The principal driver of air movement on the earth is the sun. Since the incoming solar energy varies with latitude an energy imbalance is created which is restored by transport of energy from the equator to the poles. Due to the rotation of the earth, topographic features, and the chemical composition of the atmosphere, the general circulation follows a set of intricate patterns rather than a direct poleward flow. Figure 2.2 shows the zonal mean temperature distribution of the atmosphere

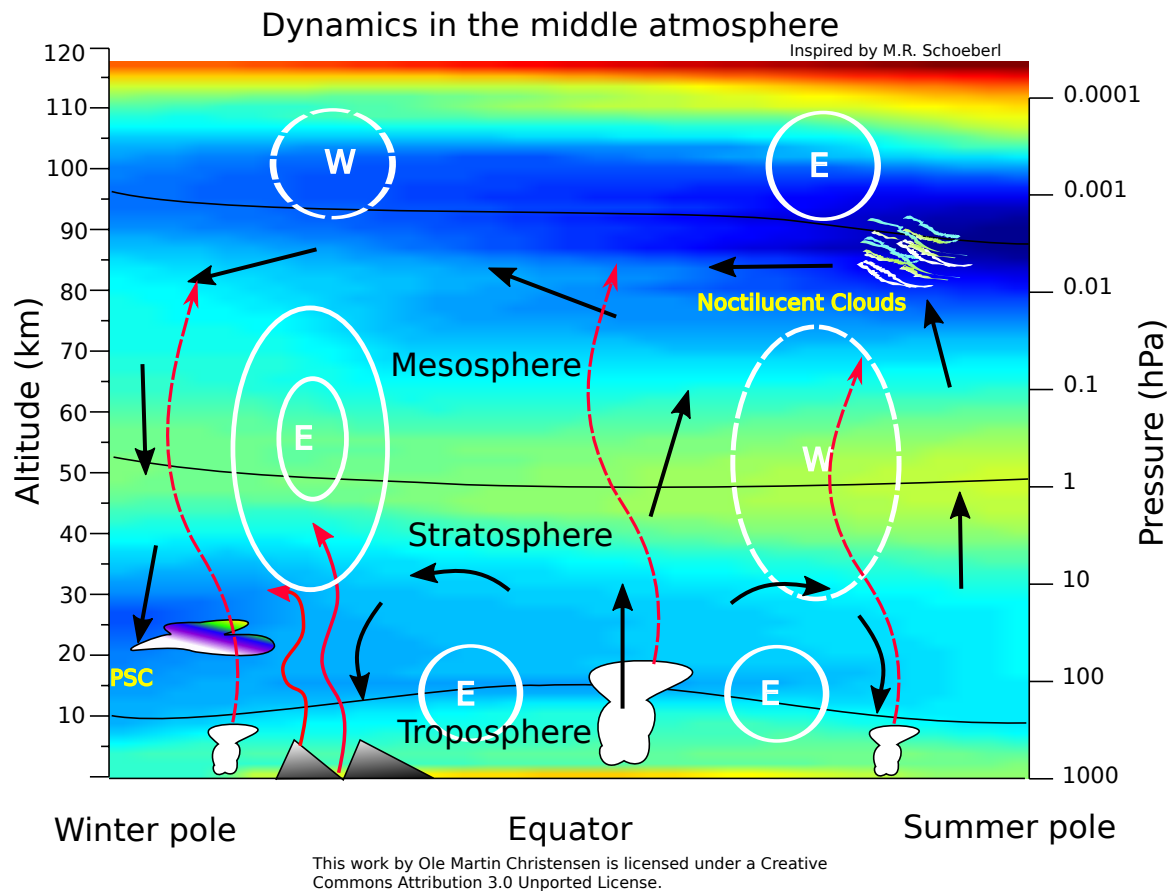


**Figure 2.2:** An illustration of the general circulation of the middle atmosphere. The background contours is the zonal mean temperature from CIRA-86 during the solstice. The white lines depicts the zonal mean wind in eastward and westward direction. The dashed and solid red lines are gravity and planetary waves respectively. The black arrows show the mean residual circulation.

together with the major middle-atmospheric general circulation patterns.

The two most important features of the general circulation are the Brewer-Dobson circulation in the stratosphere and the meridional pole to pole circulation in the mesosphere. The Brewer-Dobson circulation is driven by the deposition of momentum by planetary waves breaking in the stratosphere. Planetary waves, or Rossby waves, are large scale waves with wavelengths on the order of the planetary circumference. These planetary wave modes can be forced by for example large topographic features such as the Rocky mountains or the Himalayas. When these waves break, they deposit westward momentum in the stratosphere, which through the Coriolis force leads to a poleward transport in the upper stratosphere, creating the Brewer-Dobson circulation [Holton, 1992].

In the mesosphere the circulation is driven by the breaking of gravity waves. Gravity waves are smaller scale waves generated by topographic features or convective

activity in the troposphere. Though waves carrying both eastward and westward momentum can propagate upwards they are filtered in the stratosphere by the mean zonal winds. This filtering occurs since only gravity waves with zonal phase speeds larger than, or opposite to, the mean zonal wind can propagate upwards. From figure 2.2 we see that the prevailing stratospheric winds are eastwards in the winter and westwards in the summer. This means that gravity waves breaking in the mesosphere deposit net westwards momentum in the winter hemisphere and net eastwards in the summer hemisphere. The result of this breaking is a single cell transporting air from the summer to the winter pole. This modifies the temperature distribution, adiabatically cooling the atmosphere in areas of ascending air, and heating it in areas of descending air. This effect is seen particularly in the summer mesopause ( $\sim 90$  km) where the adiabatic cooling of ascending air makes it extremely cold despite 24 h solar heating [Brasseur and Solomon, 2005].

One particularly interesting pattern in the middle atmosphere is a persistent vortex over the winter pole. This polar vortex is characterised by the strong westerly winds seen in the winter strato-mesosphere. Within this vortex the air is isolated from the warm subtropical air. In the stratosphere the polar vortex is scientifically interesting as the cool isolated air, allows for the formation of polar stratospheric clouds, which enhances the destruction of ozone through heterogeneous chemistry [Brasseur and Solomon, 2005].

## 2.3 The changing middle atmosphere

Human influence on the atmosphere has been unequivocally established by scientists throughout the 20<sup>th</sup> century, but the full implications of these changes is far from understood. For the middle atmosphere two anthropogenically generated phenomena are particularly important. The first is the ozone loss in the middle atmosphere resulting from the release of chlorofluorocarbons (CFC). The second phenomenon is the atmospheric change occurring due to the anthropogenic release of greenhouse gases, in particular  $\text{CO}_2$  and  $\text{CH}_4$ .

Ozone is important for the middle atmosphere as it absorbs UV-radiation, heating the middle atmosphere. In the seventies it became clear that the amount of ozone in the middle atmosphere, and in particular in the upper stratosphere, was decreasing. This decrease was caused by the release of CFC-gases, which with their long photochemical lifetime can be transported out of the troposphere and into the stratosphere. In the stratosphere they undergo photolysis, and release reactants that result in the destruction of ozone through catalytic reactions. As a response to the realisation that this depletion was taking place and was a global problem, the Montréal protocol was established in 1987 to limit the release of CFC-gases.

Greenhouse gases<sup>1</sup> have their name from the fact that they heat the troposphere

---

<sup>1</sup>The name greenhouse gas is actually a misnomer as the major warming effect in a greenhouse is not the trapping of radiation, but rather by preventing the heated air from escaping.

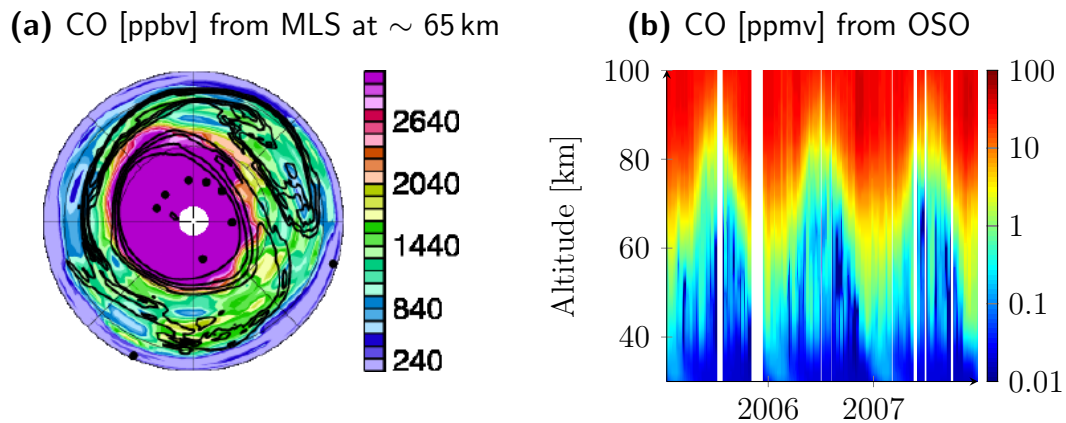


**Figure 2.3:** Volume mixing ratio of CO in the middle atmosphere. Panel a: The horizontal distribution the 20. January from 0-90 °N at roughly 65 km (3200 K) measured by the microwave limb sounder on board Aura [Manney et al., 2009]. Panel b: The seasonal variation of CO above OSO measured with the 115 GHz radiometer.

since they allow shortwave radiation in the form of UV- or visible light to reach the ground, but trap the re-emitted long wave radiation. The warming effect of greenhouse gases is well known, but they have the opposite, cooling, effect in the middle atmosphere. The cooling of the middle atmosphere is important as it helps us differentiate between natural and anthropogenic forces on the climate system [Thompson et al., 2012]. Cooling of the middle atmosphere has been determined to be  $\sim 0.5$  K/decade in the stratosphere [Thompson et al., 2012] and 1-3 K/decade in the mesosphere [Beig, 2011]. However, there is much uncertainty related to how these temperature changes might affect the dynamics in the middle atmosphere, and if any changes in the dynamics will feed back into tropospheric weather patterns.

Other unresolved questions include how the increased amount of methane in the atmosphere will affect water vapour concentrations in the mesosphere, which is important for the formation of noctilucent clouds, and why the temperature at the mesopause appears to remain constant even though the rest of the middle and upper atmosphere is cooling [Beig et al., 2003]. To answer these questions it is important to monitor the middle atmosphere and be observant of any changes detected.

## 2.4 The chemistry of mesospheric CO

One way to investigate the dynamics of the middle atmosphere is to trace the concentration of gases with long photochemical lifetimes. If a particular gas is created locally in one place, and is not removed photochemically, the distribution of this gas will be determined by the transport in the atmosphere. One such tracer gas is carbon monoxide. In the stratosphere it is produced by oxidation of methane and in thermosphere and mesopause region it is produced through the photolysis of carbon

dioxide [Brasseur and Solomon, 2005]



The only important destruction mechanism in the mesosphere is the reaction with OH



Figure 2.3a shows the concentration of CO at around 65 km during the arctic winter measured by AURA-MLS. The aforementioned polar vortex is seen clearly through the large concentration of CO. Since CO is mainly produced through photolysis in the thermosphere, this high concentration must come from large scale descent in the winter mesosphere, which is consistent with the general circulation in figure 2.2. Figure 2.3b shows the distribution of CO measured from the OSO radiometer. The same large scale descent is clearly seen during the winter months. Measuring this descent is interesting, as it can be used to test the gravity wave parametrisation of climate models (e.g. Forkman et al. [2003b]).

# Measurement Principles

To perform remote sensing measurements we need to understand how electromagnetic radiation arises and propagates through the atmosphere. Furthermore, we need analysis techniques that can extract the wanted information from the received EM-radiation and understand the errors associated with such techniques. This chapter will provide a short introduction to the measurement principles of atmospheric remote sensing, and the basic theory needed to understand the errors and uncertainties in such a measurement.

### 3.1 Blackbody radiation

Electromagnetic (EM) radiation is emitted from charged particles. It is classified based on its wavelength, and figure 3.1 shows an overview of the EM spectrum. Different categories include the UV- (100 nm to 400 nm), the visible- (400 nm to 700 nm) and the microwave region (mm-cm). The amount of radiation travelling through an area from within a certain solid angle is called radiance and is a useful quantity when discussing the strength of EM-radiation.

A blackbody is an object that absorbs all incident radiation. For such objects the emitted radiance per frequency, also called the spectral radiance, is given by Planck's law of radiation

$$L_\nu = \frac{2h\nu^3}{c^2(e^{h\nu/k_bT} - 1)} \left[ \frac{\text{W}}{\text{m}^2 \text{ Hz sr}} \right]. \quad (3.1)$$

Here  $h$  is Planck's constant,  $\nu$  the frequency of the radiation,  $c$  the speed of light,  $k_b$  Boltzmann constant and  $T$  the temperature of the object.

Not all objects are perfect blackbodies, and to take this into account, thermal radiation from such non-blackbody objects is described by the emissivity. The emissivity relates the blackbody spectral radiance to the true spectral radiance by

$$L_\nu = \epsilon(\nu)B_\nu, \quad (3.2)$$

where  $B_\nu$  is the radiance from a blackbody at the same temperature.

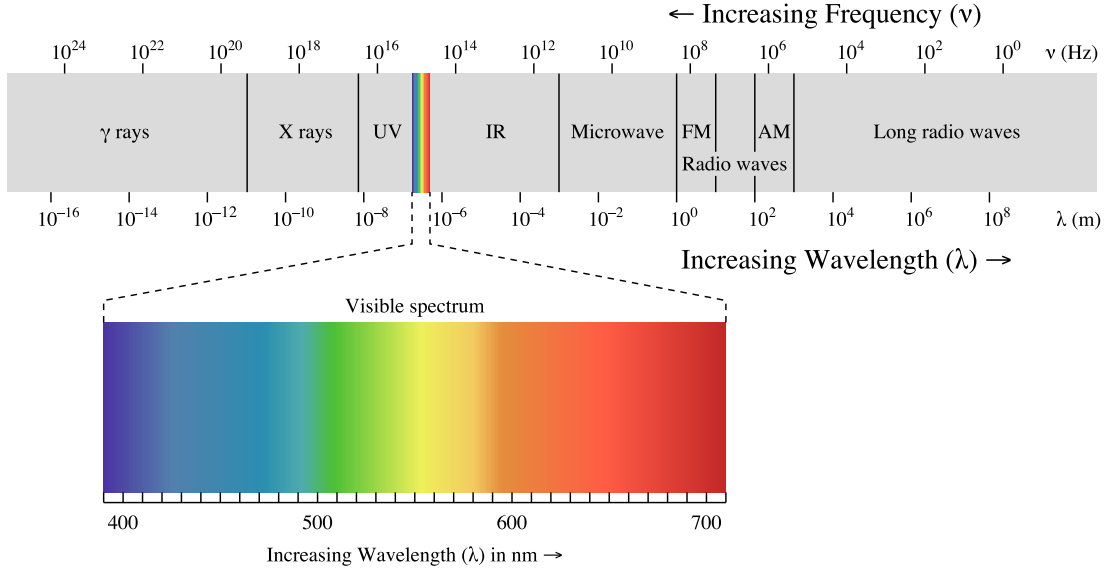


**Figure 3.1:** The electromagnetic spectrum

The absorptivity,  $\alpha$ , describes how well an object absorbs EM radiation. In local thermodynamic equilibrium (LTE) Kirchoff's law applies. This states that the absorptivity is equal to the emissivity

$$\alpha = \epsilon. \quad (3.3)$$

Local thermodynamic equilibrium is reached when the rate of collisions between molecules is much higher than the rate of which molecules absorb and emit photons, and for most rotational transitions, LTE is valid for the entire middle atmosphere [Lopez-Puertas and Taylor, 2001].

In remote sensing, spectral radiance is usually given in terms of brightness temperature, which is the temperature a blackbody object would need to have in order to radiate with measured spectral radiance. Thus from equation 3.1 and 3.2 the brightness temperature,  $T_b$  can be written as

$$T_b = \frac{h\nu}{k_b} \frac{1}{\ln\left(1 + \frac{1}{\epsilon} (e^{h\nu/k_b T} - 1)\right)}. \quad (3.4)$$

This nomenclature is particularly useful in the long wavelength-, or Rayleigh-Jeans, approximation ( $h\nu \ll k_b T$ ) where the relationship between the physical temperature and the brightness temperature reduces to

$$T_b = \epsilon(\nu)T. \quad (3.5)$$

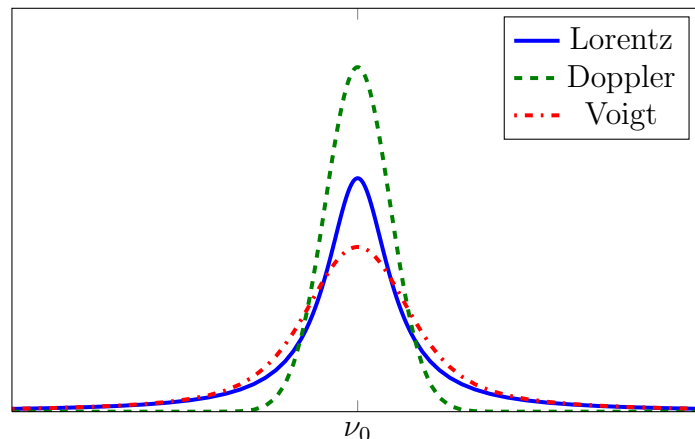


**Figure 3.2:** Three different line functions describing molecular absorption and emission. The functions are normalised to have an area of unity.

## 3.2 Absorption and emission from gases

Electromagnetic waves travelling through a medium will interact with it. This interaction includes scattering by particles and molecules, where new waves are generated, as well as absorption, where the energy is converted into internal energy of the molecule. For bounded changes in internal energy, e.g. electronic, vibrational or rotational transitions, the internal energy change,  $\Delta E$ , will be related to the absorbed or emitted frequency by

$$\Delta E = h\nu. \quad (3.6)$$

For gases in the atmosphere these energy transitions are affected by line-broadening processes. To describe these processes we introduce the *shape function*,  $\Phi$ , and the line-strength,  $S$ , such that the absorption coefficient for a given molecular transition,  $i$ , in a medium is given by

$$\gamma_{abs}^i = n^i S^i \Phi^i(\nu) \left[ \frac{1}{\text{m}} \right], \quad (3.7)$$

where  $n^i$  is the number density of the corresponding molecule in the medium. The absorption coefficient gives the amount of absorption per unit distance.

Molecules in a gas have a certain velocity relative to the incoming or outgoing EM-wave. This motion leads to a Doppler shift in the absorption/emission frequency. For a given temperature the random velocities of molecules are given by the Maxwell-Boltzmann distribution, and the resulting shape function is a Gaussian (green-dashed line in figure 3.2). The Lorentz line function (blue line in figure 3.2) describes the pressure broadening, which arises due to collisions between molecules. Quantum mechanical states also have an intrinsic lifetime due to the natural decay process. This leads to broadening of the line called natural line broadening. This broadening is also described by the Lorentz function, but for transitions in LTE the collisional lifetime is much shorter than the natural lifetime, and natural linebroadening is negligible.

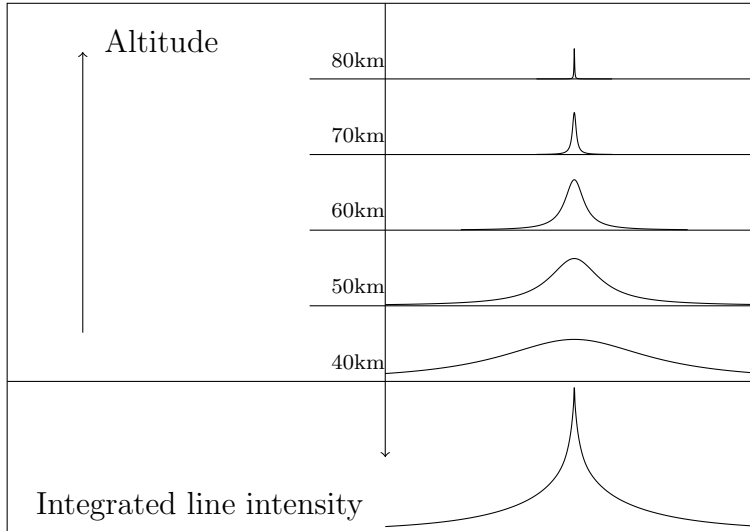


**Figure 3.3:** An illustration of the radiative transfer equation for an optically thin line. The emission at each altitude is given by Lorentzian and the total radiation reaching the ground is the sum of the emission at all altitudes.

In the lower atmosphere, the line-width of a transition will be totally dominated by pressure-broadening as the high density leads to frequent collisions between molecules. As the pressure decreases with altitude, the collisional frequency declines and the line becomes narrower. At some point the pressure broadened linewidth will become smaller than that of the Doppler broadening, and the spectrum will start to look more Gaussian in shape. At this altitude the clear relationship between lineshape and altitude vanishes since the Doppler width is only dependent on the square root of the temperature, and not the pressure. At altitudes where both pressure and Doppler broadening is important the shape function will take on the Voigt lineshape (red-dot-dashed line). This is a Lorentzian shape convolved with a Gaussian. The Voigt lineshape gives a more realistic description a line transition in the true atmosphere than using the Lorentzian or Gaussian alone. Other lineshapes also (e.g Vleck-weisskopf) exists that take into account the more subtle effects of interaction in collisions.

### 3.3 The radiative transfer equation

The radiative transfer equation describes how EM-energy is transferred along a path  $s$  in the atmosphere

$$\frac{dL_\nu}{ds} = -L_\nu\gamma + S. \quad (3.8)$$

The first term on the right hand side describes extinction, where  $\gamma$  is the extinction coefficient. The second term describes additional sources of radiation through the source term  $S$ . The most common reasons for extinction in the atmosphere are

scattering, and absorption along the path of the radiation. Common sources include scattering into the path, and thermal radiation emitted from the atmosphere along the path.

For instruments on the ground the spectral radiance coming from the atmosphere can be found by integrating equation 3.8 from the top of the atmosphere down to the detector. At microwave frequencies scattering can often be neglected [Clancy and Muhleman, 1993], and assuming LTE, the radiative transfer is given by

$$L_\nu(0) = L_\nu(s_0)e^{-\tau(s_0,\nu)} + \int_{s_0}^0 \epsilon(\nu)B_\nu(T(s))e^{-\tau(s,\nu)} ds, \quad (3.9)$$

where  $B_\nu$  is the blackbody spectral radiance,  $s_0$  the top of the atmosphere, and  $\tau$  is the optical thickness along the path. Neglecting scattering,  $\tau$  is given by

$$\tau(s) = \int_s^0 \gamma_{abs}(s',\nu)ds', \quad (3.10)$$

where  $s'$  indicates integration along the propagation path and  $\gamma_{abs}$  the total absorption coefficient from all molecules and particles along the path. Figure 3.3 illustrates the concept of integrating the radiative transfer equation from the top of the atmosphere for a single, optically thin (i.e. absorption negligible), transition line. Each altitude contributes with some radiation, and the total measured radiation at ground level is given by the sum of the emitted radiation from each altitude.

A radiative transfer simulator is a computer program that calculates the radiative transfer by solving the radiative transfer equation numerically. The radiative transfer, or forward, model used in this thesis is ARTS v.2.0. [Eriksson et al., 2011]. This is a radiative transfer model developed for the microwave region, and can simulate many different viewing geometries and instruments.

## 3.4 Retrieval

The fact that the lineshape changes with altitude (see figure 3.3) means that a measured spectrum at ground level will not only contain information about the total integrated column of a molecule, but also its altitude distribution. The green and blue lines in figure 3.4a are two altitudes profiles of water vapour differing in the mesosphere. The corresponding lines in figure 3.4b show the spectral intensity around the 22 GHz water vapour transition measured at ground level (ignoring the troposphere and cosmic background radiation) resulting from these two profiles. In the wings the two spectra have the same value, but at the line centre the green spectrum shows a clear increase in brightness temperature. This increase comes from the increased H<sub>2</sub>O concentration around 60 km. The increase is only seen at the line centre as the

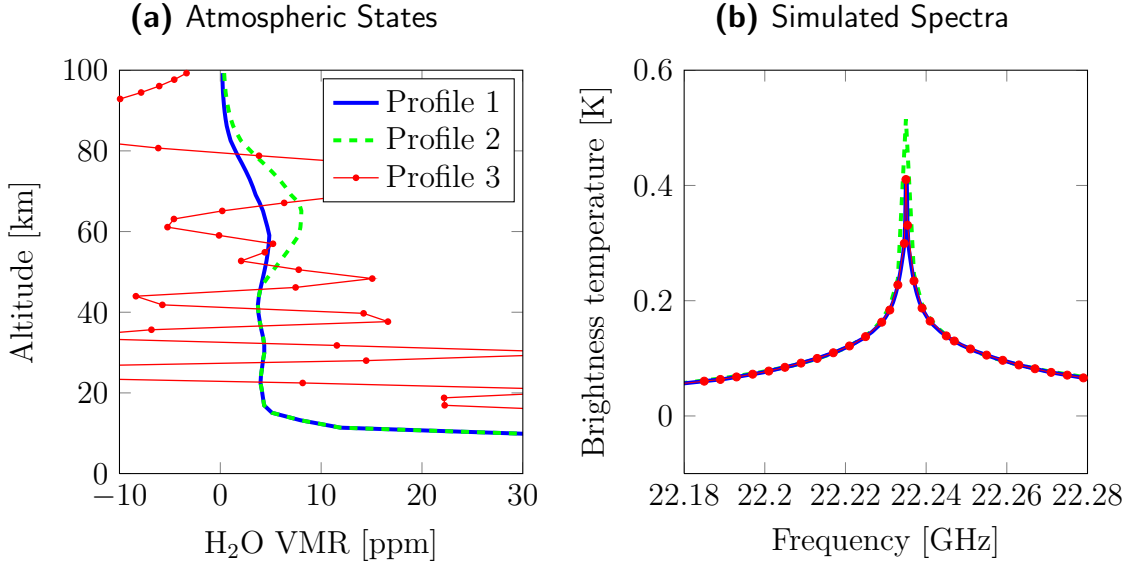


**Figure 3.4:** Left panel: Some atmospheric water vapour profiles. Profile 1 and 2 represent realistic profiles, while Profile 3 is an example of an unrealistic profile. Right panel: Spectra measured from ground level (ignoring the troposphere and cosmic background radiation) resulting from the different profiles. Note how the unrealistic profile still produces a realistic spectrum similar to the blue profile.

emitted radiation at high altitudes is less affected by pressure broadening than radiation emitted at lower altitudes. This example indicates how we can use the shape and intensity of a line to determine the altitude profile.

The process of determining the true atmospheric profile from a measured spectrum is known as an inversion, or retrieval. To solve this problem numerically on a computer, the radiative transfer equation is linearised around some atmospheric state and expressed in linear algebra as

$$\mathbf{y} = \mathbf{K}\mathbf{x} + \epsilon, \quad (3.11)$$

where  $\mathbf{y}$  is the measured spectrum arising from from atmospheric state,  $\mathbf{x}$ , and with errors,  $\epsilon$ .  $\mathbf{K} \equiv \partial\mathbf{y}/\partial\mathbf{x}$  is the linearised forward model known as the Weighting function- or Jacobian matrix. The vector spaces spanned by  $\mathbf{x}$  and  $\mathbf{y}$  are called the measurement and state space respectively, and  $\mathbf{K}$  can be seen as a mapping from one space to the other.

Naively one might think that finding  $\mathbf{x}$  for a given  $\mathbf{y}$  could be solved by inverting  $\mathbf{K}$ , or using a least squares method to estimate  $\mathbf{x}$ . However, the problem of retrieving  $\mathbf{x}$  is usually ill-posed. Formally this is due to  $\mathbf{K}$  being rank-deficient. Physically this means that there is not a unique profile that reproduces the measured spectrum. This is illustrated by the red dotted lines in figure 3.4a and 3.4b. The red profile of water vapour looks very different from the blue profile. However, when the spectrum resulting from this profile is calculated, it will be exactly equal to that resulting from

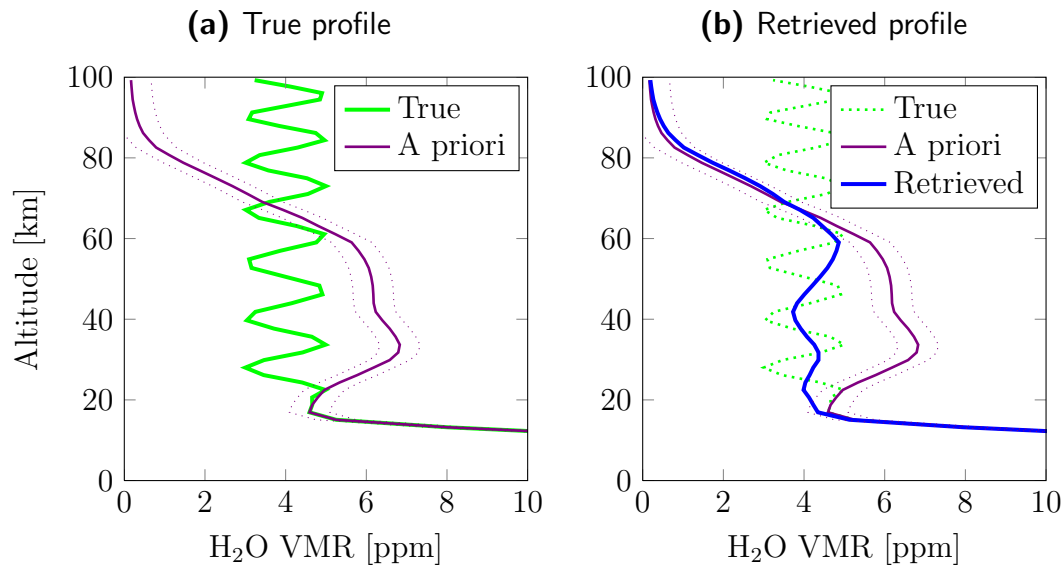


**Figure 3.5:** A simulated retrieval of water vapour. The true profile (green-solid and green-dotted lines), the a priori profile (violet lines) and the a priori standard deviation (dotted-violet lines). In absence of noise, the retrieved state (blue line) ends up as a smoothed version of the true profile.

the blue profile. This means that if an instrument measures a radiance corresponding to the blue spectrum in figure 3.4b, it is formally impossible to determine whether the true atmosphere looks like the red or the blue profile in figure 3.4a.

It is possible to mitigate this problem of non-uniqueness. By inspection we can actually see that the red profile is unphysical as it contains negative concentrations of  $\text{H}_2\text{O}$ . Furthermore, based on the current knowledge of atmospheric chemistry and dynamics, we know that the large fluctuations seen in  $\text{H}_2\text{O}$ , would not exist in the atmosphere. Thus, by inspection it is possible to determine that the blue profile in figure 3.4a is the more probable solution to the inverse problem. Such a restriction of possible solutions is called a regularisation method.

A common regularisation method used for microwave spectrometers is the maximum a posteriori (MAP) method, also called the optimal estimation method [Rodgers, 2000]. This method uses a statistical description of the expected profile to constrain the retrieved values. An a priori (expected) profile is described by an expectation value  $\mathbf{x}_a$  and a covariance matrix  $\mathbf{S}_a$ . A covariance matrix is a matrix which for a set of stochastic variables has elements  $\mathbf{S}_{ij} = \sigma_i \sigma_j \rho_{ij}$ , where  $\rho_{ij}$  is the correlation between variable  $i$  and  $j$ , and  $\sigma_i$  and  $\sigma_j$  are their respective standard deviations. Thus,  $\mathbf{S}_a$  describes the uncertainty in the a priori profile. The larger the uncertainty in the a priori profile, the less constraint is placed on the retrievals. Figure 3.5 shows a simulated retrieval of water vapour in the middle atmosphere. The green line shows the true profile. The blue line in 3.5b is the profile retrieved using the violet line as the a priori constraint. The standard deviation of the a priori profile is shown as the

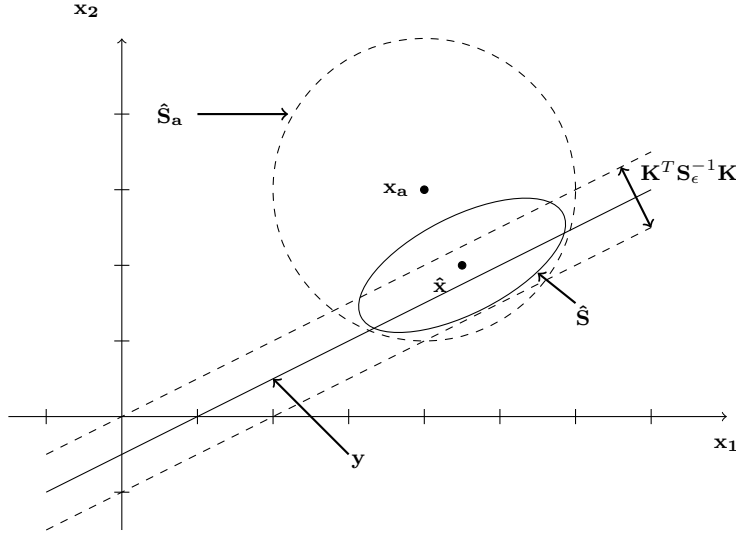


**Figure 3.6:** A schematic representation of the maximum a posteriori retrieval method. The states corresponding to the measurement,  $y$ , gives an ambiguous relationship between the two atmospheric variables  $x_1$  and  $x_2$ . The retrieved value using the MAP method is  $\hat{x}$ . The a priori state is given by  $x_a$ . The a priori covariance matrix is given by  $S_a$ , the measurement uncertainty mapped to the state space is given by  $K^T S_\epsilon K$ , and the a posteriori error by  $\hat{S}$ .

dotted-violet line.

To use the a priori profile as a constraint, a cost function,  $\chi^2$ , is defined. This function describes how well the retrieved state,  $\hat{x}$ , fits the measured spectrum ( $y - K\hat{x}$ ), and how well it fits the a priori profile ( $\hat{x} - x_a$ ). Scaling the two fitting parameters with their uncertainty gives

$$\chi^2 = (\hat{x} - x_a)^T S_a^{-1} (\hat{x} - x_a) + (y - K\hat{x})^T S_\epsilon^{-1} (y - K\hat{x}), \quad (3.12)$$

where  $S_a$  and  $S_\epsilon$  are the covariance matrices describing the uncertainty in the a priori profile and the measurement vector, respectively.

To find the minimum of the cost function  $\chi^2$ , it is helpful to first consider an analogous 1-dimensional case. Two measurements,  $x_\epsilon$  and  $x_a$ , with uncertainties  $\sigma_\epsilon$  and  $\sigma_a$ , are performed of the same scalar variable  $x$ . The optimal way of combining these two measurements in order to estimate  $x$  is to scale each of the measurements with their uncertainties

$$\hat{x} = \left( \frac{1}{\sigma_\epsilon^2} + \frac{1}{\sigma_a^2} \right)^{-1} \left( \frac{x_\epsilon}{\sigma_\epsilon^2} + \frac{x_a}{\sigma_a^2} \right), \quad (3.13)$$

where  $\hat{x}$  is the “optimal” estimate of  $x$  based on the two measurements.

Using the matrix formalism introduced earlier, the state minimising  $\chi^2$  is given by

$$\hat{x} = (K^T S_\epsilon^{-1} K + S_a^{-1})^{-1} (K^T S_\epsilon^{-1} K x + S_a^{-1} x_a) \quad (3.14)$$

The similarities between equation 3.14 and equation 3.13 can be seen. The difference is that in the matrix formulation the scalars in equation 3.13 describing the uncertainties are replaced by covariance matrices. For the a priori profile this is  $\mathbf{S}_a$ . For the measurement it is the covariance describing errors in the measurement mapped to the state space,  $\mathbf{K}^T \mathbf{S}_\epsilon^{-1} \mathbf{K}$ .

Figure 3.6 illustrates the concept of MAP geometrically. The inverse problem posed is to find a position in the state space spanned by  $\mathbf{x}_1$  and  $\mathbf{x}_2$ . A measurement provides some information on the relationship between  $\mathbf{x}_1$  and  $\mathbf{x}_2$ , but all states along the line given by the measurement  $\mathbf{y}$  is a possible solution. The retrieved state,  $\hat{\mathbf{x}}$ , is the point which minimises  $\chi^2$  so it is right between  $\mathbf{x}_a$  and  $\mathbf{y}$ , where the exact distance from  $\mathbf{x}_a$  and  $\mathbf{y}$  is determined by the constraint posed by  $\mathbf{S}_a$  and  $\mathbf{S}_\epsilon$ .

### 3.5 Limitations of an retrieval

The MAP method does not only provide a retrieved profile, but can also be used to estimate the error in the retrieved profile. Equation 3.14 can be written as

$$\hat{\mathbf{x}} = \mathbf{x}_a + \mathbf{G}(\mathbf{y} - \mathbf{K}\mathbf{x}_a), \quad (3.15)$$

where  $\mathbf{G}$  is the gain-matrix

$$\mathbf{G} \equiv \partial \hat{\mathbf{y}} / \partial \mathbf{y} = (\mathbf{K}^T \mathbf{S}_\epsilon^{-1} \mathbf{K} + \mathbf{S}_a^{-1})^{-1} \mathbf{K}^T \mathbf{S}_\epsilon^{-1}. \quad (3.16)$$

Using equation 3.11 and 3.15, the error in the retrieval,  $\hat{\mathbf{x}} - \mathbf{x}$ , can now be calculated through

$$\begin{aligned} \hat{\mathbf{x}} - \mathbf{x} &= \mathbf{x}_a + \mathbf{G}(\mathbf{y} - \mathbf{K}\mathbf{x}_a) - \mathbf{x} \\ &= \mathbf{x}_a + \mathbf{G}(\mathbf{K}\mathbf{x} + \epsilon - \mathbf{K}\mathbf{x}_a) - \mathbf{x} \\ &= (\mathbf{G}\mathbf{K} - \mathbf{I})(\mathbf{x} - \mathbf{x}_a) + \mathbf{G}\epsilon. \end{aligned} \quad (3.17)$$

The first term in last line of equation 3.17 is known as the smoothing error, and represents the error in the retrieved state as a result of the limited resolution of the retrieval. The effect of the limited resolution can be seen in figure 3.5b as the retrieved state (blue line) does not follow the variation of the true state (green dotted line), but rather a smoothed version of these variations. This limited vertical resolution is usually described by the averaging kernel matrix

$$\mathbf{A} \equiv \frac{\partial \hat{\mathbf{x}}}{\partial \mathbf{x}} = \mathbf{G}\mathbf{K}. \quad (3.18)$$

Each element,  $\mathbf{A}_{ij}$ , in this matrix describes the change in the retrieved variable  $\hat{\mathbf{x}}_i$  from a change in the real atmospheric variable  $\mathbf{x}_j$ . Figure 3.7a shows the rows of the averaging kernel matrix from the retrievals depicted in figure 3.5. These rows are called the averaging kernels (AVKs). They indicate which altitudes the retrieved

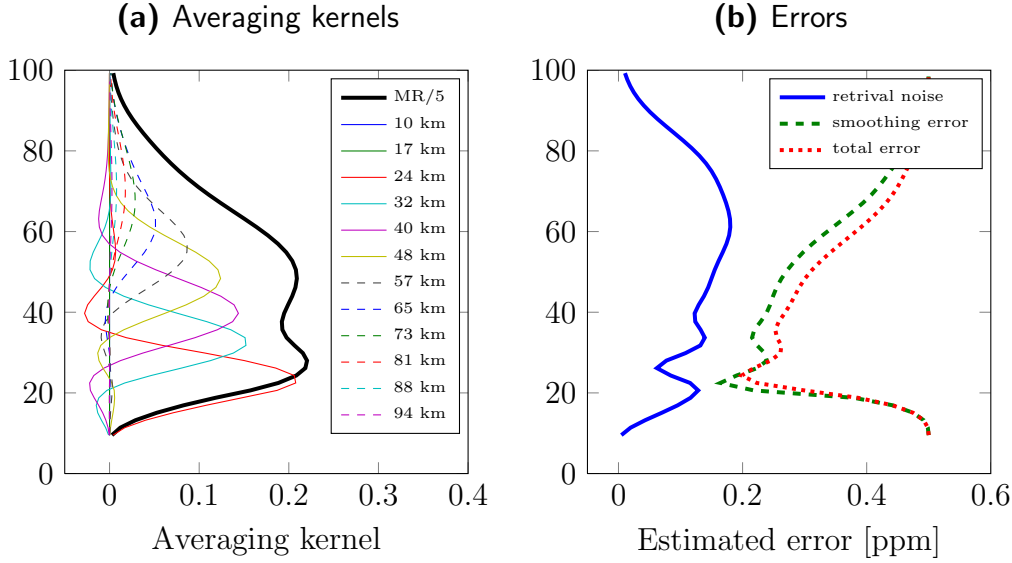


**Figure 3.7:** Panel a: Averaging kernels for different altitudes for the retrieval in figure 3.5. The thick black line is the measurement response divided by 5. Panel b: The square root of the diagonal elements of  $\mathbf{S}_m$  (blue solid),  $\mathbf{S}_s$  (green dashed) and  $\hat{\mathbf{S}}$  (red dotted).

water vapour concentration at each altitude takes information from. The full width at half maximum of these kernels can be considered as a measure of the vertical resolution of the retrievals. Assuming that the covariance of the true atmosphere is correctly described by  $\mathbf{S}_a$  the covariance of the smoothing error is

$$\mathbf{S}_s = (\mathbf{A} - \mathbf{I})\mathbf{S}_a(\mathbf{A} - \mathbf{I})^T. \quad (3.19)$$

The area of an averaging kernel gives an indication to what degree the retrieved value at that altitude uses information from the measurement. This value, called the measurement response, is plotted as the solid black line in figure 3.7a. A rule of thumb is that measurement response should be larger than 0.8 for a retrieved value to be considered valid.

The second term in equation 3.17 is the error in the retrievals resulting from errors in the measured spectrum. If the errors in the measured spectrum solely come from thermal noise in the measurement, this second term is called the retrieval noise, and its covariance is given by

$$\mathbf{S}_m = \mathbf{G}\mathbf{S}_\epsilon\mathbf{G}^T. \quad (3.20)$$

Figure 3.7b depicts the square root of the diagonal elements for the different error terms for the retrievals in figure 3.5, including the total estimated retrieval error

$$\hat{\mathbf{S}} = (\mathbf{K}^T\mathbf{S}_\epsilon^{-1}\mathbf{K} + \mathbf{S}_a^{-1})^{-1}. \quad (3.21)$$

To calculate these error the covariance matrices  $\mathbf{S}_a$  and  $\mathbf{S}_\epsilon$  need to be specified. In the example presented here they are diagonal matrices with diagonal elements of  $0.5^2$  (relative units) and  $0.05^2$  K respectively.

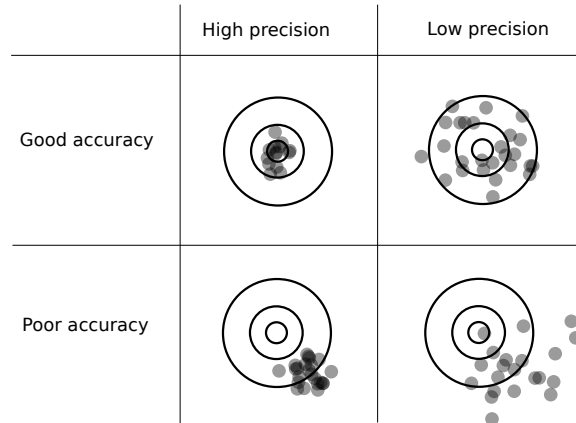


**Figure 3.8:** The effect of accuracy and precision on a set of measurements (dots). The true value is the bullseye.

### 3.6 Instrumental error sources

Estimating errors is an important part of making a measurement, and accurate error estimations are needed to ensure that measurements can be properly compared to each other, and to models. When doing an error analysis it is common to separate errors into random errors and systematic errors. A basic assumption of random errors is that it is possible to decrease them by repeating the same measurement several times, and taking the average. Systematic errors on the other hand, will not go away upon averaging. Figure 3.8 shows the difference between these error types. The magnitude of the errors are known as precision (random errors) and accuracy (systematic errors).

Random errors are often possible to estimate based on knowledge of the instrument, or by looking at the variability in the measured quantity and compare it to the expected variability. As discussed in the last section, the MAP method can provide an estimate of the expected random errors through the the a posteriori covariance matrix,  $\hat{\mathbf{S}}$ . The MAP method can also estimate a number of errors. However, some errors might come from unknown defects in the instrument, and can only be discovered through cross-comparing the results with other instruments. For further information on cross-comparing instruments and error estimation, see the appended Paper A where such a cross-comparison is done between the 115 GHz radiometer at OSO and four different satellite instruments.

---

# CHAPTER 4

---

## Instruments

To interpret an atmospheric measurement, it is important to understand the instrument performing the measurement. This chapter will introduce the instruments used in the two appended papers with particular focus on the microwave spectrometer.

### 4.1 The microwave spectrometer

Radiometers are instruments that measure the radiance of EM-radiation. Different radiometers exist for the different regions of the EM-spectrum. A particular type of radiometer is the spectrometer which measures the radiance of radiation as a function of frequency. Figure 4.1 shows an overview of a heterodyne microwave spectrometer. The radiation from the atmosphere is captured by an antenna. The frequency of the measured atmospheric signal at the antenna is called the radio frequency (RF). After being captured, this signal might be amplified and/or filtered depending the receiver design. The signal is then mixed non-linearly with a signal of known frequency from a local oscillator (LO). By mixing these two signals, the frequency of the measured signal can be reduced to a lower intermediate frequency (IF) and amplified, before it is recorded by a spectrometer. This downconversion is necessary since high frequency signals are hard to amplify and record without adding too much noise to the measurements.

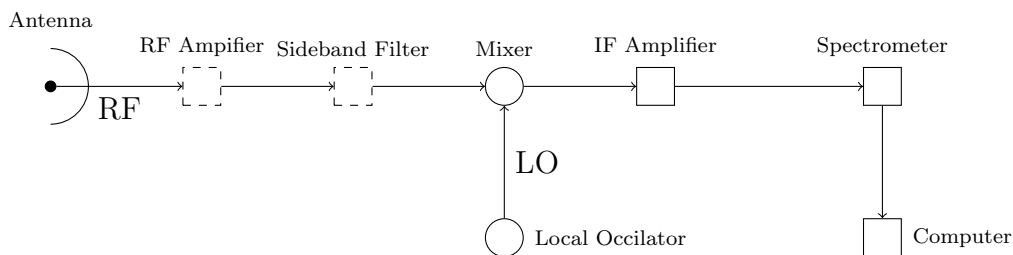


**Figure 4.1:** A schematic view of a microwave spectrometer.

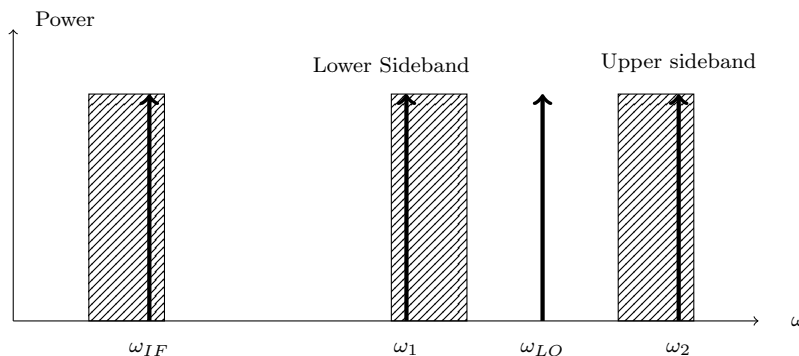


**Figure 4.2:** The heterodyne principle. When the RF signal is mixed with the LO signal ( $\omega_{LO}$ ), both frequency  $\omega_1$  and  $\omega_2$  will be mixed to the same intermediate frequency,  $\omega_{IF}$ .

The mixing technique is called heterodyne mixing. It is performed by a non-linear component called a mixer. In its simplest form a mixer can be described as a device with a purely quadratic response [Rohlfis and Wilson, 2008]. If the incoming signal is the sum of the LO and RF signal the quadratic signal leaving the mixer is

$$(A \sin(\omega_{RF}t) + B \sin(\omega_{LO}t))^2 = \frac{1}{2}(A^2 + B^2) - \frac{1}{2}A^2 \cos(2\omega_{RF}t) - \frac{1}{2}B^2 \cos(2\omega_{LO}t) + AB \cos(\underbrace{(\omega_{RF} - \omega_{LO})t}_{\omega_{IF}}) - AB \cos((\omega_{RF} + \omega_{LO})t).$$

The intermediate frequency,  $\omega_{IF}$ , is thus given by the difference between the LO frequency,  $\omega_{LO}$ , and radio frequency,  $\omega_{RF}$ . Due to the symmetry of the intermediate frequency term, signals from both  $\omega_{LO} + \omega_{IF}$  and  $\omega_{LO} - \omega_{IF}$  will be included in the IF signal. Thus, two RF bands are included in the IF signal, one on each side of the LO frequency. Figure 4.2 illustrates the principle of heterodyne detection, and shows the two RF bands. If the frequencies of interest are located in only one of the bands, a sideband filter is usually applied before the mixer to filter out the unwanted-, or image-band. Such a receiver is called a single sideband receiver. Another option is using both bands, creating a double sideband receiver.

## 4.2 Calibration

A calibration is needed to lend physical meaning to the electrical signal from the detector. Assuming a linear system, this is done by performing a measurement of thermal radiation from two known sources, or loads, one hot and one cold. This measurement can then be used to determine the relationship between the measured signal,  $S$ , and the brightness temperature  $T_b$ . These loads can in principle be anything radiating with a known brightness temperature, but for microwave radiometers the hot load is often an absorber at ambient temperature. Similarly, the cold load can for example be an absorber cooled by liquid nitrogen or helium. Figure 4.3 shows

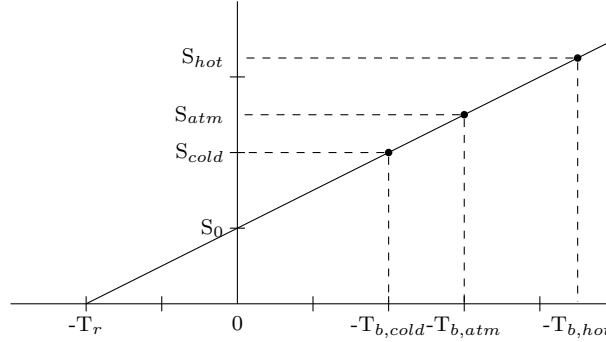


**Figure 4.3:** Calibration procedure in microwave radiometers.  $S_{hot}$ ,  $S_{cold}$  and  $S_{atm}$  are the signals from the hot load, cold load and the atmosphere respectively.  $T_{b,hot}$ ,  $T_{b,cold}$  and  $T_{b,atm}$  are the brightness temperature from in each measurement.  $S_0$  and  $T_r$  is the receiver signal and temperature.

the calibration procedure. The resulting equation for determining the atmospheric brightness temperature,  $T_{b,atm}$ , from the signal,  $S_{atm}$ , becomes

$$T_{b,atm} = \frac{T_{b,hot} - T_{b,cold}}{S_{hot} - S_{cold}} S_{atm}, \quad (4.1)$$

where subscripts *hot* and *cold* represent the signal and temperature of the hot and cold load, respectively. This calibration procedure is sufficient if the gain of the instrument is constant in time. However, most receiver systems will have time dependent variations in gain. In order to minimise the effect of these variations, a technique called Dicke-switching is used. Dicke-switching involves doing a differential measurement between a reference spectrum,  $T_{b,ref}$ , and the atmospheric spectrum, rather than measure the radiation from the atmosphere directly [Rohlfs and Wilson, 2008]. The spectrum,  $\Delta T_b$ , is then given by

$$\Delta T_b = T_{b,atm} - T_{b,ref} = \frac{T_{b,hot} - T_{b,cold}}{S_{hot} - S_{cold}} (S_{atm} - S_{ref}). \quad (4.2)$$

Since the errors from gain fluctuations are proportional to the total power measured, the receiver should be balanced. This means that the reference signal,  $S_{ref}$ , has the same power as the atmospheric signal  $S_{atm}$  without the measured line. One common way of achieving a balanced measurement is using a technique called sky-switching. Here the reference measurement is actually a measurement of the atmosphere itself, though measured at a different elevation angle than  $T_{b,atm}$ . This implies that the two measurements have different pathlength through the atmosphere, which prevents the middle atmospheric signal from being completely removed from the differential measurement. Furthermore, the different tropospheric pathlengths of the two beams are compensated for by inserting an absorber into the field of view of the reference measurement.

If the observed middle atmospheric line is narrow (i.e. smaller than the possible shift in LO frequency), sky switching can be replaced with frequency switching. In this

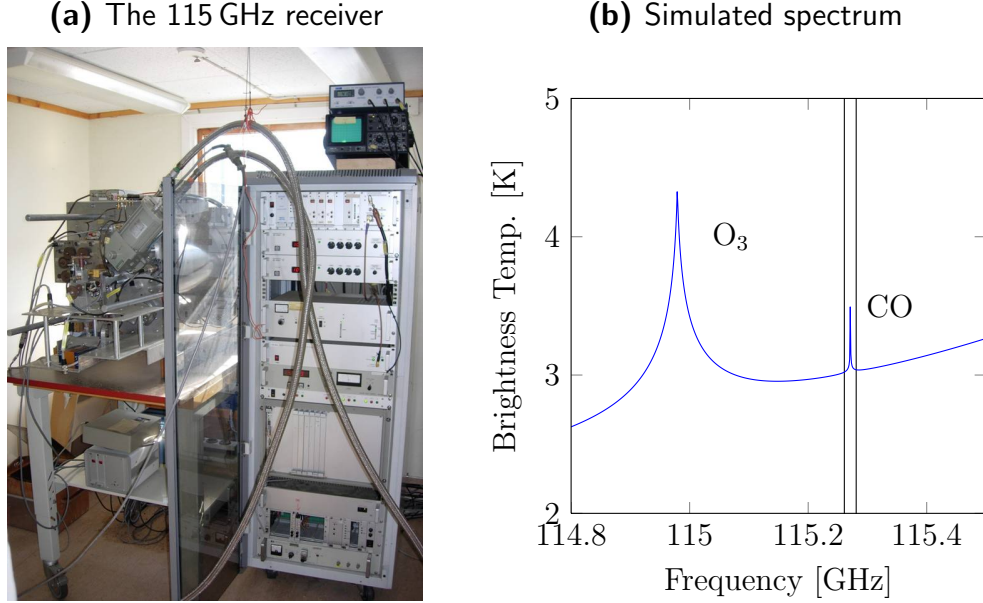


**Figure 4.4:** Panel a: A picture of the 115 GHz radiometer at OSO. Panel b: A simulated atmospheric spectrum of the frequencies around the 115 GHz CO line.

technique the local oscillator frequency is shifted a few MHz between the atmospheric and reference measurement. If this shift is smaller than the total bandwidth of the instrument, the middle atmospheric emission is included in both the reference and the target spectrum. The advantage of this is that as the measured line is seen in both the signal and reference spectrum, the effective observation time is doubled compared to sky-switching.

Though the aforementioned switching methods remove most of the tropospheric signal from the measured spectra, it does not take into account the damping of the observed line due to tropospheric absorption. One way to account for this, is to solve the radiative transfer equation (equation 3.8) for a single layer troposphere with an effective temperature  $T_{eff}$ , and a tropopause at  $z_{trop}$ . The solution is the given by

$$T_{b,atm}(z_g) = T_{b,atm}(z_{trop})e^{-\tau_{trop}} + T_{eff}(1 - e^{-\tau_{trop}}), \quad (4.3)$$

where  $\tau_{trop}$  is the optical thickness of the troposphere along the measured propagation path and  $z_g$  the altitude of the instrument. To solve this equation for  $T_{b,atm}(z_{trop})$ ,  $\tau_{trop}$  and  $T_{eff}$  must be determined. For the measurement presented in this thesis an empirical model between the radiance at these frequencies, the surface temperature, and the tropospheric temperature is used [Forkman et al., 2003a] to determine  $T_{eff}$ . The optical thickness,  $\tau_{trop}$ , can then be estimated from

$$\tau = \frac{T_{eff} - T_{b,wings}(z_g)}{T_{eff} - T_{b,wings}(z_{trop})}, \quad (4.4)$$

where  $T_{b,wings}$  is measured brightness temperature at the line wings and  $T_{b,wings}(z_{trop})$

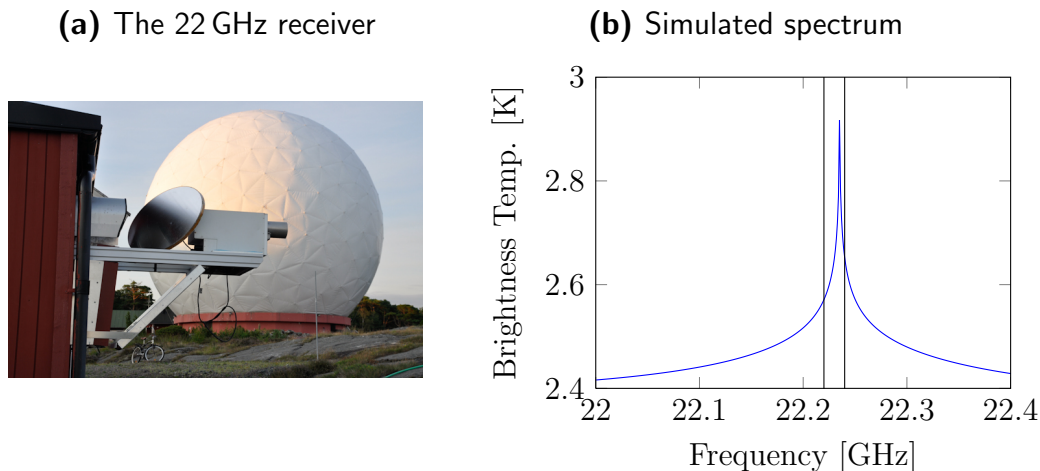


**Figure 4.5:** Panel a: A picture of the 22 GHz radiometer at OSO. Panel b: A simulated atmospheric spectrum of the frequencies around the 22 GHz water vapour line.

the brightness temperature at the wings above the troposphere. For the two ground-based radiometers at OSO  $T_{b,wings}(z_{trop})$  is assumed to be equal to the cosmic background radiation.

### 4.3 The old CO radiometer at OSO

The 115 GHz microwave spectrometer at OSO was designed to measure CO in the mesosphere [Forkman et al., 2003b]. A picture of the instrument is shown in figure 4.4a. Figure 4.4b shows a simulated atmospheric spectrum measured at the station without the influence of the troposphere. The troposphere is not included in the spectrum for pedagogical purposes as the tropospheric attenuation would obscure the CO line. The radio frequency coverage of the instrument is indicated by the two vertical black lines. The CO line at 115.27 GHz is situated near an O<sub>3</sub> line at 115 GHz and on the wing of a wide O<sub>2</sub> line located at 118 GHz. The 115 GHz radiometer at OSO was operated from 2002 to 2008 when it was disassembled for a major overhaul (see chapter 5.3). The six year time series from the OSO radiometer is the longest continuous ground based observation of CO in the mesosphere.

### 4.4 The water vapour radiometer at OSO

The 22 GHz microwave spectrometer at OSO (figure 4.5a) measures water vapour in the mesosphere [Forkman et al., 2003a]. Just like CO, water vapour is an excellent tracer of mesospheric dynamics due to its long photochemical lifetime in the mesosphere. Water vapour in the mesosphere is either water formed through the oxidation of methane, or water transported into the middle atmosphere through the tropical

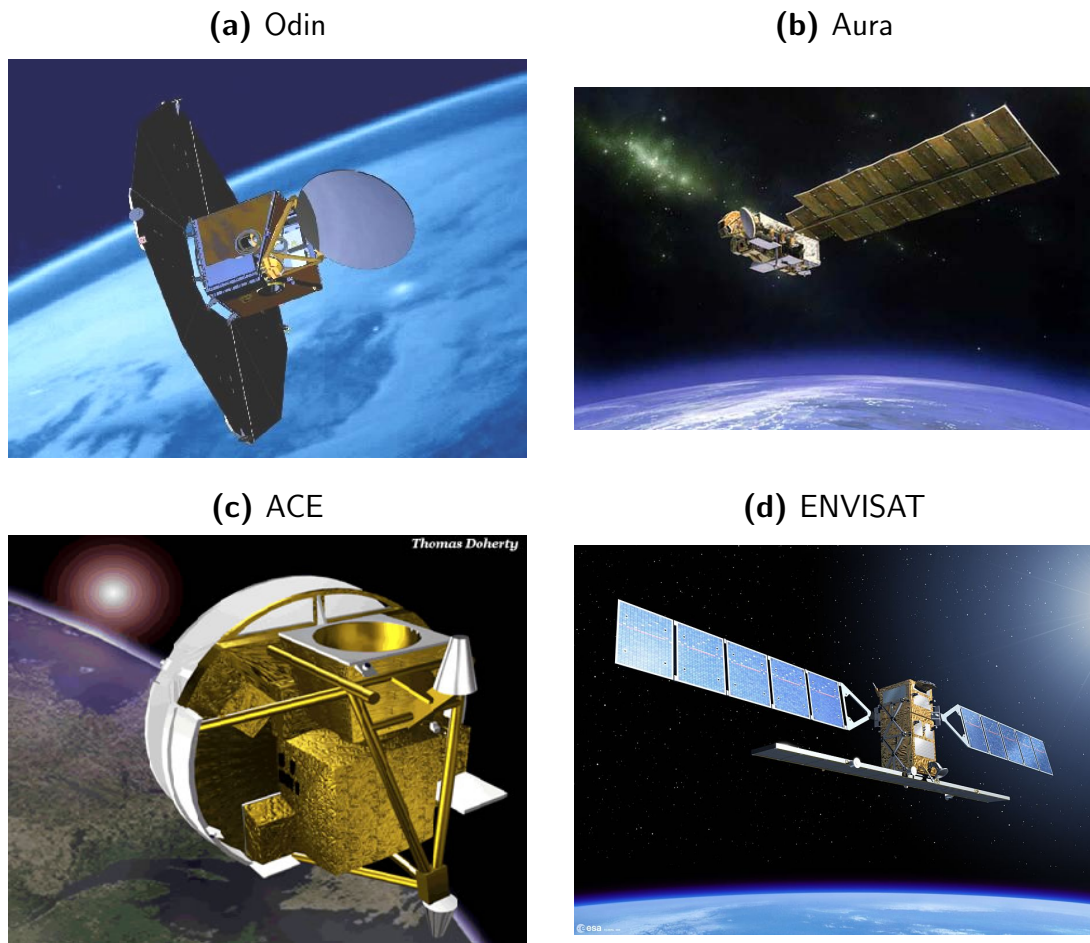


**Figure 4.6:** Satellites used in the validation of the 115 GHz CO radiometer at OSO

tropopause. This means that monitoring water vapour in the mesosphere can help us understand the influences of anthropogenic methane emissions on the mesosphere as well as provide information about the transport mechanics in the tropical tropopause.

Figure 4.5b shows a simulated atmospheric spectrum at the tropopause above OSO. The radio frequency coverage of the receiver is marked by the two black lines. The instrument has operated since 2001 and has provided over 10 years of data to the NDACC database.

## 4.5 Satellites instruments

In our paper, “Six years of mesospheric CO estimated from ground-based frequency-switched microwave radiometry at 57° N compared with satellite instruments“, the CO radiometer at OSO is compared with measurements from several satellite instruments. During 2002-2008, instruments on four different satellites measured the CO concentration in the mesosphere. The satellites are depicted in figure 4.6, and are

ACE, Aura, Odin and ENVISAT.

The Canadian Atmospheric Chemistry Experiment (ACE) was launched by NASA on 12 August, 2003 [Bernath et al., 2005]. It has a  $74^\circ$  inclined circular orbit at 650 km. The primary instrument on board is the high resolution Fourier transform spectrometer (ACE-FTS) which makes infrared absorption measurements of the atmosphere along the limb using the sun as a source. For carbon monoxide, it measures the absorption in the 1-0 ( $4.7 \mu\text{m}$ ) and 2-0 ( $2.4 \mu\text{m}$ ) vibrational bands, and covers altitudes from 5-105 km under clear-sky conditions. It has a vertical resolution of 4 km, and a precision of better than 10% in the mesosphere [Clerbaux et al., 2008]. However, since it is dependent on the sun as a source of radiation the number of measurements it provides over OSO are fewer than from the instruments performing emission measurements.

The Aura satellite was launched by NASA on 15 July 2004 [Schoeberl et al., 2006]. It flies in a sun-synchronous near-circular polar orbit at 705 km with an equator crossing time of 13.45 (ascending). On board the satellite the Microwave Limb Sounder (MLS) measures the  $J=2 \rightarrow 1$  (230.53 GHz) rotational line of CO. From this it retrieves CO concentrations between 15-85 km, with a vertical resolution of 4-8 km in the mesosphere. The precision of a single retrieved profile is very poor exceeding 100% above 20 km. The basic reason for this poor precision is the low signal to noise ratio in the measurements [Pumphrey et al., 2007]. MLS does however provide numerous of measurements, and by averaging these, the data become useful.

Odin is a Swedish led international satellite project launched on 20. February 2001 [Murtagh et al., 2002]. It flies in a sun-synchronous polar orbit at  $\approx 600$  km with an equator crossing time of 18.00 (ascending). Its sub-millimetre-radiometer (SMR) measures the  $J=5 \rightarrow 4$  (576.27 GHz) rotational transition of CO. It covers altitudes from 20-105 km with a precision of around 20% [Dupuy et al., 2004]. The major issue with the Odin measurements has been a problem with the local oscillator used, resulting in many corrupt spectra. This, combined with the fact that the Odin aeronomy mission shares observation time with the Odin astronomy mission, means that relatively few CO measurements were available for intercomparison with the OSO radiometer.

ENVISAT is a research satellite launched in March 2002 [Louet and Bruzzi, 1999]. It flies in a sun-synchronous polar orbit with a 10.00 equator crossing time (ascending node) and an altitude of 800 km. It measures the 1-0 ( $4.7 \mu\text{m}$ ) CO vibrational band, however, unlike ACE-FTS, it measures emission from this line. The advantage of this method is the ability to measure the concentration of CO independent of illumination conditions. The major disadvantage is that the emission line is highly affected by non-LTE processes, thus requiring a more complicated retrieval scheme. Despite of this a precision of 30% is achieved between 50-70 km [Funke et al., 2009].

The accuracy of the different satellite instruments has been estimated in several studies, and is around 10-20% in the mesosphere. For further discussion of this see the appended Paper A.

# Summary and Outlook

## 5.1 Summary Paper A

The large scale dynamics of the mesosphere can be studied by the use of tracer species. These are species that have a long photochemical lifetime, and by looking at the distribution of these species compared to their sources, we can determine how they are advected by the general circulation. One such tracer species is carbon monoxide, CO. At the aeronomy station at the Onsala Space Observatory, CO has been measured from a ground-based microwave spectrometer from 2002-2008. Simultaneously there have been several satellites measuring the global distribution of CO. By cross comparing the measurements, we estimate the systematic errors for the different instruments.

Paper A uses four satellites to evaluate the performance of the instrument located at OSO, so that the uniquely long measurement series it provides can be better used for atmospheric studies. The paper concludes that the systematic error in the measurements is less than 20% between 2004-2008. During this period the OSO measurements are consistent with the satellite instruments. However, the measurements show up to 25% higher CO column values above 70 km compared the satellite instruments. This is within the combined error margins of the instruments, but indicate a possible bias in either the ground-based or satellite measurements. In the period between 2002-2004 the consistency between the different measurements is less clear. The differences between the different satellite instruments are  $\pm 50\%$ , and the measured CO concentration from OSO is located somewhere in between.

## 5.2 Summary Paper B

An old meteorologist joke is that “when in doubt go for persistence”, meaning that a good predictor of tomorrows weather is that it will be the same as today. In Paper B we present a retrieval algorithm for ground-based radiometers that take into

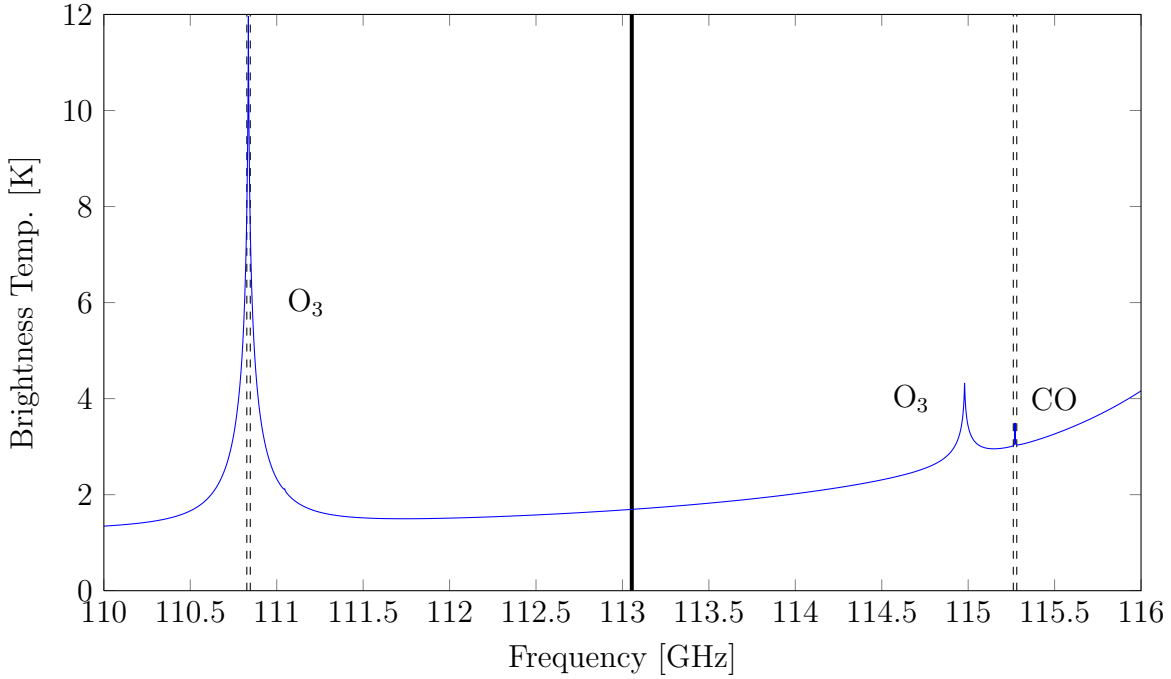


**Figure 5.1:** A simulated spectrum of the relevant frequencies for the new dual band instrument at OSO. The thick solid line shows the LO frequency. The dashed lines shows the RF-coverage of the two bands.

account this temporal correlation in atmospheric states. Retrievals for ground-based instruments are usually performed on each measured spectrum individually. Our paper, “Time series inversion of spectra from ground-based spectrometers”, takes a multi-dimensional approach. Using several spectra, we retrieve an entire time series simultaneously. This is the first time such an approach has been used for a ground-based microwave spectrometer.

The method offers several advantages over traditional single spectrum retrievals. First and foremost it allows for a retrieval to have different temporal resolution at different altitudes. This means that the optimal compromise between signal to noise ratio and temporal resolution can be made at each altitude separately rather than choosing an ad-hoc integration time before performing the retrievals. Other advantages include the possibility to seamlessly interpolate and re-grid data in the temporal domain during the retrieval. These findings should help improving retrievals for future radiometers observing the middle atmosphere.

### 5.3 Outlook

This thesis deals with the retrieval and error characterisation of the measurements from the ground based radiometers at the Onsala Space Observatory. The CO data

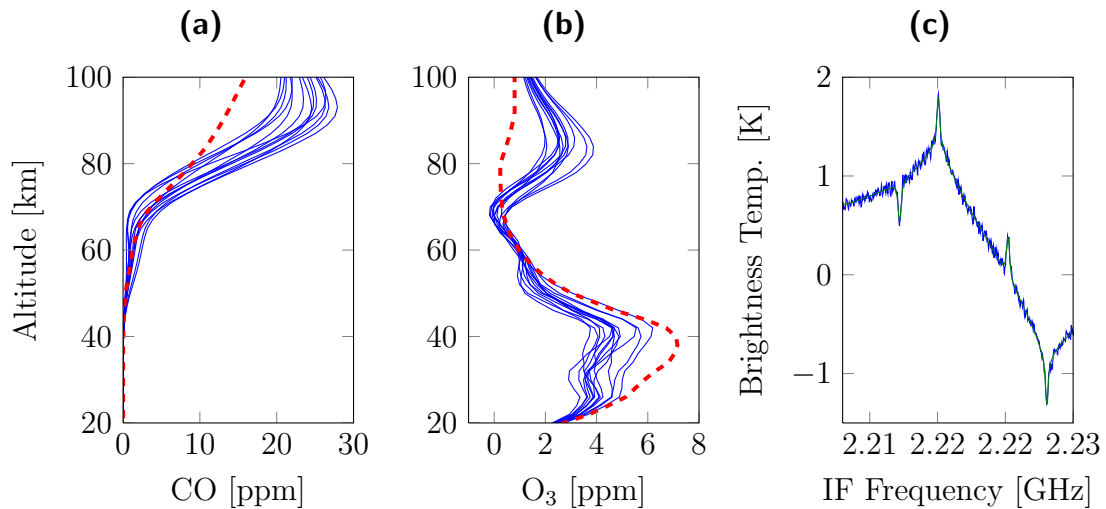


**Figure 5.2:** Preliminary inversions from the new instrument at OSO. Panel a: The retrieved CO profiles (blue). Panel b: The retrieved ozone profiles (blue). The red line shows the a priori profile for the two species. Panel c: A sample spectrum (blue) and the fitted spectrum (green) from the instrument

from the 115 GHz radiometer has been thoroughly evaluated, and are now ready for entrance into NDACC. The retrieval algorithm for the water vapour radiometer was improved, and there is no longer a need to make a selection of whether to have weekly or daily integrated data submitted to NDACC, since the retrieval algorithm handles the averaging directly. The retrieval software used in the retrievals is Qpack [Eriksson et al., 2005]. This software is in large parts developed and maintained at Chalmers. The software is used by several research groups doing atmospheric measurements. The time series inversion method is not fully integrated into this software yet, but will be if the method sparks the interest of research groups using the software.

As mentioned in chapter 4.3, the 115 GHz radiometer was taken down for a major overhaul in 2008. During this overhaul several changes to the instrument was made. One of the changes made was to move the LO frequency to 113.054 and remove the sideband filter. This allows for simultaneously observations of  $O_3$  and CO (see figure 5.1). The instrument became operational again in December 2009, and the process of retrieving the atmospheric concentrations have begun. Figure 5.2c shows an example spectrum from 2009. The major difference in the processing between the old and the new instrument is that due to the large difference in frequency between the two sidebands, a more accurate description of the tropospheric attenuation is needed. The idea is to make use of two total power radiometers (21 and 35 GHz) also located at OSO to determine the amount of liquid and gaseous water. This data will then be used to model the tropospheric attenuation. In the initial retrievals shown in figure 5.2, a simple model atmosphere from the AFGL Atmospheric Constituent Profiles [Anderson et al., 1986] is used for the tropospheric water content.

The initial results are promising. Figure 5.2a shows the retrieved CO concentrations during December 2009. They have the anticipated overall structure, showing that the instrument is working as planned. Figure 5.2b shows the O<sub>3</sub> profiles. These clearly show the ozone layer between 20-50 km and the secondary ozone maximum at 70-90 km. This second maximum arises due to the high downwelling flux of atomic oxygen in the upper winter mesosphere which produces ozone when reacting with molecular oxygen.

The long time series and number of species measured at the OSO aeronomy station makes it useful for studying the dynamics of the mesosphere. The data have already been used in several studies (e.g. Forkman et al. [2005] and Scheiben et al. [2012]). The improved retrieval methods and error characterisation described in this thesis, ensure that the data produced remains relevant into the future, helping us detect and understand any surprises the mesosphere might offer as it adjusts to the ever changing climate.

---

## REFERENCES

---

- G.P. Anderson, SA Clough, FX Kneizys, JH Chetwynd, and EP Shettle. AFGL atmospheric constituent profiles (0-120 km). Technical report, DTIC Document, 1986.
- G. Beig. Long-term trends in the temperature of the mesosphere/lower thermosphere region: 1. Anthropogenic influences. *JGR*, 116(A2):A00H11, 2011.
- G. Beig, P. Keckhut, RP Lowe, RG Roble, MG Mlynczak, J. Scheer, VI Fomichev, D. Offermann, WJR French, MG Shepherd, et al. Review of mesospheric temperature trends. *RG*, 41(4):1–41, 2003.
- P.F. Bernath, CT McElroy, MC Abrams, C.D. Boone, M. Butler, C. Camy-Peyret, M. Carleer, C. Clerbaux, P.F. Coheur, R. Colin, et al. Atmospheric chemistry experiment (ACE): mission overview. *GRL*, 32(15):L15S01, 2005.
- G.P. Brasseur and S. Solomon. *Aeronomy of the middle atmosphere: Chemistry and physics of the stratosphere and mesosphere*, volume 32. Springer, 2005.
- R. T. Clancy and D. O. Muhleman. Ground-based microwave spectroscopy of the earth’s stratosphere and mesosphere. In M. A. Janssen, editor, *Atmospheric remote sensing by microwave radiometry*, pages 335–381. John Wiley, 1993.
- C. Clerbaux, M. George, S. Turquety, K.A. Walker, B. Barret, P. Bernath, C. Boone, T. Borsdorff, JP Cammas, V. Catoire, et al. CO measurements from the ACE-FTS satellite instrument: data analysis and validation using ground-based, airborne and spaceborne observations. *Atmos. Chem. Phys.*, 8:15277–15340, 2008.
- Committee on the Assessment of NASA’s Earth Science Program, Space Studies Board, Division on Engineering and Physical Sciences, and National Research Council. *Earth Science and Applications from Space: A Midterm Assessment of NASA’s Implementation of the Decadal Survey*. The National Academies Press, 2012. ISBN 9780309257022.
- E. Dupuy, J. Urban, P. Ricaud, É. Le Flochmoën, N. Lauté, D. Murtagh, J. De La Noë, L. El Amraoui, P. Eriksson, P. Forkman, et al. Strato-mesospheric measurements of carbon monoxide with the Odin Sub-Millimetre Radiometer: Retrieval and first results. *Geophys. Res. Lett.*, 31(20):101, 2004.

- P. Eriksson, S.A. Bühler, C.P. Davis, C. Emde, and O. Lemke. ARTS, the atmospheric radiative transfer simulator, version 2. *J. Quant. Spectrosc. Radiat. Transfer*, 112(10):1551–1558, 2011. ISSN 0022-4073. doi: 10.1016/j.jqsrt.2011.03.001.
- Patrick Eriksson, Carlos Jiménez, and Stefan A. Bühler. Qpack, a general tool for instrument simulation and retrieval work. *J. Quant. Spectrosc. Radiat. Transfer*, 91(1):47–64, 2005. ISSN 0022-4073. doi: 10.1016/j.jqsrt.2004.05.050.
- P. Forkman, P. Eriksson, and A. Winnberg. The 22 GHz radio-aeronomy receiver at Onsala Space Observatory. *J. Quant. Spectrosc. Radiat. Transfer*, 77(1):23–42, 2003a. ISSN 0022-4073. doi: 10.1016/S0022-4073(02)00073-0.
- P. Forkman, P. Eriksson, A. Winnberg, R.R. Garcia, and D. Kinnison. Longest continuous ground-based measurements of mesospheric CO. *Geophys. Res. Lett.*, 30(10):1532, 2003b.
- P. Forkman, P. Eriksson, and D. Murtagh. Observing the vertical branch of the mesospheric circulation at lat N60° using ground based measurements of CO and H<sub>2</sub>O. *J. Geophys. Res.*, 110(D05):107, 2005. doi: 10.1029/2004JD004916.
- H.H. Frisinger. Aristotle’s Legacy in Meteorology. *BAMS*, 54:198–204, 1973.
- B. Funke, M. López-Puertas, M. García-Comas, GP Stiller, T. Von Clarmann, M. Höpfner, N. Glatthor, U. Grabowski, S. Kellmann, and A. Linden. Carbon monoxide distributions from the upper troposphere to the mesosphere inferred from 4.7  $\mu\text{m}$  non-local thermal equilibrium emissions measured by MIPAS on Envisat. *Atmos. Chem. Phys.*, 9:2387–2411, 2009.
- M.I. Hegglin and S. Tegtmeier. The SPARC Data Initiative. *Sparc Newsletter*, 36: 22–23, 2011.
- James R. Holton. *An Introduction to Dynamic Meteorology*, volume 48 of *International Geophysics Series*. Academic Press, 3 edition, 1992. ISBN 0-12-354355-X.
- M. Lopez-Puertas and F. W. Taylor. *Non-LTE Radiative Transfer in the Atmosphere*. Series on Atmospheric, Oceanic and Planetary Physics. World Scientific Co. Pte. Ltd., River Edge, 2001. ISBN 981-02-4566-1.
- J. Louet and S. Bruzzi. ENVISAT mission and system. In *Geoscience and Remote Sensing Symposium, 1999. IGARSS’99 Proceedings. IEEE 1999 International*, volume 3, pages 1680–1682. IEEE, 1999.
- G. L. Manney, R. S. Harwood, I. A. MacKenzie, K. Minschwaner, D. R. Allen, M. L. Santee, K. A. Walker, M. I. Hegglin, A. Lambert, H. C. Pumphrey, P. F. Bernath, C. D. Boone, M. J. Schwartz, N. J. Livesey, W. H. Daffer, and R. A.

- Fuller. Satellite observations and modeling of transport in the upper troposphere through the lower mesosphere during the 2006 major stratospheric sudden warming. *ACP*, 9(14):4775–4795, 2009. doi: 10.5194/acp-9-4775-2009. URL <http://www.atmos-chem-phys.net/9/4775/2009>.
- D. Murtagh, U. Frisk, F. Merino, M. Ridal, A. Jonsson, J. Stegman, G. Witt, P. Eriksson, C. Jiménez, G. Megie, J. de La Noë, P. Ricaud, P. Baron, J. R. Pardo, A. Hauchcorne, E. J. Llewellyn, D. A. Degenstein, R. L. Gattinger, N. D. Lloyd, W. F. J. Evans, I. C. McDade, C.S. Haley, C. Sioris, C. von Savigny, B. H. Solheim, J. C. McConnell, K. Strong, E. H. Richardson, G. W. Leppelmeier, E. Kyrölä, H. Auvinen, and L. Oikarinen. An overview of the Odin atmospheric mission. *Can. J. Phys.*, 80:309–319, 2002.
- NDACC. Network for the Detection of Atmospheric Composition Change (NDACC). <http://www.ndsc.ncep.noaa.gov/>, Dec 2012.
- H. C. Pumphrey, M.J. Filipiak, N.J. Livesey, M.J. Schwartz, C. Boone, K.A. Walker, P. Bernath, P. Ricaud, B. Barret, C. Clerbaux, R.F. Jarnot, G.L. Manney, and J.W. Waters. Validation of middle-atmosphere carbon monoxide retrievals from MLS on Aura. *J. Geophys. Res.*, 112:D24S38, 2007.
- D. Rees, JJ Barnett, and K. Labitzke. COSPAR International Reference Atmosphere: 1986. Pt. 2: Middle atmosphere models. *ASR*, 10, 1990.
- C.D. Rodgers. *Inverse methods for atmospheric sounding: Theory and practice*. World Scientific, Singapore, 2000.
- K. Rohlfs and T. L. Wilson. *Tools of Radio Astronomy*. Springer-Verlag, Berlin, 2008.
- D. Scheiben, C. Straub, K. Hocke, P. Forkman, and N. Kämpfer. Observations of middle atmospheric H<sub>2</sub>O and O<sub>3</sub> during the 2010 major sudden stratospheric warming by a network of microwave radiometers. *ACP*, 12(16):7753–7765, 2012. doi: 10.5194/acp-12-7753-2012.
- M.R. Schoeberl, A.R. Douglass, E. Hilsenrath, P.K. Bhartia, R. Beer, J.W. Waters, M.R. Gunson, L. Froidevaux, J.C. Gille, J.J. Barnett, et al. Overview of the EOS Aura mission. *ISETGRS*, 44(5):1066–1074, 2006.
- D.W.J. Thompson, D.J. Seidel, W.J. Randel, C.Z. Zou, A.H. Butler, C. Mears, A. Osso, C. Long, and R. Lin. The mystery of recent stratospheric temperature trends. *Nature*, 491(7426):692–697, 2012.



Six years of mesospheric CO  
estimated from ground-based  
frequency-switched microwave  
radiometry at 57° N compared  
with satellite instruments

**Authors:**

P. Forkman, O.M. Christensen, P. Eriksson, J. Urban, B. Funke

**Bibliography:**

P. Forkman, O.M. Christensen, P. Eriksson, J. Urban, B. Funke. Six years of mesospheric CO estimated from ground-based frequency-switched microwave radiometry at 57° N compared with satellite instruments *Atmos. Meas. Tech.*, 5, 2827-2841, doi:10.5194/amt-5-2827-2012, 2012.





# Six years of mesospheric CO estimated from ground-based frequency-switched microwave radiometry at 57° N compared with satellite instruments

P. Forkman<sup>1</sup>, O. M. Christensen<sup>1</sup>, P. Eriksson<sup>1</sup>, J. Urban<sup>1</sup>, and B. Funke<sup>2</sup>

<sup>1</sup>Department of Earth and Space Sciences, Chalmers University of Technology, Sweden

<sup>2</sup>Instituto de Astrofísica de Andalucía (CSIC), Spain

Correspondence to: P. Forkman (peter.forkman@chalmers.se)

Received: 29 March 2012 – Published in Atmos. Meas. Tech. Discuss.: 1 June 2012

Revised: 29 October 2012 – Accepted: 31 October 2012 – Published: 20 November 2012

**Abstract.** Measurements of mesospheric carbon monoxide, CO, provide important information about the dynamics in the mesosphere region since CO has a long lifetime at these altitudes. Ground-based measurements of mesospheric CO made at the Onsala Space Observatory, OSO, (57° N, 12° E) are presented. The dataset covers the period 2002–2008 and is hence uniquely long for ground-based observations. The simple and stable 115 GHz frequency-switched radiometer, calibration method, retrieval procedure and error characterization are described. A comparison between our measurements and co-located CO measurements from the satellite sensors ACE-FTS on Scisat (v2.2), MLS on Aura (v3-3), MIPAS on Envisat (V3O\_CO\_12 + 13 and V4O\_CO\_200) and SMR on Odin (v225 and v021) is carried out. Our instrument, OSO, and the four satellite instruments show the same general variation of the vertical distribution of mesospheric CO in both the annual cycle and in shorter time period events, with high CO mixing ratios during winter and very low amounts during summer in the observed 55–100 km altitude range. During 2004–2008 the agreement of the OSO instrument and the satellite sensors ACE-FTS, MLS and MIPAS (200) is good in the altitude range 55–70 km. Above 70 km, OSO shows up to 25 % higher CO column values compared to both ACE and MLS. For the time period 2002–2004, CO from MIPAS (12 + 13) is up to 50 % lower than OSO between 55 and 70 km. Mesospheric CO from the two versions of SMR deviates up to  $\pm 65$  % when compared to OSO, but the analysis is based on only a few co-locations.

## 1 Introduction

Above the tropopause, CO is formed in the upper mesosphere/thermosphere mainly by photo-dissociation of CO<sub>2</sub> and the major sink is by reactions with hydroxyl, OH. The vertical volume mixing ratio of middle atmospheric CO is characterized by low values in the stratosphere and a steep vertical gradient in the mesosphere.

The dynamics of the mesosphere is characterized by a seasonally varying global circulation, driven by the meridional temperature gradient, and the breaking of upwelling gravity waves. This global circulation brings down constituents from the upper mesosphere to the lower regions of the mesosphere and further down to the stratosphere at the winter pole region, and the reverse is seen at the summer pole region. Due to its long lifetime (weeks) in the mesosphere, CO is an excellent tracer of mesospheric dynamics, especially at high latitudes where both horizontal motions (e.g. caused by the meandering polar vortex) and vertical motion (e.g. caused by the global circulation) can be studied. Lopez-Puertas et al. (2000) surveyed CO observations and model simulations and showed that the CO abundance undergoes an annual cycle in the high latitude mesosphere and lower thermosphere region, with high values in the winter and low values in the summer. During the last 35 yr, middle atmospheric CO has periodically been observed from a variety of ground-based stations. Waters et al. (1976) was the pioneer in observing the rotational transition of CO at 115 GHz. Clancy et al. (1984) and Bevilacqua et al. (1985) made ground-based microwave observations of the seasonal variation of mesospheric CO. Aellig et al. (1995) made 115 GHz observations

and attributed variations in the CO column density to breaking wave activity in the mesosphere. de Zafra and Muscari (2004) used 230 GHz observations of CO as a tracer of polar mesospheric dynamics. Kasai et al. (2005) made the first CO observations using ground-based solar absorption infrared spectroscopy, Velazco et al. (2007) made a long record of strato-mesospheric CO column values using the same technique. Long-term CO measurements at both 115 GHz (Forkman et al., 2003b) and infrared wavelengths (Borsdorff and Sussmann, 2009) have been compared with data from the Whole Atmosphere Community Climate Model, WACCM. Forkman et al. (2005) used CO measurements to estimate the vertical motion of the global circulation. Burrows et al. (2007) estimated horizontal mesospheric winds at Antarctica by the Doppler shift of ground-based microwave CO measurements. Hoffmann et al. (2011) compared ground-based CO measurements at 230 GHz with different satellite sensors.

The Improved Stratospheric and Mesospheric Sounder (ISAMS) onboard the Upper Atmosphere Research Satellite (UARS) made the first global stratospheric and lower mesospheric CO measurements during 6 months in 1991–1992 (Allen et al., 1999). During the last ten years, several different satellite sensors have been observing mesospheric CO including the microwave limb sounders SMR/Odin (Dupuy et al., 2004) and MLS/Aura (Pumphrey et al., 2007), the sun tracking ACE-FTS/Scisat-1 (Clerbaux et al., 2008) and the infrared limb sounder MIPAS/Envisat (Funke et al., 2009).

The lowest rotational transition of CO is at 115 GHz. The advantage of observing at 115 GHz compared to higher frequency transitions is both that the troposphere is optically thinner at lower frequencies and that pressure broadening exceeds Doppler broadening up to about 70 km altitude, making it possible to estimate vertical profiles of CO up to this altitude and column values above.

Dicke-switching, i.e. signal-reference switching of the receiver, is the standard microwave observation method in order to reduce the effect of gain drift in the receiver system. The intensities of the signal (the sky) and the reference (normally a blackbody load) have to balance each other to neutralize system gain nonlinearities. Frequency-switching, a small shift in the local oscillator frequency between the signal and reference phases, is a Dicke-switching variant. This method is mainly useful for the study of narrow lines like mesospheric CO at 115 GHz. One of the advantages of frequency-switching is that the line is present in both the signal and the reference phases, which doubles the effective observation time compared to “load-switching” where the reference is a blackbody load. The frequency-switching observing technique is commonly used in radio astronomy but more seldom used in microwave remote sensing.

In this study we present ground-based, frequency-switched measurements of mesospheric CO made at the Onsala Space Observatory, OSO, (57.4° N, 11.9° E). This is the longest ground-based measurement series of mesospheric

CO and covers the period 2002–2008. The instrument, calibration and inversion methods are described and the results are compared with data from four satellite instruments. Section 2 introduces our frequency-switched receiver system, Sect. 3 describes the inversions, Sect. 4 presents our results, Sect. 5 covers the satellite comparisons, and Sect. 6 gives a summary and the conclusions.

## 2 Measurement

### 2.1 Instrument and observation technique

Microwave remote sensing permits resolved line measurements of pure rotational transitions, which are sufficiently optically thin to allow observations from the ground. These lines are pressure-broadened in the atmosphere, and therefore the measured shape of the spectrum contains information on the number density of the emitting constituent as a function of pressure. Information of the vertical distribution of the emitting constituent can be estimated using mathematical inversion techniques (see Sect. 3).

We present measurements of CO made by a spectral, frequency-switched, heterodyne receiver used for the CO  $1 \rightarrow 0$  transition at 115.27120 GHz based on a cooled Schottky single-sideband mixer. A block diagram of the receiver is shown in Fig. 1 and technical specifications are given in Table 1. The spectrometer is a 2-bit autocorrelator with 20 MHz bandwidth and 800 delay channels giving a nominal resolution of 25 kHz.

In the frequency-switched radiometer, the local oscillator is tuned between the signal and reference measurements. The intensities of the signal and reference phases balances each other as long as the frequency throw is small (normally  $< 10$  MHz). If the frequency is switched,  $\pm \Delta f$  the observed spectral feature will appear both as a negative and a positive peak separated by  $2\Delta f$  in the spectra. Since we use  $\Delta f = 4$  MHz in the frequency-switching we have 8 MHz between the peaks as seen in Fig. 2. If the observed spectral feature is narrower than  $2\Delta f$  it will not be affected by the switching. Frequency-switching can be performed at high speed (5 Hz), which will remove faster gain variations than traditional load-switching.

### 2.2 Calibration

The sky emission increases with decreasing elevation due to the increasing path length through the atmosphere. At the same time, however, the tropospheric absorption increases and therefore also the system temperature of the receiver. At 115 GHz the troposphere is fairly opaque and model calculations show that elevation angles larger than 30° give the highest signal to system-temperature ratio (Forkman et al., 2003a). For practical reasons we have chosen an elevation angle of 90° but the zenith observation direction also

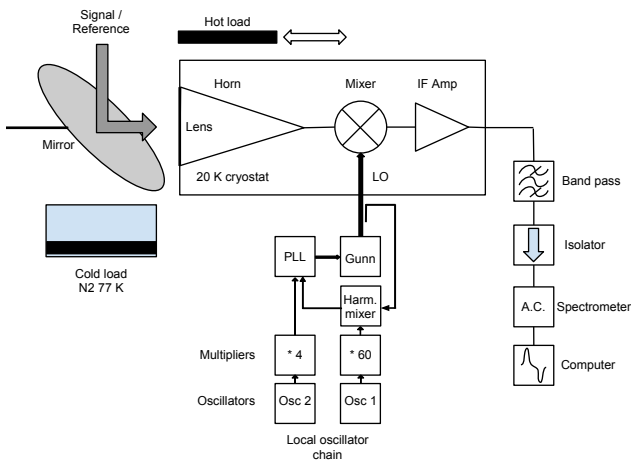


**Fig. 1.** Block diagram of the 115 GHz CO receiver system. The cold load is regularly mounted and used. Since the hot-cold calibrations are performed ahead of the lens, the losses in the lens and in the other components (horn, mixer, etc) along the transmission line are corrected for.

**Table 1.** Receiver specifications.

Radio frequency	115.261–115.281 GHz, SSB
Mirror edge taper	–35 dB
Elevation	90°, fixed
Cryostat window	Teflon lens
Horn	Aluminium, corrugated
Beam width, FWHM (lens included)	3°
First stage	Cooled Schottky mixer, 20 K
Image sideband rejection	Mechanical back short
Image sideband suppression	> 20 dB
Local oscillator (LO)	Gunn oscillator
LO frequency	111.27 GHz
Frequency throw ( $2\Delta f$ )	8 MHz
Mixer IF	$4.0 \pm 0.3$ GHz
Total receiver temperature	~ 325 K
Backend spectrometer	800 channel autocorrelator
Bandwidth	20 MHz
Nominal resolution	25 kHz

minimizes Doppler shift effects due to horizontal movement of mesospheric air.

In microwave radiometry the intensity is normally presented as brightness temperature,  $T_b$ . The receiver output power is calibrated in units of antenna temperature,  $T_a$ . The antenna temperature is the sky brightness temperature distribution weighted with the antenna radiation pattern. Since the beam is quite narrow and the sky brightness temperature increases only slowly, when the elevation changes from zenith to lower elevations (Forkman et al., 2003a) the zenith pencil beam  $T_b$  can be well approximated with the measured  $T_a$ .

The net power reaching the spectrometer consists of two components. The first one is proportional to the sky

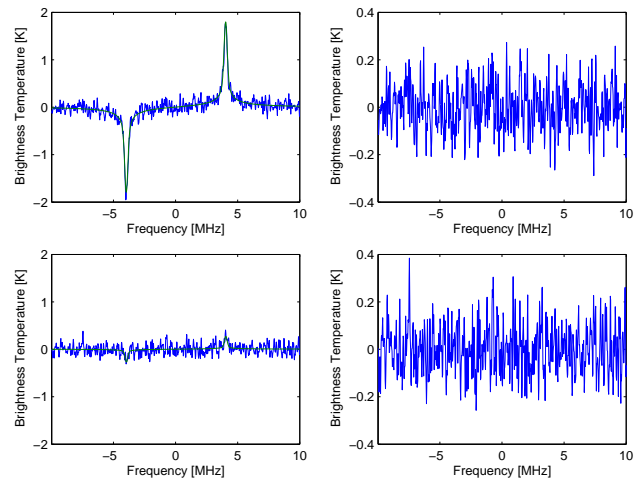


**Fig. 2.** To the left: measured spectra (4 h average) with retrieval fits. To the right: residuals (measured spectrum–fit). The frequencies are given relative to the CO line center. The negative and positive peaks are the result of the frequency throw in the frequency-switching method. The spectra are corrected for baseline features. Note the weak CO signal in the summer (bottom figures).

brightness temperature. The other component is the power generated in the receiver system (lens, horn, mixer, etc), which we identify as the receiver temperature,  $T_{rec}$ . The sum of these components is the system temperature,  $T_{sys} = T_b + T_{rec}$ .

To estimate  $T_{rec}$ , two blackbody loads with brightness temperatures  $T_{hot}$  (ambient load) and  $T_{cold}$  (77 K load) are observed each month. These hot-cold calibrations indicate that the variability of  $T_{rec}$  is less than 5 %.

Before each 15 min observation cycle, a calibration is performed to estimate the zenith sky brightness temperature. This is done by observing the zenith sky and an ambient load

$$\frac{P_{hot} - P_{sky}}{P_{sky}} = \frac{(T_{hot} + T_{rec}) - (T_b(z_0) + T_{rec})}{T_b(z_0) + T_{rec}}, \quad (1)$$

where  $P_{hot}$  and  $P_{sky}$  are the measured powers observing the hot load and the zenith sky respectively,  $T_b(z_0)$  is the zenith sky brightness temperature (observed from the ground,  $z_0$ ).  $T_b(z_0)$  can be derived from the equation above since  $T_{hot}$  and  $T_{rec}$  are known.

Then during the observation cycle we record

$$\begin{aligned} \Delta T_b(z_0) &= T_b(z_0, f_+) - T_b(z_0, f_-) \\ &= \frac{\Delta P}{P_{hot} - P_{sky}} (T_{hot} - T_b(z_0)), \end{aligned} \quad (2)$$

where  $\Delta T_b(z_0)$  is the difference in brightness temperatures between the two frequencies  $f + \Delta f$  and  $f - \Delta f$ ,  $\Delta P$  is the difference between the measured powers at the two frequencies.  $P_{hot}$ ,  $P_{sky}$ ,  $T_{hot}$  and  $T_b(z_0)$  are taken from the calibration.

### 2.3 The tropospheric correction

Assuming a 1-layer model for the troposphere, the microwave radiative transfer equation for a ground-based, zenith-looking observer can be written as

$$T_b(z_0) = T_b(z_{\text{trop}})e^{-\tau} + T_{\text{trop}}(1 - e^{-\tau}), \quad (3)$$

where  $T_b(z_{\text{trop}})$  is the brightness temperature as observed from the tropopause,  $\tau$  is the tropospheric zenith opacity and  $T_{\text{trop}}$  is the effective brightness temperature of the troposphere. If  $T_{\text{trop}}$  and  $\tau$  are considered constant within the frequency throw we get

$$\Delta T_b(z_{\text{trop}}) = \frac{\Delta T_b(z_0)}{e^{-\tau}}. \quad (4)$$

In practice  $\tau$  is calculated from Eq. (3) as

$$\tau = -\ln\left(\frac{T_{\text{trop}} - T_b(z_0)}{T_{\text{trop}} - T_{\text{bg}}}\right). \quad (5)$$

Since the atmospheric opacity is dominated by the contribution from the troposphere, the cosmic background radiation,  $T_{\text{bg}}$ , is used instead of  $T_b(z_{\text{trop}})$  in Eq. (5). This means that the calculated  $\tau$  actually is the atmospheric zenith opacity and hence includes the minor contribution from altitudes above the troposphere (e.g. absorption by stratospheric O<sub>2</sub> and H<sub>2</sub>O).

The frequency-switching only yields  $\Delta T_b(z_0)$ , which is close to zero except for the line peaks.  $T_b(z_0)$  therefore has to be measured separately as done in the calibration.

To be able to estimate  $T_{\text{trop}}$  in Eq. (5), one year of radiosonde data from the Gothenburg-Landvetter Airport (37 km north-east of the observatory) have been processed in forward model calculations (Forkman et al., 2003a). Our estimation of  $T_{\text{trop}}$  is based on the correlation between  $T_{\text{trop}}$  and the ground temperature,  $T_{\text{gr}}$ , but we include the sky brightness temperature,  $T_b(z_0, \nu)$ , to improve the estimate.

$$T_{\text{trop}}(\nu) = \alpha T_{\text{gr}} + \beta T_b(z_0, \nu), \quad (6)$$

where  $\alpha = 0.89$  and  $\beta = 0.10$  for  $\nu = 115$  GHz are found by applying the method of least squares to the processed radiosonde data. The error of the  $T_{\text{trop}}$  estimate was found to be 3.5 K ( $1\sigma$ ). Commonly  $T_{\text{trop}}$  is expressed as  $0.95T_{\text{gr}}$ , but the inclusion of  $T_b(z_0)$  improves the estimate and reduces the error by 10 %.

### 2.4 Calibration errors

An error in the estimate of the receiver temperature,  $T_{\text{rec}}$ , affects the estimation of the sky brightness temperature,  $T_b(z_0)$ . If  $T_{\text{rec}}$  is within the observed variation the error in  $T_b(z_0)$  should be less than 5 %. By comparing the thermal noise,  $\sigma_{\text{tn}}$ , in the measured spectra with theoretical calculations, an estimate of the systematic calibration error can be

found.  $\sigma_{\text{tn}}$  in the spectra can be estimated by fitting a polynomial to the measurement and calculating the standard deviations of the residuals. By using the *radiometric formula* a theoretical estimate of  $\sigma_{\text{tn}}$  is given by

$$\sigma_{\text{tn}} = \frac{K T_{\text{sys}}}{\sqrt{t \Delta \nu}}, \quad (7)$$

where  $t$  is the integration time,  $\Delta \nu$  is the spectrometer resolution and  $K$  depends on the receiver type and configuration. In our case  $K$  reduces to 1.15, which corresponds to the loss of information due to the digitalization of the signal (van Vleck clipping correction), see Rohlfs and Wilson (2008) for further details. By comparing these two calculations of  $\sigma_{\text{tn}}$  we estimate the systematic error in  $T_b(z_0)$  to be less than 5 %.

If the measurement and the tropospheric correction are made in one step (Eqs. 2 and 4) it is clearly seen that errors in the  $T_b(z_0)$  estimation almost cancel out.

$$\Delta T_b(z_{\text{trop}}) = \frac{\Delta P}{P_{\text{hot}} - P_{\text{sky}}} (T_{\text{hot}} - T_b(z_0)) \frac{T_{\text{trop}} - T_{\text{bg}}}{T_{\text{trop}} - T_b(z_0)}. \quad (8)$$

The error in  $\Delta T_b(z_{\text{trop}})$  due to calibration and the tropospheric correction is <2 %.

If  $T_{\text{hot}}$  and  $T_{\text{trop}}$  in Eq. (8) both are approximated with the ambient temperature,  $T_{\text{amb}}$  and  $T_{\text{amb}} \gg T_{\text{bg}}$ , we get

$$\Delta T_b(z_{\text{trop}}) = \frac{\Delta P}{P_{\text{hot}} - P_{\text{sky}}} T_{\text{amb}}, \quad (9)$$

which describes the ‘‘chopper wheel’’ calibration method, which can be used for a quick but not so accurate calibration and correction for the tropospheric attenuation in one step.

In total we believe that the systematic errors from the measurements and the tropospheric corrections, including the effect of the variability of the tropospheric opacity within the measurement cycles, are within 5 % across the used bandwidth.

## 3 Retrievals

### 3.1 Terminology

The inversions were done using the Optimal Estimation Method (OEM) (Rodgers, 2000). The state of the atmosphere and instrument are described by a *state vector*,  $\mathbf{x}$ . A *forward model*,  $\mathbf{f}$ , is then employed to map  $\mathbf{x}$  to a measurement,  $\mathbf{y} = \mathbf{f}(\mathbf{x})$ . The inverse problem consists in finding  $\mathbf{x}$  given some measurement  $\mathbf{y}$ . By linearizing the forward model  $\mathbf{y} = \mathbf{K}\mathbf{x}$  around the a priori atmosphere ( $\mathbf{x}_a$ ), where  $\mathbf{K}$  is the Jacobian or weighting function matrix ( $\partial \mathbf{y} / \partial \mathbf{x}$ ), the problem can be solved using linear algebra.

Doing this and applying OEM, the best estimate of the state vector is

$$\begin{aligned} \hat{\mathbf{x}} &= \mathbf{x}_a + (\mathbf{K}^T \mathbf{S}_\epsilon^{-1} \mathbf{K} + \mathbf{S}_a^{-1})^{-1} \mathbf{K}^T \mathbf{S}_\epsilon^{-1} (\mathbf{y} - \mathbf{f}(\mathbf{x}_a)) \\ &= \mathbf{x}_a + \mathbf{G}_y (\mathbf{y} - \mathbf{f}(\mathbf{x}_a)), \end{aligned} \quad (10)$$

where  $\mathbf{S}_\epsilon$  is the covariance matrix describing the uncertainty in the measurement,  $\mathbf{S}_a$  the covariance matrix for the a priori profile and  $\mathbf{G}_y$  the gain matrix. The relation between the true state, the a priori state and the retrieved state is given by

$$\hat{\mathbf{x}} - \mathbf{x} = (\mathbf{A} - \mathbf{I})(\mathbf{x} - \mathbf{x}_a) + \mathbf{G}_y \mathbf{K}_b (\mathbf{b} - \hat{\mathbf{b}}) + \mathbf{G}_y \Delta \mathbf{f}(\mathbf{x}, \mathbf{b}) + \mathbf{G}_y \boldsymbol{\epsilon}, \quad (11)$$

where  $\mathbf{A}$  is denoted the averaging kernel matrix,  $\mathbf{I}$  is the identity matrix,  $\mathbf{b}$  and  $\hat{\mathbf{b}}$  the true and estimated value of forward model parameter (i.e. line strength),  $\mathbf{K}_b$  is the Jacobian matrix of the parameter ( $\partial y / \partial \mathbf{b}$ ),  $\Delta \mathbf{f}(\mathbf{x}, \mathbf{b})$  are errors in the forward model and  $\boldsymbol{\epsilon}_x$  are errors in the measurement. For a complete definition and derivation see Rodgers (2000). The different terms will be discussed further in Sect. 4.1.

The AVK matrix is defined as  $\mathbf{A} = \partial \hat{\mathbf{x}} / \partial \mathbf{x}$ . It describes the sensitivity of the retrieval to a change in the true state. Each element  $\mathbf{A}_{ij}$  gives the change in the retrieved profile  $\hat{\mathbf{x}}_i$ , resulting from a perturbation in the true profile  $\mathbf{x}_j$ . A row in the AVK matrix can be regarded as a smoothing function (averaging kernel) describing the vertical resolution of the retrievals. The area of this smoothing function is called the *measurement response* and gives a rough indication of the contribution of the measurement to the retrieved value (Baron et al., 2002).

As mentioned in Hoffmann et al. (2011), the AVK will differ in shape depending on whether  $\mathbf{x}$  is representing the volume mixing ratio (VMR AVKs) or the relative change compared to the a priori concentration (fractional AVKs). Both type of AVKs will be presented in this paper for easier comparison with other studies, however we will mainly use the VMR AVKs to characterize the instrument.

### 3.2 Retrieval setup

For the OSO inversions the forward model was provided by ARTS (v2.0) (Eriksson et al., 2011), and the retrieval software is a new version of Qpack (v2.0) (Eriksson et al., 2005). The retrieved quantities are CO volume mixing ratios, temperature, instrumental baselines and a frequency shift in the instrument. Only the CO VMR will be presented as a retrieval product, whereas the three others are retrieved mainly to stabilize the retrieval process. To ensure that the frequency shift is compensated for, the inversions were performed in an iterative leap using a Marquardt-Levenberg algorithm (Marks and Rodgers, 1993).

The spectroscopic line strength and position were taken from the JPL 2001 database (Pickett et al., 1998), whereas the pressure- and self-broadening parameters as well as their temperature dependence coefficients were taken from the HITRAN 2000 database (Rothman et al., 2003). Some of the used CO spectroscopic data are given in Table 2. Since the absorption of  $\text{O}_2$  and  $\text{H}_2\text{O}$  is compensated for in the tropospheric correction (see Sect. 2.3) the only line included in the forward model calculations was the CO line at 115.27 GHz.

**Table 2.** Some of the used CO spectroscopic data.

Center frequency, $f_0$	115.27120 GHz
Line intensity, $I_0$	$9.761128 \cdot 10^{-18} \text{ m}^2 \text{ Hz}^{-1}$
Air-broadened width	$23332.68 \text{ Hz Pa}^{-1}$
Self-broadened width	$25958.54 \text{ Hz Pa}^{-1}$
Reference temperature for broadening parameters	296 K
Temperature dependence exponent for broadening parameters	0.69

The retrieval was performed on a pressure grid ranging from 2738 Pa ( $\sim 10$  km) to 0.87 mPa ( $\sim 130$  km), with a logarithmic spacing of 0.125 decades ( $\sim 2$  km).

The temperature and pressure data were taken from the MSIS90 climatology (Hedin, 1991), and the temperature a priori covariance matrix was given as a matrix with diagonal entries  $\mathbf{S}_{ii} = 25$  K (i.e. standard deviation of 5 K). Furthermore, since the temperature in the real atmosphere is correlated in altitude the non-diagonal elements  $\mathbf{S}_{ij} = \sigma_i \sigma_j \rho_{ij}$  were constructed so that the correlation ( $\rho$ ) would decline linearly with a correlation of 0.37 when the altitude difference (correlation length) between  $i$  and  $j$  was 4 km (roughly based on Eriksson, 2000).

The abundance of CO is highly variable over the year and OEM requires using the best estimate atmosphere as a priori. Therefore a monthly mean from a run of the Whole Atmosphere Community Climate Model (WACCM) (Garcia et al., 2007) was created and used as the a priori profile for the center day in each month. The value for other days were found by linearly interpolating onto each day. To simplify the error analysis, however, the covariance matrix for the a priori data was kept constant (in VMR) throughout the year.

Following Eriksson (2000), the covariance matrix for CO consists of two parts. The first represents the uncertainty of the mean a priori profile for each month. As with temperature, the covariance matrix must also represent correlation in altitude for this error. This was modeled to decline linearly with a correlation length of 8 km. The standard deviation was set to 50 % of the yearly mean of the a priori profiles. The second part represents the natural variability of CO on shorter timescales which was set to 0.5 ppm for all altitudes and with no correlation between the layers.

The OSO instrument had problems with baseline features before an upgrade on 7 January 2004. After this upgrade the baseline variation was reduced significantly. To account for this, an instrumental baseline was retrieved by fitting a 5th order polynomial with a diagonal a priori covariance matrix with entries from 20 K (0th order) to 5 K (5th order) for dates before this upgrade, and entries from 20 K (0th order) to 0.05 K (5th order) for dates after this upgrade. This leads to a different measurement response for the different dates.

Due to the performed Hanning windowing, the thermal noise in neighboring channels is correlated. The average

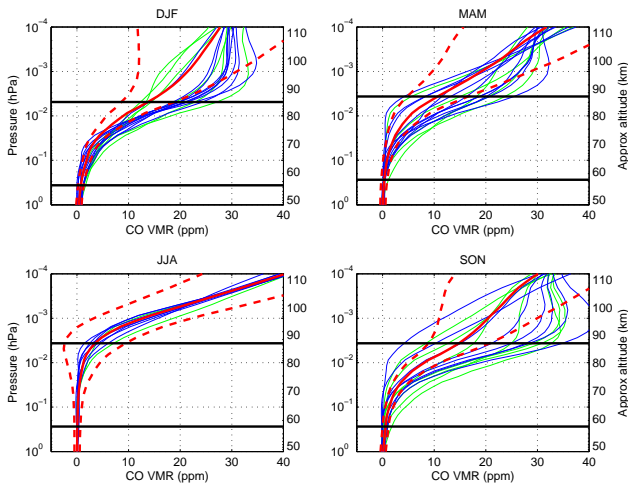


**Fig. 3.** Retrieved profiles 2002–2008 (every 20th profile is plotted for each season). CO volume mixing ratios are plotted against pressure (and altitude). The red line shows the average a priori profile for the season, and the dashed line the standard deviation of the a priori profile. Green lines are retrieved profiles 2002–2004 and the blue lines are profiles 2004–2008. The mean measurement response of the OSO instrument is higher than 0.8 between the black horizontal lines.

channel correlation of the thermal noise was measured to be 1.6 nominal channel widths, so  $S_{\epsilon}$  was given as a covariance matrix with a correlation length of 1.6 nominal channel widths. The magnitude of the thermal noise was estimated in each measurement independently by fitting a polynomial of order 3 to the measurement and calculating the RMS of the residuals at the wings.

#### 4 Results of the OSO measurements

Figure 2 shows a sample spectrum, the corresponding retrieved spectrum and the residuals for a typical winter and summer measurement. The CO line is much fainter during the summer than the winter line due to the strong seasonal cycle of CO (Sect. 1). The residuals are of equal strength, with both summer and winter showing that the system temperature is more or less constant during the year. Example profiles for each season are plotted in Fig. 3.

The shapes of the VMR AVKs are quite similar in both winter and summer. The most notable feature of the VMR AVKs is the negative values around 60 km for the AVKs corresponding to retrieved values above 90 km (pink and black curves in Figs. 4 and 5). Although this looks dramatic, it is important to remember that these AVKs represent the sensitivity to changes in VMR. The concentration of CO is much lower at 60 km than above 90 km, and accordingly the expected variability in CO VMR is also much lower. This implies that the impact of the negative lobes will be small, as the retrieved value follows the product of the AVK value and

the deviation from the a priori (see first term Eq. 11). The corresponding averaging kernels (the rows of AVK matrix) can be seen in Figs. 4 and 5.

Since CO has a very strong vertical gradient, relative changes at altitudes above the target altitude will give a larger effect than relative changes beneath. This changes the shape and area of the fractional AVKs, especially around 70 km during the summer where the fractional AVKs becomes extremely wide. Here strong vertical gradients combined with poor vertical resolution even results in the measurement response of the fractional AVKs to become greater than one. This means that a concentration change of 10 % at one altitude could give a responding change of 20 % at a lower altitude.

This complication is less prominent when using the VMR AVKs, rather than the fractional AVKs, to define the measurement response of the instrument. Note that the measurement response then describes the instruments' sensitivity to changes in vmr rather than changes relative to the a priori. The use of VMR AVKs is motivated by the fact that the strong vertical gradient of CO combined with a meandering vortex can lead to extremely large changes in the true atmosphere relative to the a priori. This variation is easier to describe in VMR rather than relative units, and the sensitive range is therefore given as such. To further address the issue of the poor vertical resolution above 70 km, only the column (rather than individual layers) will be used above this altitude.

The retrievals have an average degree of freedom (trace of the AVK matrix) of 1.8 before 2004 and 2.2 after 2004. The measurement response (VMR) is above 80 % approximately between 55 and 85 km. The vertical resolution within this altitude range is about 15–20 km (see Figs. 4 and 5). The beam of the OSO instrument has a horizontal width of about 4 km in the mesosphere.

The results presented in this paper will be given as the mixing ratios at 36 Pa (55 km), 12 Pa (63 km) and columns above 4 Pa (71 km) where Doppler broadening dominates. The column values are calculated by summing up the number densities from the air pressures below 4 Pa. The number densities are calculated from the retrieved profiles using the a priori temperature profiles.

#### 4.1 Errors

The error of the retrieval is the difference between the true state  $x$  and the retrieved state  $\hat{x}$ . The error can be divided into several parts corresponding to each term in Eq. (11).

The first term is known as the *smoothing error* and represents the error at each altitude, which arises from the limited vertical resolution of the retrieval. When analyzing a profile from a given instrument this has to be taken into account, either by saying that the value at each altitude is the average represented by the AVK or by stating the smoothing error. In this study the averaging kernels of the OSO instrument

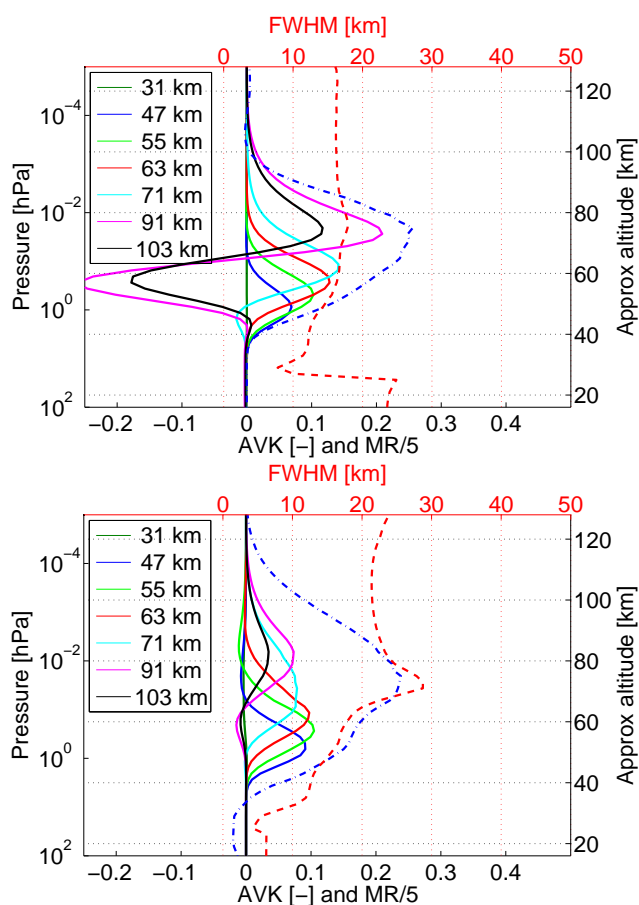


**Fig. 4.** Solid lines show the averaging kernels from 27 December 2005 in vmr (a) and fractional (b) units for different altitudes. The blue dash-dotted line is the measurement response divided by 5. The red dashed line shows the FWHM of the averaging kernels.

is taken into account by Eq. (12) and the smoothing error is thus ignored. The second term is the *model parameter error*, which describes the error in the retrieval arising from the difference between the true value of a forward model parameter  $\mathbf{b}$  and the estimated value  $\hat{\mathbf{b}}$ . This will be discussed further in Sect. 4.2. The third term is the *forward model error*, which comes from direct errors in the forward model from either approximations or not modeled processes. This last term will not be discussed in this paper and is negligible. A thorough validation of ARTS is presented in Melsheimer et al. (2005).

The last term is the *retrieval noise*, which is the error coming from noise in the measured spectra. It is described by the covariance matrix  $\mathbf{S}_m = \mathbf{G}_y \mathbf{S}_e \mathbf{G}_y^T$ . This error is random and will introduce noise into the retrieved profiles. An estimate of this noise is shown as the blue lines in Fig. 6. The dashed (dashed-dot) line shows the value for winter (summer) retrievals and the solid line the mean retrieval noise. The big difference between summer and winter values is due to the low concentration of CO during summer.

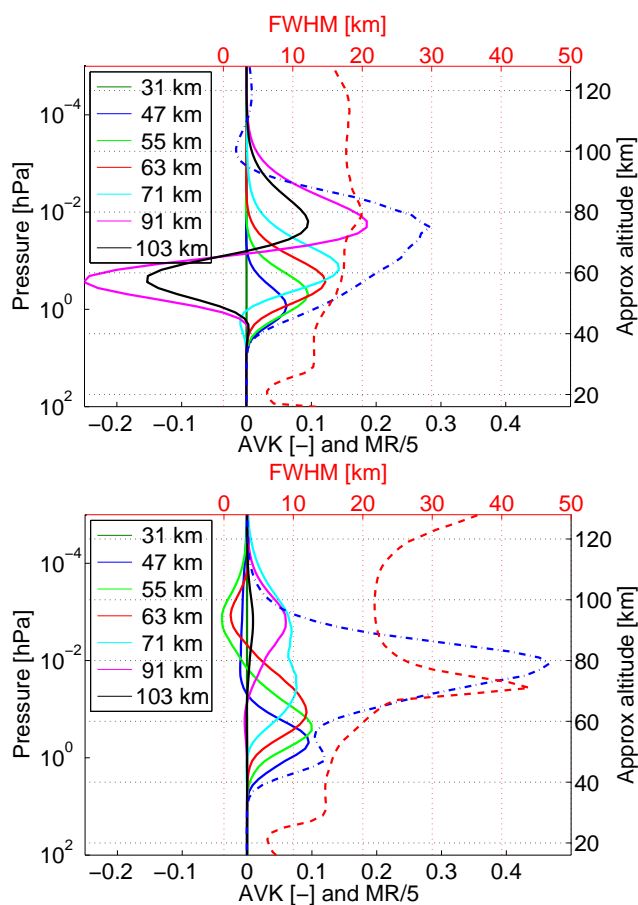


**Fig. 5.** Solid lines show the averaging kernels from 26 June 2006 in vmr (a) and fractional (b) units for different altitudes. The blue dash-dotted line is the measurement response divided by 5. The red dashed line shows the FWHM of the averaging kernels.

## 4.2 Forward model parameter errors

In addition to the errors accounted for in the retrieval, there will be systematic errors from the forward model as well as instrumental errors which might influence the retrievals. To estimate the influence of errors in different retrieval parameters on the results, the retrievals from year 2006 were used. The summer values (JJA) were removed resulting in 177 remaining spectra, which were rerun with the different parameters perturbed with their estimated  $1\sigma$ -error. The differences between the standard and the perturbed inversions show that errors in forward model parameters can lead to a systematic error (bias) as well a decreased precision in each measurement. The systematic error can be described by  $\mathbf{x}_{\text{pert}} = k \cdot \mathbf{x}_{\text{std}}$  at each altitude, where  $\mathbf{x}_{\text{pert}}$  is the value of the perturbed inversion,  $\mathbf{x}_{\text{std}}$  the retrieved value using the standard parameter values and  $k$  a coefficient which can be found by linear regression. The estimated relative error can then be expressed as  $|100 \cdot (k - 1)| \%$  (Pumphrey et al., 2007). The decreased precision is estimated by the standard deviation of

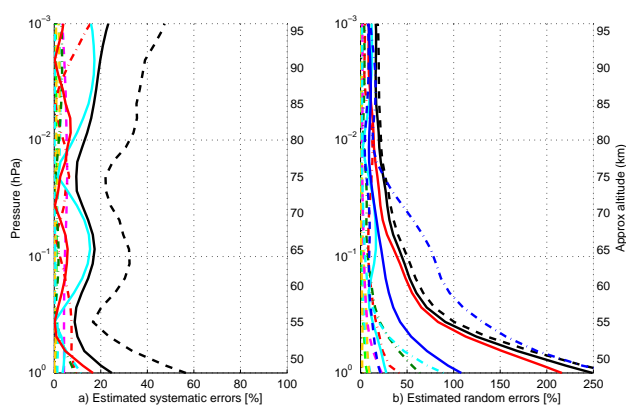


**Fig. 6.** In (a) the estimated systematic errors and in (b) the random errors. The colored (except blue) lines show the mean relative change (a) and standard deviation (b) in the retrieved value at each altitude as the different forward model parameters are perturbed. The forward model parameters are: line-strength,  $I_0$ , (green-dashed), temperature profile,  $T$ , (cyan-dashed), pressure broadening parameter,  $\gamma_P$ , (yellow-dashed), temperature coefficient for the broadening parameter,  $\alpha_P$ , (yellow-dashed-dot), a priori profile,  $x_a$ , (red-dashed-dot), 50 % a priori uncertainty,  $S_x$ , (green-dashed-dot), removing natural variability from a priori uncertainty,  $S_x$ , (red-solid), a priori uncertainty for the polynomial fit (cyan-dashed-dot), calibration errors (magenta-dashed-dot) and backend channel broadening error (cyan). The black line in both figures is the root-sum-square of the parameter errors. In (a) the black-dashed is the sum of the errors. The dark blue lines in (b) show the retrieval noise from 1 January 2006 (dashed), 2 September 2006 (dashed-dot) scaled with the a priori profile for the respective day as well as the average retrieval noise (solid). The black dashed line in (b) is the root-sum of the average retrieval noise (blue-solid) and the total parameter variability (black-solid).

the relative difference between the standard and perturbed inversions (i.e. scaled with the a priori).

The different forward model parameters tested include the line strength of the CO transition, the pressure broadening parameter and the instrument backend channel response. In addition, the a priori temperature profile, a priori CO profile, a priori uncertainty and size of the polynomial baseline fit were perturbed to test the possible systematic errors arising from different retrieval parameters.

For the spectral parameters the error estimates were done by comparing the values for HITRAN 2000, HITRAN 2008 and JPL 2001. If the discrepancies between the databases were bigger than the given error estimate in the database the discrepancy was used, if not the error estimate from the database was used. This gives a line strength  $I_0$  uncertainty of 1 % (JPL-database), a pressure broadening parameter  $\gamma_P$  uncertainty of 10 % (HITRAN 2000 uncertainty) and an uncertainty in the temperature coefficient  $\alpha_P$  of the pressure broadening parameter of 10 % (difference between HITRAN 2000 and HITRAN 2008). Errors in the self-broadening parameters were found to be insignificant to the retrieval and will

not be presented in this paper. In total, the spectroscopic parameters together give errors of less than 5 % in the retrievals.

To investigate the influence of the calibration errors, the spectra were simply multiplied with  $1 \pm 0.05$  to simulate the  $1\sigma$  calibration error (see Sect. 2.4). To test the influence of the a priori, the CO profile was perturbed by 50 % and the standard deviation for the a priori uncertainty covariance matrix was changed with 50 %. In addition, another test was done where the part representing the natural variability (0.5 ppm at all altitudes) was removed from the uncertainty matrix, and only the uncertainty in a priori mean was used. The temperature profile was perturbed by 5 K ( $1\sigma$  error for MSIS90 is 3 K) to take errors in temperature into account. The polynomial baseline fit in the retrieval had its a priori variance multiplied and divided by 4.

Figure 6a shows the estimated systematic error for the different parameters and their root-sum-square (solid black). This estimate indicates the total systematic error expected in the measurements. The solid black line shows the sum of all the errors, this represents a worst case scenario for systematic errors which we will use before 2004.

In addition to the systematic errors, uncertainties in the forward model and retrieval parameters also lead to a decreased precision. Figure 6b shows the standard deviation from each parameter and their root-sum-square (solid black). Combined (root-sum-square) with the average retrieval noise (blue solid) an estimate of the precision of the measurements is obtained and shown as the black dashed line in Fig. 6b.

The total estimated averaged systematic error between 55–85 km is in the order of 15 % for profiles and 10 % for column values. The worst case error, the sum of the different errors, is of the order of 25 % for profiles and 20 % for the column values. Estimated average random errors between 55–85 km is 30–50 %, but is significantly worse when the concentration of CO is low. The random errors mainly comes from the retrieval noise, and depend heavily on the a priori uncertainty at those altitudes (red curve Fig. 6), with a higher uncertainty leading to more noise. The retrieval noise from one such date (2 September 2006) is shown as the dashed-blue line in Fig. 6b.

## 5 Comparison

### 5.1 Satellite instruments

The four satellite instruments which observed mesospheric CO during the time period 2002–2008 are the sun tracking ACE-FTS on Scisat-1 (Clerbaux et al., 2008), the microwave limb sounder MLS on Aura (Pumphrey et al., 2007), the infrared limb sounder MIPAS on Envisat (Funke et al., 2009) and the microwave limb sounder SMR on Odin (Dupuy et al., 2004). The temporal and mesospheric vertical coverage are different for the four satellites. Table 3 gives the

**Table 3.** Satellite and data characteristics.

Satellite instrument	ACE-FTS	Aura-MLS
Reference	Clerbaux et al. (2008)	Pumphrey et al. (2007)
CO data version	V 2.2	V-3-3
Measurement principle	Sun tracking, absorption	Limb sounding, emission
Wavelength or frequency	2.3 & 4.7 $\mu\text{m}$	230 GHz
Launch	12 August 2003	15 July 2004
Orbit inclination	74°	90°
Vertical range	6–100 km	16–80 km
Vertical resolution (mesosphere)	4 km	7–8 km
Horizontal resolution (mesosphere)	500 km	200 km
Systematic errors (above 60 km)	Better than $\pm 25\%$	$\pm 20\%$
Co-location range satellite-OSO	< 1500 km & < $\pm 20\%$ PV	< 1500 km & < $\pm 20\%$ PV
Co-located measurement days	126	618
Satellite instrument	Envisat-MIPAS	Odin-SMR
Reference	Funke et al. (2009)	Dupuy et al. (2004)
CO data version	V3O(12 + 13) 2003–2004	V021 (new version)
CO data version	V4O(200) 2005–2008	V225 (old version)
Measurement principle	Limb sounding, emission	Limb sounding, emission
Wavelength or frequency	4.7 $\mu\text{m}$	576.4 GHz
Launch	1 March 2002	20 February 2001
Orbit inclination	98.6°	97.8°
Vertical range	6–70 km	17–110 km
Vertical resolution (mesosphere)	10 km	3 km
Horizontal resolution (mesosphere)	500 km	500 km
Systematic error (50–70 km)	$\pm 10\%$	Not available
Co-location range satellite-OSO	< 1500 km & < $\pm 20\%$ PV	< 1500 km & < $\pm 20\%$ PV
Co-located measurement days	418	22

characteristics of the four satellite sensors. As seen in Table 3, we use two different CO datasets for MIPAS and SMR. For MIPAS we use version V3O.CO.12 and V3O.CO.13 obtained from high spectral resolution measurements during 2003–2004 and version V4O.CO.200 in the period 2005–2008 when the MIPAS spectral resolution was reduced as consequence of an instrumental failure. All MIPAS observations used here were taken in the nominal observation mode covering tangent heights within 6–70 km. For SMR we use both the older v225 and the newer v021. V021 is an extended dataset compared to v225 using all the available observation modes. V225 has been used in previous comparisons (e.g. Clerbaux et al., 2008).

## 5.2 Comparison procedure

Side-looking satellites and a zenith-looking ground-based instrument do not observe the same air volume. Comparisons between satellite- and ground-based instruments are therefore complicated. All the satellites report data from a 100 times longer horizontal path than OSO but their vertical resolution are up to four times better. Differences in vertical resolution can be compensated for by using the averaging kernels of the instruments but differences in horizontal resolution are harder to adjust for. A second issue is the co-location criterion to apply. At periods when small horizontal variations of CO are expected in the mesosphere (as in the summer)

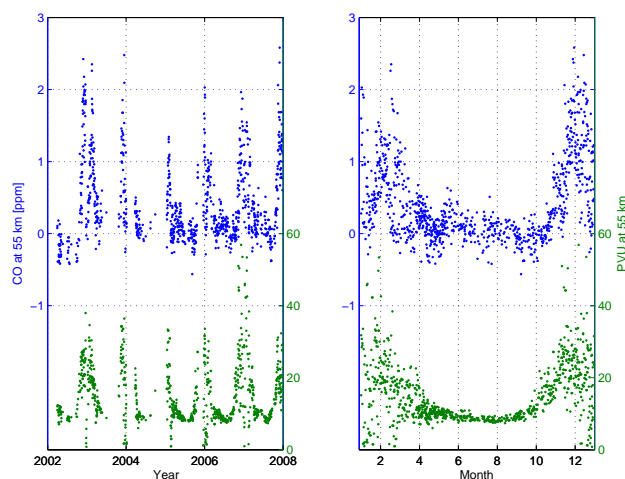


**Fig. 7.** CO volume mixing ratio and PV above OSO at 55 km altitude. To the left: the time series 2002–2008. To the right: the data from the different years stacked together. The modified Ertel's PV is used and 1 PVU =  $10^{-6} \text{ K m}^2 \text{ s}^{-1} \text{ kg}^{-1}$ . The overall correlation between CO and PV is 0.63.

the air above OSO should be rather similar to air inside the co-location radius of 1500 km chosen in this study. A higher variability is expected in the wintertime when the movement of the polar vortex brings in or out CO rich air above the OSO instrument, and the concentration can vary substantially both

within 1500 km radius from OSO and along the horizontal paths of the satellite beams. These deviations can partly be compensated for by using observed potential vorticity as a supplementary co-location criteria.

The polar vortex builds up in the autumn and breaks down in the spring. The potential vorticity (PV) of an air parcel is a measure of the position of the air parcel relative to the polar vortex. Figure 7 shows the OSO CO volume mixing ratio at 55 km together with the modified Ertel's PV (Lait, 1994), calculated from the ECMWF operational dataset at 55 km during the time period 2002–2008. Figure 7 shows both a time series for the different years and the data for the different years stacked together to clearly see the seasonal variation. Both the CO mixing ratio and the PV have a steep and distinct increase in the autumn. The winter is characterized by the meandering of the polar vortex, which brings in or out CO rich air from the polar region and this causes fast variations of both CO mixing ratio and PV. The decrease in CO and PV in the spring is both less steep and less distinct than the increase in the autumn. The PV is low and stable in the summer and the CO mixing ratio is close to zero but show a high variability in the measurements. The high variability is explained by the faint CO signal in the summer which gives a low signal to noise ratio. The overall correlation between the CO mixing ratio and PV is 0.63.

The co-location criteria was chosen as follows: the temporal co-location criteria was set to the same date for satellite and OSO. The air volume measured by the satellite had to be within a radius of 1500 km from OSO. The potential vorticity (PV) of the air volume measured by the satellite had to be within 20 % of the PV above OSO (Hoffmann et al., 2011 used a similar co-location procedure). The PV data were taken from the ECMWF operational data set at the potential temperature level of 2000 K ( $\sim 50$  km altitude) and the modified Ertel's PV (Lait, 1994) was calculated for both satellites and OSO. Figure 8 show the co-located positions for the four satellites.

For the comparison, the satellite data were interpolated onto the OSO retrieval grid. In the relevant vertical range the best resolution of the different satellites are roughly 4 km, which is about twice the interpolation resolution used. Hence the interpolation errors should be small ( $< 1\%$ ) which also is confirmed in a test (not shown).

For grid points outside the valid data points for the satellite the OSO a priori CO data were used. To take into account the different vertical resolution of the instruments the satellite data was convolved with the averaging kernels,  $A$ , of the OSO instrument (Rodgers and Connor, 2003)

$$\mathbf{x}_s = \mathbf{x}_a + \mathbf{A}(\mathbf{x}_{\text{sat}} - \mathbf{x}_a), \quad (12)$$

where  $\mathbf{x}_s$  is the smoothed version of the satellite profile  $\mathbf{x}_{\text{sat}}$ , and  $\mathbf{x}_a$  is the OSO a priori profile.

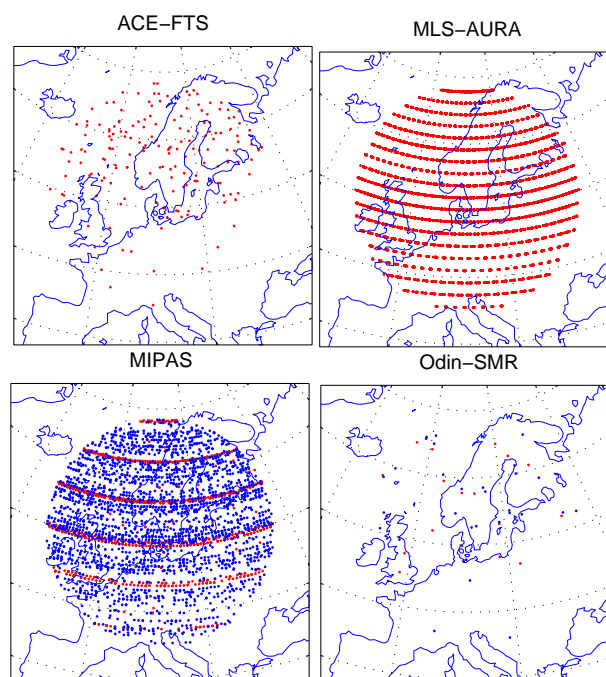


**Fig. 8.** Satellite (co-location) positions. The dots indicate the satellite positions within 1500 km radius from OSO, which also fulfill the PV criteria. In the MIPAS co-location map red/blue dots show (12 + 13)/(200) data, respectively. In the Odin co-location map red/blue show v225/v021, respectively.

### 5.3 Results of the satellite comparison

The satellite comparison is divided in the time periods: 2002–2004 and 2004–2008. As mentioned in Sect. 3.2 there were baseline features in the OSO spectra 2002–2004 that may have affected the retrieved vertical profiles. These features disappeared when the local oscillator chain of the instrument was rebuilt in the beginning of 2004. Figure 9 shows time series of CO from OSO, MIPAS (12 + 13) and SMR (021 + 225) for the time period 2002–2004 and Fig. 10 show time series from OSO, ACE, MIPAS (200), MLS and SMR (225) for the time period 2004–2008. Both figures show CO volume mixing ratios at 55 and 63 km and column values above 71 km. No column values are presented for MIPAS and MLS since the nominal MIPAS CO observations are not vertically resolved above 70 km, and the upper limit for MLS is about 80 km. Figure 11 shows the WACCM mean CO volume mixing ratio and the mean CO number densities. The main contribution for the column values is from altitudes  $< 100$  km, even if the volume mixing ratio is increasing with altitude. This is explained by the exponential decrease in air pressure, and hence in air density, with altitude.

As seen in Figs. 9–10 all instruments show the same general features in both the annual cycle and in sporadic events. The noticeable difference between OSO and the satellites in

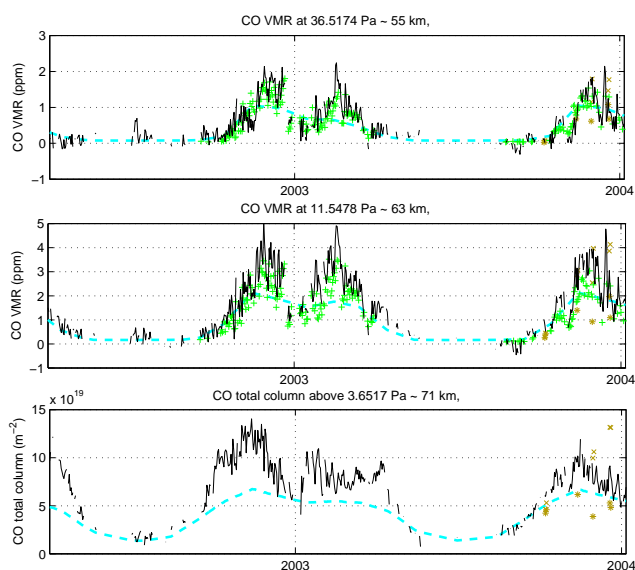


**Fig. 9.** Time series of CO mixing ratio at 55 km and 63 km and columns above 71 km for the time period 2002–2004 are shown: OSO (black), MIPAS (12 + 13, green plus), SMR (V021, brown cross; V225, brown stars) and a priori (cyan).

these figures is mainly the higher values of OSO compared to MIPAS (12 + 13) at 63 km (Fig. 9).

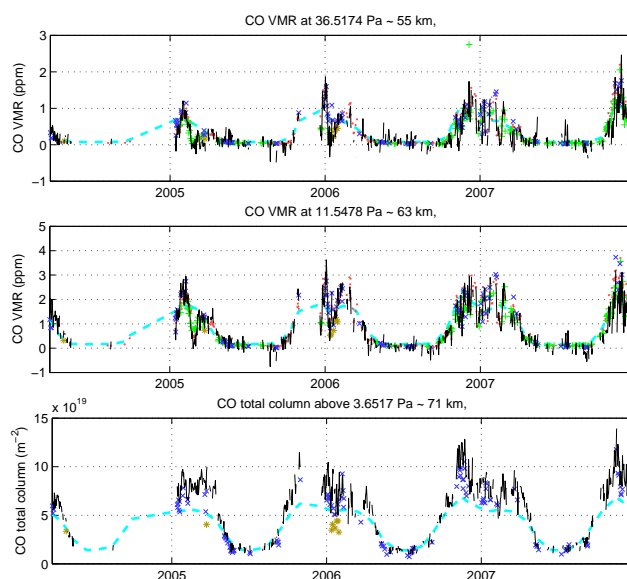
Figures 12–13 and Table 4 give a more detailed view of the comparison. Figure 12 shows the mean relative differences between the satellites and OSO for the time periods 2002–2004 and 2004–2008. The differences are discussed for each satellite instrument later in this section.

Figure 13 shows the mean absolute and relative standard deviations between OSO and the satellites. These deviations originate from noise in the different instruments, from fluctuations due to insufficient co-location and forward model/retrieval parameters. Below 65 km the OSO measurement response gradually decreases, which explain the increase of the deviations below this altitude.

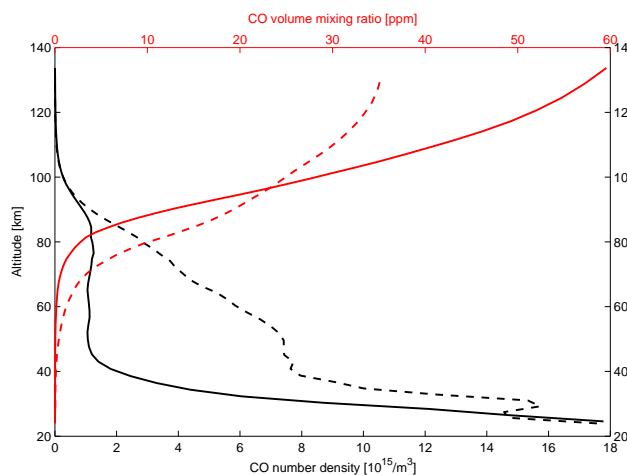
Table 4 gives a supplement to Figs. 12–13 showing the mean relative differences, the mean standard deviations and the mean correlation between OSO and the satellites. The correlation of the data from OSO and the satellite instruments is high.

The OSO summer CO spectra have a very low signal to noise ratio leading to a higher relative noise (Figs. 2b and 6). This gives a high variability in the retrieved summer mixing ratios (Fig. 10). The summer values are therefore excluded in Figs. 12–13 and Table 4 to avoid the noisy OSO summer measurements interference in the satellite comparison.

Taken into account the systematics errors of OSO ( $\leq 15\%$ ) and the satellites (20–30%, see Table 3) OSO overlaps the satellites in the time period 2004–2008 when OSO is compared to ACE, MIPAS (200) and MLS.



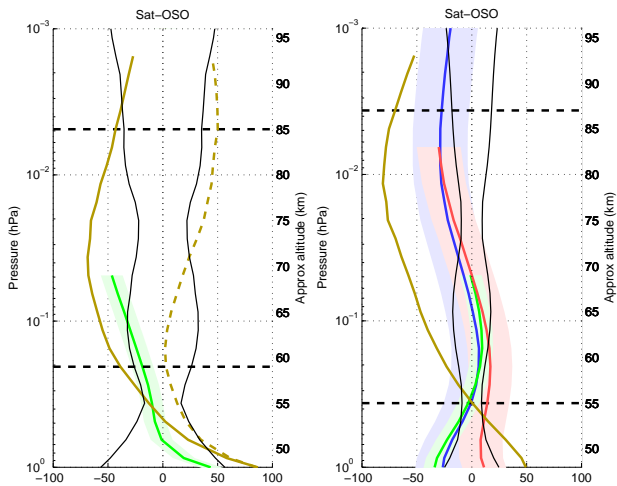
**Fig. 10.** Time series of CO mixing ratio at 55 km and 63 km and columns above 71 km for the time period 2004–2008 are shown: OSO (black), FTS (blue cross), MIPAS (200, green plus), MLS (red dots), SMR (V225, brown stars) and a priori (cyan dashed).



**Fig. 11.** The number density of CO (black) and the volume mixing ratio of CO (red) versus altitude. The data shown are the mean summer (solid) and mean winter (dashed) OSO a priori from WACCM. The main contribution to the column above 70 km originates from altitudes  $\leq 100$  km altitude.

### 5.3.1 ACE and MLS

The CO mixing ratios from OSO and the satellites MLS and ACE agree well and have a high correlation at all altitudes. Between 55 and 70 km the difference in mixing ratios between OSO and ACE and MLS is less than 15% (Fig. 12 and Table 4). The deviation between ACE and MLS, as seen in Fig. 12, has been reported earlier by Pumphrey et al. (2007) and Clerbaux et al. (2008). As seen in both Fig. 12 and



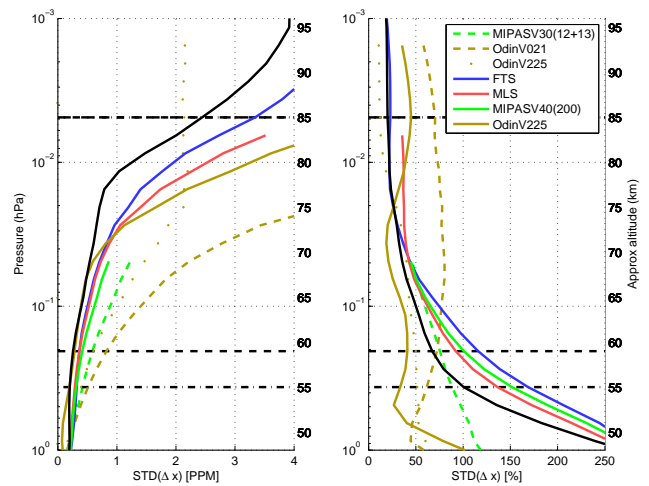
**Fig. 12.** Mean relative differences between satellites and OSO; (Left): the time period 2002–2004, MIPAS (12 + 13, green), SMR (V021, dashed brown) and SMR (V225, solid brown). (Right): the time period 2004–2008, FTS (blue), MIPAS (200, green), MLS (red) and SMR (V225, brown). The deviating lengths of the satellite profiles is explained by the different vertical coverage of the satellites. The shaded areas show the estimated systematic error of the different satellites. The vertical black lines are the estimated systematic errors of the OSO instrument, 2002–2004 the worst case systematic error is used due to baseline problems (see Sect. 4.2). The horizontal black dashed lines show the vertical limits of the OSO observations. The summer values are excluded.

Table 4 OSO has higher CO mixing ratios above 70 km compared to ACE and MLS leading to 25 % higher CO column values ( $> 71$  km). The MLS column values are close to the OSO a priori since the upper limit of MLS is about 80 km and we use the a priori CO data for grid points outside the vertical range of the satellite (see Sect. 5.2).

### 5.3.2 MIPAS

MIPAS (200) shows only a small deviation in CO mixing ratios compared to OSO. MIPAS (12 + 13) does not show the same good agreement when compared to OSO, it has up to 50 % lower values than OSO above 55 km. MIPAS (12 + 13) and MIPAS (200) have the same vertical coverage though MIPAS (200) is slightly better vertically sampled (due to shorter integration time). Resulting vertical resolutions of retrieved profiles, however, are quite similar.

Up to March 2004 only MIPAS (12 + 13) data are available and after March 2004 only MIPAS (200) data. In this comparison we have no overlap between MIPAS (12 + 13) and the other satellites except a few collocations with SMR (021 + 225). Clerbaux et al. (2008) compared CO data from the beginning of 2004 from MIPAS (9 + 10) and ACE and found that the CO mixing ratios from MIPAS (9 + 10) is within  $\pm 26$  % of the ACE mixing ratios in the altitude range 55–70 km. The most probable reason for the deviation



**Fig. 13.** The mean standard deviation between OSO and the satellites; absolute(left) and relative(right). MIPAS (12 + 13), SMR (v021), and the dotted SMR (v225) are from the time period 2002–2004. The vertical coverage of the satellites explains the deviating extension of the profiles. The horizontal black dashed lines show the vertical limits of the OSO observations. The dashed line at 60 km is the lower limit 2002–2004 and the dash-dotted line at 55 km is the lower limit 2004–2008. The black line is the root-sum of the average retrieval noise and the total forward model parameter variability of the OSO instrument. The summer values are excluded.

between OSO and MIPAS (12 + 13) can be the baseline features seen in the OSO spectra before 2004.

### 5.3.3 SMR

The two CO datasets of SMR deviate in different ways compared to the OSO data at 55–95 km. SMR (225) shows down to 65 % lower mixing ratios than OSO and SMR (021) shows up to 50 % higher mixing ratios (Fig. 12). A reason for the general discrepancy between SMR and OSO can be the few co-locations with OSO but this does not explain the difference between the two SMR versions. V021 is regarded to be the more accurate than v225. Comparisons between SMR (021 + 225) and ACE shows the same general discrepancy between v225 and v021 (not shown).

## 6 Summary and conclusions

Ground-based, frequency-switched measurements of mesospheric CO at 115 GHz from Onsala Space Observatory ( $57^\circ$  N,  $12^\circ$  E) during the time period 2002–2008 are presented.

Signal-reference switching is the standard microwave observation method in order to reduce the effect of gain drift in the receiver system. A frequency-switched radiometer is an especially simple instrument since almost no moving parts are needed (except a hot load flag). The advantages with frequency-switching include also that both gain nonlinearity

**Table 4.** Statistics for 55 km, 63 km and for total columns > 71 km. *Mn (%)* the mean relative difference of CO between satellite and OSO (> 0 if the satellite reports more CO than OSO), *Std (%)* the mean standard deviations, *Corr* the mean correlation of CO between satellite and OSO, *total* the total number of co-located measurements, *days* the number of days with co-located measurements. The summer values are excluded.

	55 km			63 km			> 71 km			co-locations	
	Mn	Std	Corr	Mn	Std	Corr	Mn	Std	Corr	total	days
FTS	-1	169	0.82	4	82	0.89	-22	18	0.96	148	108
MIPAS (12 + 13)	-10	88	0.72	-30	63	0.73	-	-	-	1424	194
MIPAS (200)	-3	152	0.76	9	71	0.77	-	-	-	1842	180
MLS	14	136	0.81	14	68	0.86	-24	28	0.89	19250	506
SMR (v021) < 04	13	62	0.78	4	76	0.74	42	66	0.85	22	8
SMR (v225) < 04	-13	51	0.76	-55	45	0.72	-47	15	0.73	11	6
SMR (v225) > 04	1	33	0.82	-40	39	0.75	-68	32	0.35	14	8

and gain variations are almost canceled out and that no time is spent observing a reference load. Frequency-switching is very well suited for the observation of narrow transition lines as in the case of mesospheric CO at 115 GHz.

The Optimal Estimation Method, OEM, has been used to retrieve vertical CO profiles from the measured spectra. A thorough error analysis has been performed to investigate the systematic effects due to the uncertainties in the different parameters used in the measurement and retrieval process to give an as accurate error estimation as possible.

The OSO instrument has provided the longest time series of ground-based mesospheric CO measurements so far. The OSO data show the same general features as data from satellite instruments both in the annual cycle, characterized by high CO mixing ratios during winter and very low mixing ratios during summer, and in shorter time period events.

The OSO CO data have been compared to CO datasets from four satellite instruments; ACE-FTS (v2.2) on Scisat, MIPAS (V3O\_CO\_12 + 13 and V4O\_CO\_200) on Envisat, MLS (v3-3) on Aura and SMR (v225 and v021) on Odin.

A satellite measurement is assumed to be co-located with OSO if the measurement is done the same day and if the air at the tangent point of the satellite both is within a radius of 1500 km from OSO and deviates less than 20 % in PV (potential vorticity) compared to the air above OSO.

During the time period 2004–2008 the averaged CO datasets retrieved by OSO and ACE, MLS and MIPAS (200) do not differ by more than 15 % in the altitude range 55–70 km, which is within the combined systematic errors of the different instruments (see Fig. 12b).

The time period 2002–2004 MIPAS (12 + 13) shows up to 50 % smaller mixing ratios compared to OSO. One reason for the observed difference between the OSO and MIPAS (12 + 13) mesospheric CO datasets can be due to baseline features seen in the OSO spectra before February 2004.

SMR (021 + 225) have very few co-located CO measurements with OSO. V225 shows up to 65 % lower mixing ratios than OSO and the v021 measurements show up to 50 % higher mixing ratios than OSO.

Above 70 km we compare the CO column values from OSO and the satellite sensors ACE, MLS and SMR. The OSO column values are about 25 % higher than the values from both ACE and MLS. SMR (021) shows up to 65 % higher column values than OSO. The MLS column values are close to the OSO a priori values since we use a priori information outside the vertical range of the satellite (the upper vertical limit for MLS is 80 km). SMR has very few co-located measurements with OSO.

The systematic error above 70 km is  $\pm 25$  % for ACE and  $\pm 10$  % for OSO. If the systematic errors for ACE and OSO are correctly estimated the mean true profile has to be in the range where the mean profiles of OSO and ACE (inclusive their systematic errors) overlaps. Since ACE shows 25 % lower column values than OSO, this indicates that OSO has a positive bias of less than 10 % above 70 km and that ACE has a negative bias of about 15–25 % above 70 km (see Fig. 12b). Hoffmann et al. (2011) report an offset pattern when their ground-based instrument is compared to ACE and MLS, which is similar to the offset pattern we report when OSO is compared to the same satellites. Additional comparisons of upper mesospheric CO are needed to understand the reason for this observed offset between ground-based and satellite instruments.

Observation of mesospheric CO provides important information of the mesospheric dynamics. The satellite sensors which measure mesospheric CO today are not, to our knowledge, planned to be replaced when they stop functioning. Therefore, in a few years, ground-based instruments will be even more important than today. The CO transition at 115 GHz is suitable for ground-based studies of the upper atmosphere due to both that the lower atmosphere is fairly transparent, at this frequency, and that pressure broadening exceeds Doppler broadening as high as 70 km, making it possible to estimate vertical profiles up to this altitude and to estimate column values above.

The exact CO abundance in the upper mesosphere is still an open question. Further ground-based measurements at

115 GHz can be used as a low cost alternative to clarify this issue.

**Acknowledgements.** The Swedish Natural Science Research Council supported the maintenance and development of the OSO receiver system. We thank the teams behind HITRAN, JPL and WACCM for providing a priori information to the retrievals. We thank the community behind ARTS for software used in the retrieval process. We thank ECMWF for wind field data and the teams behind MLS/Aura, MIPAS/Envisat and ACE-FTS/SCISAT for providing the satellite CO datasets. The Atmospheric Chemistry Experiment (ACE), also known as SCISAT, is a Canadian-led mission mainly supported by the Canadian Space Agency and the Natural Sciences and Engineering Research Council of Canada. We also thank the Department of Earth and Space Sciences, Chalmers University of Technology for SMR/Odin CO data. Odin is a Swedish-led satellite project funded jointly by the Swedish National Space Board (SNSB), the Canadian Space Agency (CSA), the National Technology Agency of Finland (Tekes), the Centre National d'Etudes Spatiales (CNES) in France and the European Space Agency (ESA). We thank the laboratory and workshop of Onsala Space Observatory for keeping the OSO receiver up and running. Finally we thank the reviewers for their helpful comments on the manuscript.

Edited by: R. Sussmann

## References

- Aellig, C., Kaempfer, N., and Hauchecorne, A.: Variability of mesospheric CO in the fall and winter as observed with ground-based microwave radiometry at 115 GHz, *J. Geophys. Res.*, 100, 14125–14130, doi:10.1029/95JD00984, 1995.
- Allen, D., Stanford, J., López-Valverde, M., Nakamura, N., Lary, D., Douglass, A., Cerniglia, M., Remedios, J., and Taylor, F.: Observations of middle atmosphere CO from the UARS ISAMS during the early northern winter 1991/92, *J. Atmos. Sci.*, 56, 563–583, doi:10.1175/1520-0469(1999)056<0563:OOMACF>2.0.CO;2, 1999.
- Baron, P., Ricaud, P., de La Noë, J., Eriksson, P., Merino, F., and Murtagh, D.: Studies for the Odin sub-millimetre radiometer: Retrieval methodology, *Can. J. Phys.*, 80, 341–356, doi:10.1139/P01-150, 2002.
- Bevilacqua, R., Stark, A., and Schwartz, P.: The variability of carbon monoxide in the terrestrial mesosphere as determined from ground-based observations of the  $J = 1 \rightarrow 0$  emission line, *J. Geophys. Res.*, 90, 5777–5782, doi:10.1029/JD090iD03p05777, 1985.
- Borsdorff, T. and Sussmann, R.: On seasonality of stratomesospheric CO above midlatitudes: New insight from solar FTIR spectrometry at Zugspitze and Garmisch, *Geophys. Res. Lett.*, 36, 804, doi:10.1029/2009GL040056, 2009.
- Burrows, S., Martin, C., and Roberts, E.: High-latitude remote sensing of mesospheric wind speeds and carbon monoxide, *J. Geophys. Res.*, 112, 109, doi:10.1029/2006JD007993, 2007.
- Clancy, R., Muhleman, D., and Allen, M.: Seasonal variability of CO in the terrestrial mesosphere, *J. Geophys. Res.*, 89, 9673–9676, doi:10.1029/JD089iD06p09673, 1984.
- Clerbaux, C., George, M., Turquety, S., Walker, K. A., Barret, B., Bernath, P., Boone, C., Borsdorff, T., Cammas, J. P., Catoire, V., Coffey, M., Coheur, P.-F., Deeter, M., De Mazière, M., Drummond, J., Duchatelet, P., Dupuy, E., de Zafra, R., Eddouinia, F., Edwards, D. P., Emmons, L., Funke, B., Gille, J., Griffith, D. W. T., Hannigan, J., Hase, F., Höpfner, M., Jones, N., Kagawa, A., Kasai, Y., Kramer, I., Le Flochmoën, E., Livesey, N. J., López-Puertas, M., Luo, M., Mahieu, E., Murtagh, D., Nédélec, P., Pazmino, A., Pumphrey, H., Ricaud, P., Rinsland, C. P., Robert, C., Schneider, M., Senten, C., Stiller, G., Strandberg, A., Strong, K., Sussmann, R., Thouret, V., Urban, J., and Wiacek, A.: CO measurements from the ACE-FTS satellite instrument: data analysis and validation using ground-based, airborne and spaceborne observations, *Atmos. Chem. Phys.*, 8, 2569–2594, doi:10.5194/acp-8-2569-2008, 2008.
- de Zafra, R. and Muscari, G.: CO as an important high-altitude tracer of dynamics in the polar stratosphere and mesosphere, *J. Geophys. Res.*, 109, D06105, doi:10.1029/2003JD004099, 2004.
- Dupuy, E., Urban, J., Ricaud, P., Le Flochmoën, É., Lauté, N., Murtagh, D., De La Noë, J., El Amraoui, L., Eriksson, P., Forkman, P., Frisk, U., Jégou, F., Jiménez, C., and Olberg, M.: Strato-mesospheric measurements of carbon monoxide with the Odin Sub-Millimetre Radiometer: Retrieval and first results, *Geophys. Res. Lett.*, 31, L20101, doi:10.1029/2004GL020558, 2004.
- Eriksson, P.: Analysis and comparison of two linear regularization methods for passive atmospheric observations, *J. Geophys. Res.*, 105, 18157–18167, doi:10.1029/2000JD900172, 2000.
- Eriksson, P., Jiménez, C., and Buehler, S. A.: Qpack, a tool for instrument simulation and retrieval work, *J. Quant. Spectrosc. Ra.*, 91, 47–64, doi:10.1016/j.jqsrt.2004.05.050, 2005.
- Eriksson, P., Buehler, S. A., Davis, C. P., Emde, C., and Lemke, O.: ARTS, the atmospheric radiative transfer simulator, Version 2, *J. Quant. Spectrosc. Ra.*, 112, 1551–1558, doi:10.1016/j.jqsrt.2011.03.001, 2011.
- Forkman, P., Eriksson, P., and Winnberg, A.: The 22 GHz Radio-aeronomy receiver at Onsala Space Observatory, *J. Quant. Spectrosc. Ra.*, 77, 23–42, doi:10.1016/S0022-4073(02)00073-0, 2003a.
- Forkman, P., Eriksson, P., Winnberg, A., Garcia, R., and Kinnison, D.: Longest continuous ground-based measurements of mesospheric CO, *Geophys. Res. Lett.*, 30, 1532, doi:10.1029/2003GL016931, 2003b.
- Forkman, P., Eriksson, P., and Murtagh, D.: Observing the vertical branch of the mesospheric circulation at lat N60° using ground based measurements of CO and H<sub>2</sub>O, *J. Geophys. Res.*, 110, 107, doi:10.1029/2004JD004916, 2005.
- Funke, B., López-Puertas, M., García-Comas, M., Stiller, G. P., von Clarman, T., Höpfner, M., Glatthor, N., Grabowski, U., Kellmann, S., and Linden, A.: Carbon monoxide distributions from the upper troposphere to the mesosphere inferred from 4.7 μm non-local thermal equilibrium emissions measured by MIPAS on Envisat, *Atmos. Chem. Phys.*, 9, 2387–2411, doi:10.5194/acp-9-2387-2009, 2009.
- Garcia, R. R., Marsh, D. R., Kinnison, D. E., Boville, B. A., and Sassi, F.: Simulation of secular trends in the middle atmosphere, 1950–2003, *J. Geophys. Res.*, 112, D09301, doi:10.1029/2006JD007485, 2007.

- Hedin, A. E.: Extension of the MSIS thermosphere model into the middle and lower atmosphere, *J. Geophys. Res.*, 96, 1159–1172, doi:10.1029/90JA02125, 1991.
- Hoffmann, C. G., Raffalski, U., Palm, M., Funke, B., Golchert, S. H. W., Hochschild, G., and Notholt, J.: Observation of stratospheric CO above Kiruna with ground-based microwave radiometry – retrieval and satellite comparison, *Atmos. Meas. Tech.*, 4, 2389–2408, doi:10.5194/amt-4-2389-2011, 2011.
- Kasai, Y. J., Koshiro, T., Endo, M., Jones, N. B., and Murayama, Y.: Ground-based measurement of strato-mesospheric CO by a FTIR spectrometer over Poker Flat, Alaska, *Adv. Space Res.*, 35, 2024–2030, doi:10.1016/j.asr.2005.04.099, 2005.
- Lait, L.: An alternative form for potential vorticity, *J. Atmos. Sci.*, 51, 1754–1759, doi:10.1175/1520-0469(1994)051<1754:AAFFPV>2.0.CO;2, 1994.
- Lopez-Puertas, M., Lopez-Valverde, M., Garcia, R., and Roble, R.: A review of CO<sub>2</sub> and CO abundances in the middle atmosphere, *Geoph. Monog.*, 123, 83–100, doi:10.1029/GM123p0083, 2000.
- Marks, C. and Rodgers, C.: A retrieval method for atmospheric composition from limb emission measurements, *J. Geophys. Res.*, 98, 14939–14953, doi:10.1029/93JD01195, 1993.
- Melsheimer, C., Verdes, C., Buehler, S. A., Emde, C., Eriksson, P., Feist, D. G., Ichizawa, S., John, V. O., Kasai, Y., Kopp, G., Koulev, N., Kuhn, T., Lemke, O., Ochiai, S., Schreier, F., Sreerekha, T. R., Suzuki, M., Takahashi, C., Tsujimaru, S., and Urban, J.: Intercomparison of general purpose clear sky atmospheric radiative transfer models for the millimeter/submillimeter spectral range, *Radio Sci.*, 40, RS1007, doi:10.1029/2004RS003110, 2005.
- Pickett, H., Poynter, R., Cohen, E., Delitsky, M., Pearson, J., and Müller, H.: Submillimeter, millimeter, and microwave spectral line catalog, *J. Quant. Spectrosc. Ra.*, 60, 883–890, doi:10.1016/S0022-4073(98)00091-0, 1998.
- Pumphrey, H. C., Filipiak, M., Livesey, N., Schwartz, M., Boone, C., Walker, K., Bernath, P., Ricaud, P., Barret, B., Clerbaux, C., Jarnot, R., Manney, G., and Waters, J.: Validation of middle-atmosphere carbon monoxide retrievals from MLS on Aura, *J. Geophys. Res.*, 112, D24S38, doi:10.1029/2007JD008723, 2007.
- Rodgers, C. D.: Inverse methods for atmospheric sounding: Theory and practice, World Scientific, Singapore, 2000.
- Rodgers, C. D. and Connor, B.: Intercomparison of remote sounding instruments, *J. Geophys. Res.*, 108, 4116, doi:10.1029/2002JD002299, 2003.
- Rohlfs, K. and Wilson, T. L.: Tools of Radio Astronomy, Springer-Verlag, Berlin, 2008.
- Rothman, L., Barbe, A., Chris Benner, D., Brown, L., Camy-Peyret, C., Carleer, M., Chance, K., Clerbaux, C., Dana, V., Devi, V., Devic, V., Fayt, A., Flaud, J., Gamache, R., Goldman, A., Jacquemart, D., Jucks, K., Lafferty, W., Mandin, J., Massie, S., Nemtchinov, V., Newnham, D., Perrin, A., Rinsland, C., Schroeder, J., Smith, K., Smith, M., Tang, K., Toth, R., Vander Auwera, J., Varanasi, P., and Yoshino, K.: The HITRAN molecular spectroscopic database: edition of 2000 including updates through 2001, *J. Quant. Spectrosc. Ra.*, 82, 5–44, doi:10.1016/S0022-4073(03)00146-8, 2003.
- Velazco, V., Wood, S. W., Sinnhuber, M., Kramer, I., Jones, N. B., Kasai, Y., Notholt, J., Warneke, T., Blumenstock, T., Hase, F., Murcray, F. J., and Schrems, O.: Annual variation of strato-mesospheric carbon monoxide measured by ground-based Fourier transform infrared spectrometry, *Atmos. Chem. Phys.*, 7, 1305–1312, doi:10.5194/acp-7-1305-2007, 2007.
- Waters, J., Wilson, W., and Shimabukuro, F.: Microwave measurement of mesospheric carbon monoxide, *Science*, 191, 1174, doi:10.1126/science.191.4232.1174, 1976.



Time series inversion of spectra  
from ground-based spectrometers

**Authors:**

O.M. Christensen, P. Eriksson

**Bibliography:**

O.M. Christensen, P. Eriksson. Time series inversion of spectra from ground-based spectrometers *Atmos. Meas. Tech.*, submitted, 2012.



# Time series inversion of spectra from ground-based radiometers

Ole Martin Christensen<sup>1</sup> and Patrick Eriksson<sup>1</sup>

<sup>1</sup>Department of Earth and Space Sciences, Chalmers University of Technology, Gothenburg, Sweden

**Abstract.** Retrieving time series of atmospheric constituents from ground-based spectrometers often requires different temporal averaging depending on the altitude region in focus. This can lead to several datasets existing for one instrument which complicates validation and comparisons between instruments. This paper puts forth a possible solution by incorporating the temporal domain into the maximum a posteriori (MAP) retrieval algorithm. The state vector is increased to include measurements spanning a time period, and the temporal correlations between the true atmospheric states are explicitly specified in the a priori uncertainty matrix. This allows the MAP method to effectively select the best temporal smoothing for each altitude, removing the need for several datasets to cover different altitudes.

The method is compared to traditional averaging of spectra using a simulated retrieval of water vapour in the mesosphere. The simulations show that the method offers a significant advantage compared to the traditional method, extending the sensitivity an additional 10 km upwards without reducing the temporal resolution at lower altitudes. The method is also tested on the OSO water vapour microwave radiometer confirming the advantages found in the simulation. Additionally, it is shown how the method can interpolate data in time and provide diagnostic values to evaluate the interpolated data.

## 1 Introduction

Ground-based microwave spectrometers are useful for measuring properties of the middle atmosphere due to the low tropospheric attenuation at microwave frequencies. Using these frequencies also allows the use of pressure broadening of molecular transitions to retrieve altitude profiles well into

the mesosphere (Clancy and Muhleman, 1993). Microwave instruments have, for example, provided measurements important for ozone chemistry (Parrish et al., 1981; Solomon et al., 1984), and have the ability to determine long term trends of trace constituents (Nedoluha et al., 2003).

Microwave measurements will always contain thermal noise. In order to overcome this noise, the measured atmospheric spectra must be averaged over time. This averaging increases the signal to noise ratio, but reduces the temporal resolution of the measurements. The strength of the measured emission, tropospheric attenuation, the required accuracy, and the sensitivity of the instrument determine the need for temporal averaging. Depending on which atmospheric phenomena and altitudes investigated in any single study, a specific compromise must be made between temporal resolution and noise reduction.

The use of different temporal resolutions is exemplified by the WASPAM instrument, which has used a 6 h averaging time in a case study of sudden stratospheric warming (Seele and Hartogh, 2000) as well as a 24 h averaging time to study the annual variation of water vapour around the mesopause (Seele and Hartogh, 1999). Different averaging times are used since retrievals for higher altitudes require lower thermal noise and thus longer integration times.

The ratio between the required averaging times for high and low altitudes will in large part be determined by the altitude range of the instrument. As newer instruments, such as those described in Nedoluha et al. (2011) and Bleisch et al. (2011), offer the possibility to increase this range, the differences in averaging time needed for the upper- and lowermost altitudes will increase.

Although the use of different averaging times in itself poses no problems, it does complicate the validation and cross-comparison of instruments. An example is the water vapour radiometer at the Onsala Space Observatory (OSO) (Forkman et al., 2003). This instrument has mainly used one day spectra in studies of atmospheric dynamics (Fork-

---

*Correspondence to:* Ole Martin Christensen  
ole.m.christensen@chalmers.se

man et al., 2005; Scheiben et al., 2012), whereas only a scheme with varying averaging time depending on tropospheric opacity has been cross-compared with other instruments (Haefele et al., 2009).

One way to circumvent the problem of multiple averaging times for a single dataset is to incorporate the averaging of spectra directly in the retrieval process. To achieve this, several measurements are simultaneously inverted using temporal correlation data of the quantity to be retrieved. The method is similar to the 2-dimensional retrievals for limb sounding satellites (Livesey et al., 2006; Dinelli et al., 2010). But instead of doing the retrievals in two spatial dimensions, the retrievals are performed simultaneously in altitude and time. Earlier attempts to use the temporal information in retrievals have resorted to recursive filtering (Askne and Westwater, 1986), whereas the method presented in this paper uses a non-recursive approach based on the maximum a posteriori method (Rodgers, 2000).

The study is described using the following structure. Section 2 introduces the retrieval theory, nomenclature and the time series inversion technique. In Sect. 3 we apply the time series inversion method on a simulated instrument to show the advantages of the method. Section 4 investigates the practical use of the method, and Sect. 5 discusses the computational requirements. The conclusion is given in Sect. 6.

## 2 Retrieval Methodology

### 2.1 Nomenclature

In passive atmospheric remote sensing, properties of the atmosphere are determined by analysing the radiation emitted from, and passing through, the atmosphere. This analysis is called a retrieval, or inversion, and is done by solving an inverse problem. The relationship between the measured radiation,  $\mathbf{y}$ , and the atmospheric properties is described by a forward model,  $\mathbf{y} = \mathbf{F}(\mathbf{x})$ , where  $\mathbf{x}$ , denoted as the state vector, contains the variables to be retrieved. These can include atmospheric variables at different altitudes as well as instrument variables. If the forward model is locally linear, the measurement can be expressed as

$$\mathbf{y} = \mathbf{F}(\mathbf{x}_a) + \mathbf{K}(\mathbf{x} - \mathbf{x}_a) + \epsilon, \quad (1)$$

where  $\mathbf{x}_a$  is the a priori state vector,  $\mathbf{K}$  is the Jacobian-, or weighting function matrix, defined as  $\partial\mathbf{y}/\partial\mathbf{x}$ , and  $\epsilon$  represents errors in the measurement.

The inverse problem involves finding  $\mathbf{x}$  for a given  $\mathbf{y}$ . In remote sensing, inverse problems are usually ill-posed, so the relationship between the measurement and the atmosphere is ambiguous. This means that several atmospheric states can give rise to the same measurement. To obtain sensible results, the inversion needs to be constrained through some regularisation algorithm. The regularisation in the time series inversion method is based on the maximum a posteriori

(MAP), also called optimal estimation, method. It uses statistical properties of the measurements and the atmosphere to constrain the solutions (Rodgers, 2000).

Assuming Gaussian statistics, the relationship between a set of stochastic variables is described by a covariance matrix,  $\mathbf{S}$ , in which each element,  $\mathbf{S}_{i,j}$ , is the covariance between variables  $i$  and  $j$ . If the covariance of the a priori state is given by the matrix  $\mathbf{S}_a$  and the measurement uncertainties are specified by  $\mathbf{S}_\epsilon$ , a cost-function can be expressed as

$$\chi^2 = (\mathbf{x} - \mathbf{x}_a)^T \mathbf{S}_a^{-1} (\mathbf{x} - \mathbf{x}_a) + (\mathbf{y} - \mathbf{F}(\mathbf{x}))^T \mathbf{S}_\epsilon^{-1} (\mathbf{y} - \mathbf{F}(\mathbf{x})), \quad (2)$$

where  $\mathbf{x}$  is the true state vector and  $\mathbf{x}_a$  is the a priori state vector. The state minimising this function is the maximum of the a posteriori probability density function and is given by

$$\hat{\mathbf{x}} = \mathbf{x}_a + \mathbf{G}(\mathbf{y} - \mathbf{F}(\mathbf{x}_a)), \quad (3)$$

where  $\mathbf{G}$ , the gain-matrix, is

$$\mathbf{G} = \partial\mathbf{y}/\partial\mathbf{x} = (\mathbf{K}^T \mathbf{S}_\epsilon^{-1} \mathbf{K} + \mathbf{S}_a^{-1})^{-1} \mathbf{K}^T \mathbf{S}_\epsilon^{-1}. \quad (4)$$

An alternative way of expressing equation 3 is by introducing the averaging kernel (AVK) matrix,  $\mathbf{A} = \partial\hat{\mathbf{x}}/\partial\mathbf{x} = \mathbf{G}\mathbf{K}$ . Combining Eq. 1 and 3 gives

$$\hat{\mathbf{x}} = \mathbf{x}_a + \mathbf{A}(\mathbf{x} - \mathbf{x}_a) + \mathbf{G}\epsilon. \quad (5)$$

This shows that a retrieved value, in the absence of noise, is the sum of the corresponding a priori value plus the change from the a priori state convolved with the matching row of the AVK matrix. The sum of a row in the AVK matrix is a measure of the retrieval's sensitivity to changes in the state vector and is called measurement response (Baron et al., 2002).

### 2.2 Time series inversion

For ground-based instruments using single spectrum inversions, the measurement vector,  $\mathbf{y}$ , usually holds the brightness temperature for each channel of the instrument. Thus, for an instrument with  $m$  channels, the length of  $\mathbf{y}$  is  $m$ , and similarly  $\mathbf{x}$  contains values of the state variables at the time of the measurement. The time series inversion method proposed here expands both  $\mathbf{y}$  and  $\mathbf{x}$  to include measurements from  $N$  different times. This increases the length of  $\mathbf{y}$  to  $m \cdot N$ , and the length of  $\mathbf{x}$  to  $n \cdot N$ , where  $n$  is the length of the single spectrum state vector. In a similar fashion, the Jacobian matrix,  $\mathbf{K}$ , becomes a block diagonal matrix with block elements equal to the Jacobian matrix for each mea-

surement giving

$$\mathbf{y} = \begin{pmatrix} y_1^1 \\ \vdots \\ y_m^1 \\ y_1^2 \\ \vdots \\ y_m^2 \\ y_1^3 \\ \vdots \\ y_m^N \end{pmatrix}, \mathbf{K} = \begin{pmatrix} \mathbf{K}^1 & 0 & 0 \\ 0 & \ddots & 0 \\ 0 & 0 & \mathbf{K}^N \end{pmatrix}, \mathbf{x} = \begin{pmatrix} x_1^1 \\ \vdots \\ x_n^1 \\ x_1^2 \\ \vdots \\ x_n^2 \\ x_1^3 \\ \vdots \\ x_n^N \end{pmatrix},$$

where the upper index denotes measurement number.

Since the state and measurement vectors cover several measurements, the covariance matrices in Eq. 2 must be adjusted. Assuming that the measurement uncertainties are uncorrelated between the measurements (i.e. only thermal noise),  $\mathbf{S}_\epsilon$  simply becomes a block diagonal matrix, where block  $\mathbf{S}_\epsilon^i$  corresponds to the covariance matrix from the measurement  $i$ . The uncertainties in the a priori state are, however, *not* uncorrelated between the times of the measurements. To incorporate this temporal correlation, even the non-diagonal blocks in  $\mathbf{S}_a$  must have non zero values. Thus, the covariance matrices become

$$\mathbf{S}_\epsilon = \begin{pmatrix} \mathbf{S}_\epsilon^1 & 0 & 0 \\ 0 & \ddots & 0 \\ 0 & 0 & \mathbf{S}_\epsilon^N \end{pmatrix}, \mathbf{S}_a = \begin{pmatrix} \mathbf{S}_a^{1,1} & \mathbf{S}_a^{1,2} & \dots & \mathbf{S}_a^{1,N} \\ \mathbf{S}_a^{2,1} & \mathbf{S}_a^{2,2} & \dots & \mathbf{S}_a^{2,N} \\ \vdots & \vdots & \ddots & \vdots \\ \mathbf{S}_a^{N,1} & \mathbf{S}_a^{N,2} & \dots & \mathbf{S}_a^{N,N} \end{pmatrix},$$

where  $\mathbf{S}_a^{i,j}$  is the covariance matrix corresponding to measurement  $i$  and  $j$ .

Introducing correlation between measurements in  $\mathbf{S}_a$  results in an averaging kernel matrix which contains non-zero elements in its off-diagonal blocks. The resulting matrix,

$$\mathbf{A} = \begin{pmatrix} \mathbf{A}^{1,1} & \mathbf{A}^{1,2} & \dots & \mathbf{A}^{1,N} \\ \mathbf{A}^{2,1} & \mathbf{A}^{2,2} & \dots & \mathbf{A}^{2,N} \\ \vdots & \vdots & \ddots & \vdots \\ \mathbf{A}^{1,N} & \mathbf{A}^{2,N} & \dots & \mathbf{A}^{N,N} \end{pmatrix},$$

will contain information about how much smoothing that occurs with respect to both altitude and time. Temporal smoothing occurs because the MAP method uses information from several measurements to retrieve a single profile. The amount of smoothing will partly depend on the setup of the a priori uncertainty matrix, which will be described in detail in the next section.

### 2.3 Specification of the a priori covariance matrix

The specification of the uncertainty matrices is central to MAP. Since the state vector of the time series inversions has been extended to include several measurements, both the

temporal and vertical correlation of the state variables need to be specified in  $\mathbf{S}_a$ , and it is through the latter correlation that the MAP method can take into account results from adjacent measurement times when retrieving a profile.

The correlation between state variables can be conveniently described with a correlation function combined with a correlation length. We will use an exponential function to describe correlations. This means that for state vector variables related in altitude (e.g. species concentration), the correlation coefficient between the variable at altitude  $z_k$  and  $z_p$  for measurement  $i$  will be given by  $\rho_z(\mathbf{x}_k^i, \mathbf{x}_p^i) = \exp(-|z_k - z_p|/l_c)$ , where  $l_c$  denoted as the correlation length, meaning the length at which the correlation has dropped to  $1/e$ . In a similar fashion the correlation of a variable in time can be represented by  $\rho_t(\mathbf{x}_k^i, \mathbf{x}_k^j) = \exp(-|t^i - t^j|/t_c)$ , where  $t^i$  ( $t^j$ ) is the time of measurement  $i$  ( $j$ ) and  $t_c$  is the temporal correlation length. Assuming that the correlation is independent in the two dimensions (separable), the total correlation is calculated as the product of  $\rho_z$  and  $\rho_t$ . In this study we also assume that the a priori covariance is stationary, so that it is can be described by the same matrix at all measurement times.

The a priori covariance matrix of the investigated variable should represent both the uncertainty arising from natural variability and the uncertainty of the a priori mean value (Eriksson, 2000). The latter uncertainty arises from a limited knowledge of the atmospheric mean state. These two terms have quite different correlations. In general, the error in the mean value of the state variable should be characterised by longer vertical correlation length and a smaller standard deviation than the natural variability. An additional, and more important, feature for inverting the time series is that errors in the mean will be correlated over long temporal periods compared to the natural variability. If, for example, the assumed a priori value for the concentration of one atmospheric species is too high with respect to the true mean at one time, it is likely that it will remain too high for a considerable time (weeks, months, etc.) thereafter.

We will use the retrieval of water vapour in the mesosphere as an example of the time series inversion method. Figure 1 shows covariance matrices used to describe the a priori water vapour profile in the retrievals. In Fig. 1a and 1b the vertical and temporal covariance of the concentration of water vapour at 60 km are shown. The dashed-green curve represents the natural variability of water vapour, which is given a standard deviation of 50 %, a vertical correlation length of 4 km, and a temporal correlation length of 12 h.

As mentioned earlier, the correlation lengths of the uncertainty in the a priori mean are different from the natural variability. The red-dot-dashed curve in Fig. 1 shows properties of a covariance matrix set to represent the uncertainty in the a priori mean. The matrix has a standard deviation of 20 % and a correlation length of 8 km in altitude and 7 days in time. By adding both the natural variability and the a priori mean uncertainty, the complete covariance matrix, described by the

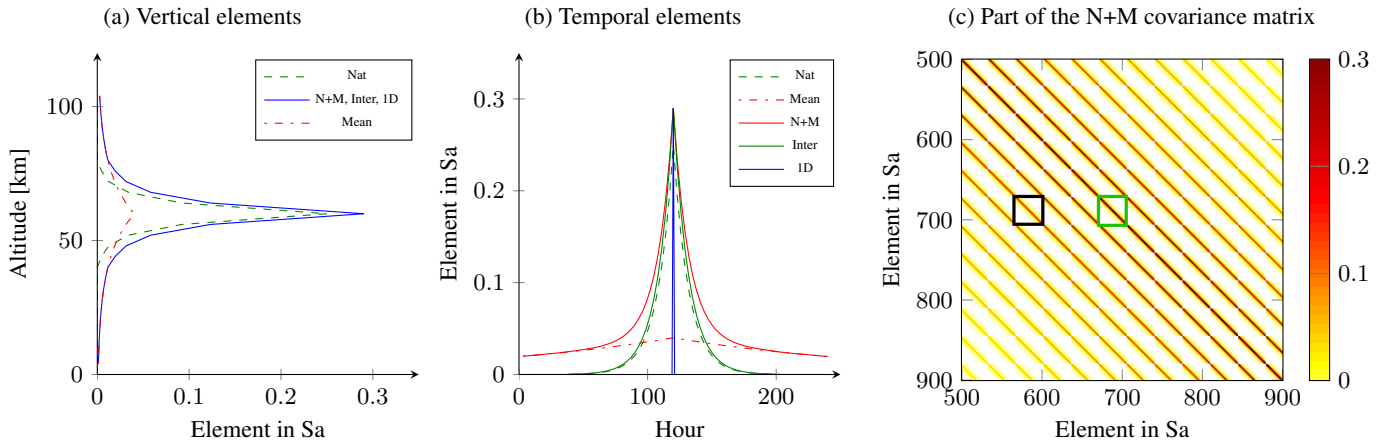


Fig. 1: The covariance matrices used for the a priori information on water vapour. Plot (a) depicts the temporal and (b) the vertical elements of the covariance matrix. The matrices represent natural variability (Nat), uncertainty in a priori mean (Mean), the sum of natural variability and uncertainty in mean (N+M), single spectrum inversions (1D) and an intermediate covariance matrix (Inter). The structure of the N+M a priori covariance matrix is shown in plot (c). A diagonal matrix block is highlighted by the green square and an off-diagonal block is highlighted by the black square.

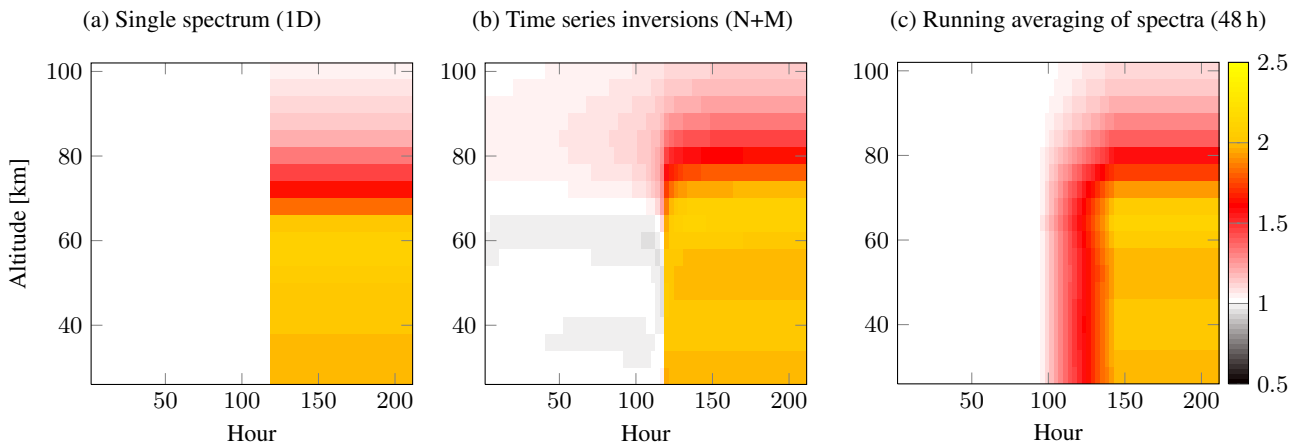


Fig. 2: Retrieved concentration of water vapour, relative to a priori, from the simulated retrievals. Plot (a) is from the single spectrum (1D) inversions, plot (b) from the retrievals using the time series inversion method with the N+M covariance matrix, and (c) is from the retrievals using spectra averaged over 48 h.

solid-red line, is obtained. A selected number of elements from the complete  $\mathbf{S}_a$  matrix are shown in Fig. 1c. The block structure, explained in Sect. 2.1, is indicated by the green and black squares. The diagonal block (green square) represents the covariance within a measurement time, whereas the off-diagonal block (black square) represents the variance scaled with the correlation between measurement times.

The result from the time series retrievals will depend on the temporal correlation used. To investigate this, a second covariance matrix is created which assumes that the entire a priori uncertainty has a temporal correlation of only 12 h, but with the same standard deviation (54 %) and vertical correlation length as the total covariance matrix. This matrix is described by the solid-green line in Fig. 1b. For comparison, inversions are also performed with zero correlation in time (blue curve) to mimic single spectrum (1D) retrievals. Though these retrievals could be done on each spectrum separately, it is chosen, for comparison purposes, to perform the retrievals simultaneously using the same formalism as the time series inversions. This is achieved by using a block diagonal a priori covariance matrix in the retrievals.

A retrieval using the traditional method of averaging spectra is also performed by doing a 48 h running mean over the simulated spectra. However, the expected variance in a 48 h mean is different from that expected in a 3 h mean, so, to correctly specify the covariance of these inversions, the N+M covariance matrix is projected onto a 48 h grid following Rodgers (2000, Ch. 10.3.1.1). This results in an a priori standard deviation of 36 %, which is a decrease from the 54 % for the 3 h measurements.

### 3 Theoretical test case

#### 3.1 The simulation and retrievals

In order to test the time series inversion method, a model scenario is set up. The simulation and retrievals are done with the radiative transfer simulator ARTS (v.2.0) and the retrieval toolkit Qpack (Eriksson et al., 2005, 2011). The simulated instrument is designed to mimic the 22 GHz radiometer currently operating at OSO, but some simplifications are made to illustrate the more general use of this method. Most notably, the bandwidth is increased from 20 MHz to 1 GHz and the noise temperature is reduced from 170 K to around 100 K. The instrument backend is simulated using 83 channels, each 25 kHz wide and unevenly distributed across the bandwidth of the instrument. At the line-centre, a distance of 25 kHz between the channels is used. This is increased further away from the centre, reaching 100 MHz at the band edges. The calibration used is a beam switching method.

Spectra from ground-based radiometers are often corrected for tropospheric loss before retrievals are performed. To model this, the simulated instrument is located above the troposphere (15 km) and the thermal noise level is doubled.

This represent a tropospheric transmission of 0.5, which, together with the loss of observational time due to the beam switching, leads to an effective noise temperature of 400 K, which is used to specify  $\mathbf{S}_e$ . Additionally, the thermal noise in the system is left uncorrelated between the channels, and the integration time is set to 3 h. Note that no thermal noise is added to the actual spectra, but only used to specify the covariance matrix.

The simulated atmosphere is created by extracting temperature and water vapour profiles for the 25<sup>th</sup> of February from the MSIS (Hedin, 1991) temperature database and a climatology based on retrieved water vapour over OSO from AURA-MLS. The spectroscopic parameters for the water vapour line at 22 GHz are taken from the JPL-catalogue (Pickett et al., 1998) (line strength and position) and HITRAN 2004 database (Rothman et al., 2005) (broadening parameters).

The retrieval of water vapour is done on an altitude grid ranging from 4 km to 104 km with a grid resolution of 4 km. The covariance matrices used are the same as specified in Sect. 2.3 with  $\mathbf{S}_e$  being a pure diagonal matrix and  $\mathbf{S}_a$  having a correlation in both altitude and time.

#### 3.2 Response to a unit change

The MAP inversion method combines information from measurements at several times, this makes the temporal characteristics of the retrieved profiles of particular interest. To investigate these temporal characteristics, we run a test scenario in which water vapour in the atmosphere is kept constant, equal to the a priori, until the 120<sup>th</sup> hour and then suddenly doubled.

The results of the retrievals are shown in Fig. 2. The single spectrum inversions (Fig. 2a) have no errors before the increase. Afterwards, the retrievals will only change at certain altitudes determined by the measurement response. At the highest levels, the retrieved value remains 1, i.e. equal to a priori, due to the lack of measurement response, whereas the at lower altitudes the retrieved values reflect the true atmosphere.

The conventional way to increase the measurement response at high altitudes is by averaging spectra in order to reduce the influence of thermal noise. Figure 2c shows results from the 48 h averaging of spectra. An improvement around 70 km can be seen for measurements later than 24 h after the unit change. This however, comes at the cost of smoothing out the step increase in time. Figure 2b shows that this smoothing can be avoided (for low altitudes) by applying the time series inversion method. Just as with the traditional averaging, the response around 70 km improves after the increase compared to the single spectrum inversions. However, the high temporal resolution is maintained at lower altitudes, and the abrupt change can clearly be seen in the retrievals. Thus, by inverting the entire time series simultaneously, temporal resolution can be maintained at the lower altitudes while the sensitivity at higher altitudes is increased.

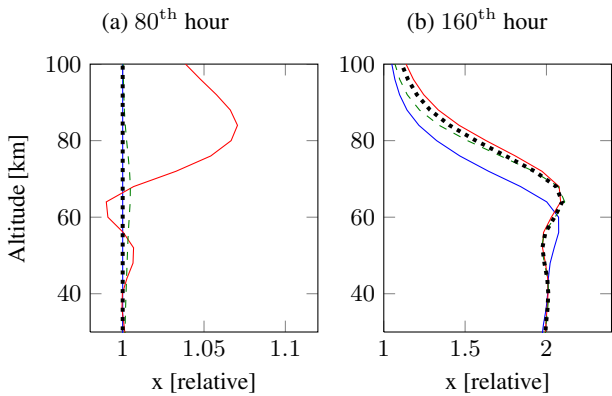


Fig. 3: Retrieved water vapour profiles (relative to the a priori) from the simulated retrievals. The different curves represent the single spectrum inversions (blue), the time series inversions using the N+M (red line) and the intermediate covariance matrix (dashed-green), and the inversions using the averaged spectra (black-dashed). Plot (a) is the retrieved profile at the 80<sup>th</sup> hour, when the true profile is equal to the a priori. Plot (b) is the retrieved profile at the 160<sup>th</sup> hour, after the step-increase, when the true profile is double that of the a priori.

The increase in sensitivity is seen more clearly in Fig. 3b, which shows the profiles at the 160<sup>th</sup> hour. Both the traditional method of averaging spectra (dotted-black) and the time series inversions (red and dashed-green line) show a significant improvement above 60 km. The long temporal correlation in the a priori mean uncertainty does, however, lead to a large temporal smoothing at high altitudes seen by the increased water vapour above 70 km in the red line in Fig. 3a. The time series inversion method also leads to some oscillatory patterns shown by the negative values around 60 km in Fig. 3a.

### 3.3 Retrieval diagnostics

The temporal and vertical resolution of the inversions can be explored further by analysing the AVK matrices. Selected elements of the AVK matrices are shown in Fig. 4. The single spectrum inversions (Fig. 4a) give an AVK matrix which is completely diagonal with respect to time (at 3 h time resolution), meaning that the matrix is a block diagonal matrix where the non-zero elements are confined to elements no further away from the diagonal than the number of elements in the single measurement state vector. If correlation between the days is introduced (Fig. 4b), the blocks adjacent to the diagonal block become non-zero and fall off exponentially from the diagonal. This implies that a smoothing occurs in the temporal dimension, as already shown in Sect. 3.2. For direct averaging of the spectra (Fig. 4c) the AVK elements are constant across all blocks inside the averaging time, albeit

reduced with a factor 1/16 compared to the single spectrum inversion to account for the averaging.

The averaging kernels are the rows of the AVK matrix. For clarity, it is convenient to focus on some particular elements of the rows. The first are the elements which corresponds to the  $n$  columns around the diagonal, where  $n$  is the number of elements in the single spectrum state vector. These represent the vertical averaging kernel for each altitude. These kernels are seen in the second row of Fig. 4. The vertical averaging kernels for the three inversions are quite similar. Most notable is the reduction of the values that occurs for the 48 h averaging, but this is compensated by the kernels spanning a larger number of measurements. Time series inversion produces vertical averaging kernels that have smaller negative values for elements within the same measurement compared to single spectrum inversions, but it should be noted that elements corresponding to different altitudes and different times can be negative (black areas in Fig. 4b).

The temporal averaging kernels describe the smoothing in time and are given by the elements corresponding to the same altitude for different times. These are shown in the third row of Fig. 4. The single spectrum inversions have Dirac delta function kernels. The time series inversions have averaging kernels showing how the retrieval takes values from adjacent measurements into account. The lower values at the wings show how the inversions put diminishing weight measurements further away. For the averaging of spectra, the temporal AVKs have a constant value over the averaging time and zero elsewhere.

The full width at half maximum (FWHM) of the AVKs in the different dimensions can be used to roughly describe the resolution of the inversion in those dimensions. Figure 5a shows the FWHM of the temporal AVKs. The single spectrum inversions (blue curve) and the inversions averaging over spectra (black-dashed curve) have a constant temporal resolution across all the altitudes corresponding to their respective averaging times. The red and the dashed-green curves show the FWHM from the time series inversions. These inversions have a temporal FWHM which varies with altitude. At lower altitudes the FWHM is close to 3 h, i.e. the same as the single spectrum inversions. At higher altitudes the AVKs become wider indicating a reduction of temporal resolution as more information from adjacent measurements are used in the retrievals. Also, the larger a priori correlation between days of the N+M matrix (red curve) compared to the intermediate (green curve) matrix results in wider AVKs. It is this wider averaging time at higher altitudes that allows the time series inversions to extend the retrievals higher than the single spectrum inversions.

There is some limitation in using only the FWHM to describe the resolution, as it does not take into account the full shape of the AVKs. The FWHM will have a different meaning for different shapes. For example, the FWHM in the temporal dimension of 48 h averaged retrievals will define where the averaging is cut off. For the exponentially-shaped

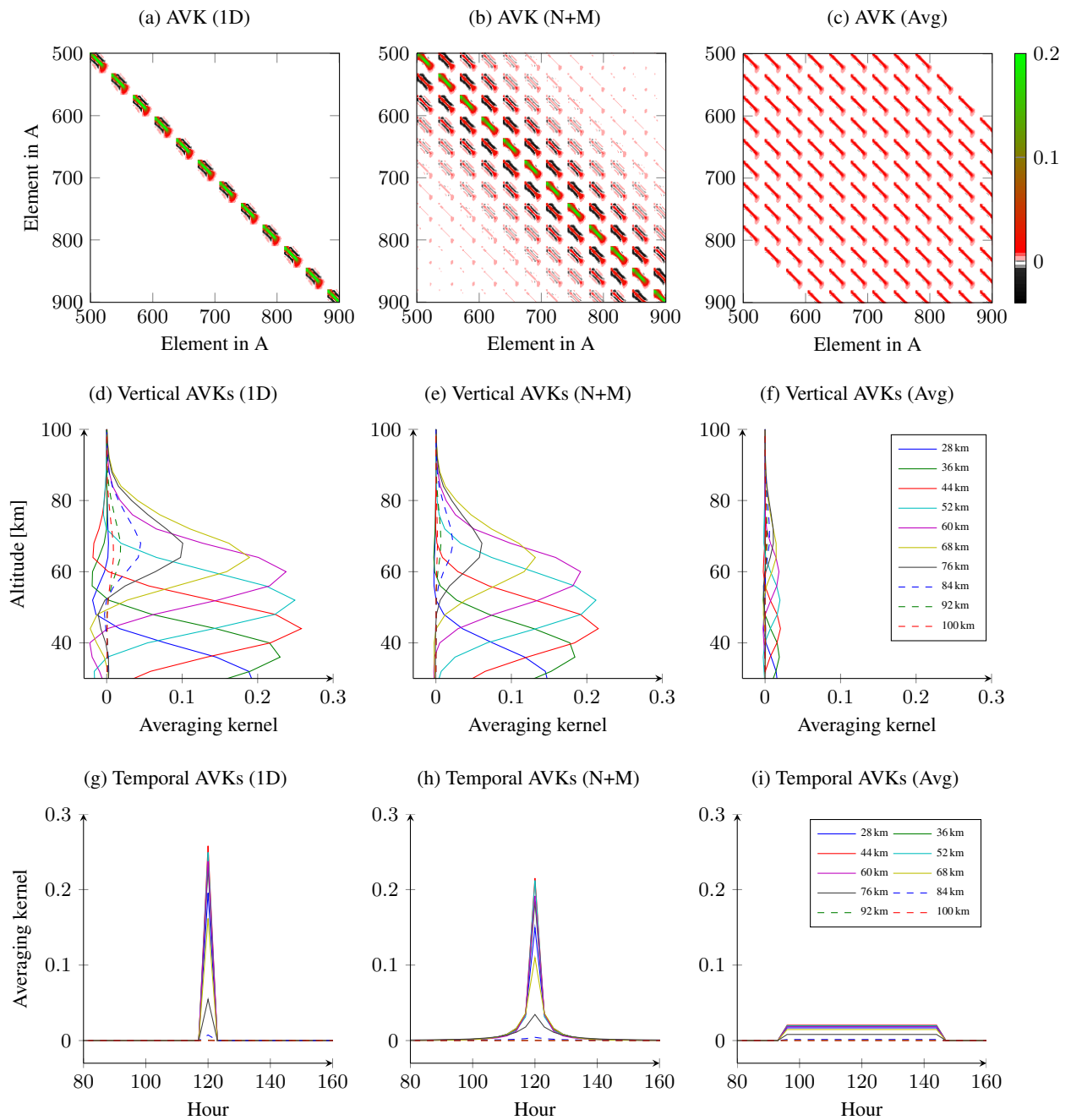


Fig. 4: Selected elements of the averaging kernels for the theoretical test case. The first row (a-c) shows the structure of the AVK matrices of single spectrum retrieval (left), time series retrieval with the N+M a priori uncertainty matrix (centre) and 48 h averaging of spectra (right). The second row (d-f) shows vertical AVKs for the respective cases and the third row (g-i) temporal AVKs for the respective cases. For the vertical and temporal averaging kernels each of the curves corresponds to different altitudes.

temporal AVKs of the time series inversions, however, the retrievals can have significant contributions from measurements beyond the FWHM. This explains why the time series inversion shows more temporal smoothing above 80 km in Fig. 2, yet, it has a smaller temporal FWHM in 5a.

Figure 5b shows the FWHM of the vertical AVKs. The FWHM is more or less the same for the inversions except for the 48 h averaging over spectra where the reduced noise in the measurements results in a better vertical resolution. Once again some care should be taken when comparing the

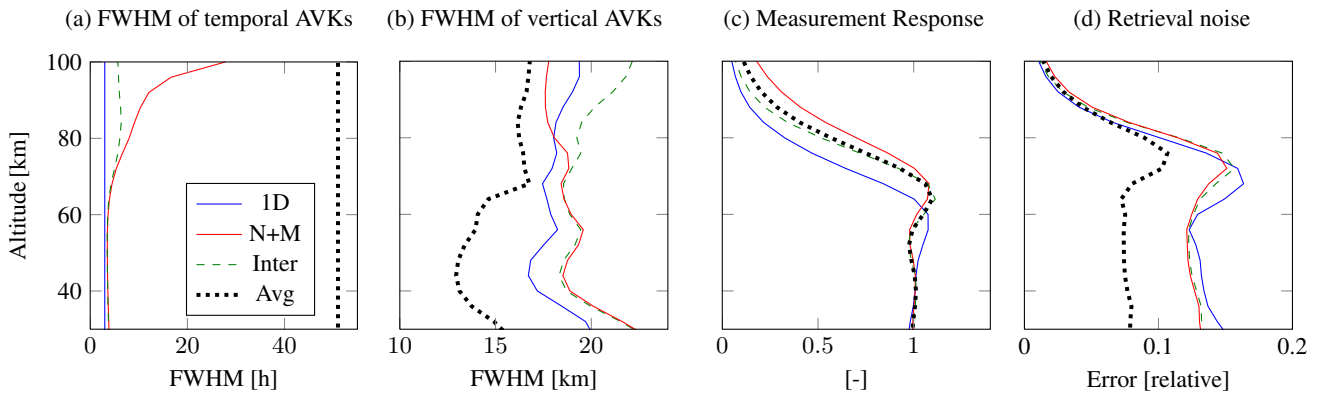


Fig. 5: Properties of the simulated retrievals at the the 120<sup>th</sup> hour. Plot (a) is the FWHM of the temporal AVKs, plot (b) is the FWHM of the vertical AVKs, plot (c) is the measurement response from the retrievals, and plot (d) is the retrieval noise from the retrievals in units relative to a priori concentration. The different curves represent the single spectrum inversions (blue), the time series inversions using the N+M (red) and the intermediate covariance matrix (dashed-green), and the inversions using the averaged spectra (black-dashed).

FWHM from the different inversions. In particular, the negative lobes seen in the 1D inversions will not be accounted for, and thus, AVKs with weaker lobes, like those from the time series inversions, will have a larger FWHM, though this mainly comes from the removal of the lobes, and not a decrease in vertical resolution.

The measurement response corresponds, as anticipated, to the observed changes when  $x$  is doubled (Fig. 3b). The measurement response for the different inversions shows once again that the time series inversion method enables the retrieval of atmospheric values up to roughly the same altitude as the traditional averaging over spectra, actually exceeding the traditional averaging when using the N+M covariance matrix.

Retrieval noise describes the error in the retrieved profiles from thermal noise, and is calculated as  $\mathbf{GS}_\epsilon \mathbf{G}^T$  (Rodgers, 2000). Figure 5d shows the square root of the diagonal elements of the retrieval noise matrix. As anticipated, the reduction of thermal noise in the measurements from the traditional averaging method (black-dashed line) will result in a lower retrieval noise compared to the single spectrum inversions (blue line). This is the result of both a reduction in the thermal noise due to averaging and the change from using a different a priori uncertainty. The retrieval noise in the time series inversions ends up a bit below the single spectrum inversions. This shows that some error reduction is achieved with the time series method, but that the main improvement it offers is the increased measurement response at high altitudes.

In addition to the diagonal elements, the retrieval noise covariance matrix will have non-diagonal elements arising from temporal and vertical correlations. This means that the retrieval noise for the time series inversions has a correlation in time *even though* the underlying thermal noise is uncor-

related in time. The FWHM of this correlation (not shown) can be different from that of the AVKs. For the time series inversions (N+M), it is roughly 15 h up to around 70 km, above this it increases and reaches 50 h at 85 km. For the intermediate a priori covariance matrix inversions, the temporal FWHM of the retrieval noise stays at around 15 h for all altitudes.

#### 4 Test using a real instrument

To illustrate the practical use of the time series inversion method, we invert atmospheric spectra measured from the water vapour radiometer at OSO. When using real measurements, instrument related issues might degrade the efficiency of the retrieval, or introduce biases, which complicates the retrievals and error analysis.

##### 4.1 OSO-radiometer

The radiometer used to test the time series inversion method is placed at OSO (57.4°N, 12°E). It measures water vapour at 22.235 GHz with a resolution of 25 KHz and bandwidth of 20 MHz. The system has an uncooled HEMT frontend and uses a 800 channel autocorrelator backend. Receiver temperature is estimated to 170 K and the calibration is done by a hot-cold calibration and beam switching. The spectra are also corrected for tropospheric absorption. Each spectrum consists of 5 min measurements averaged together into six 3 h-intervals for each day, 00-03, 04-07, 08-11, 12-15, 16-19 and 20-23. The averaging is done so that measurements with lower noise values have a larger weight in the average. The thermal noise of each 3 h spectrum is determined separately by fitting a 3<sup>rd</sup> order polynomial to one of the line-wings and calculating the standard deviation of the residual.

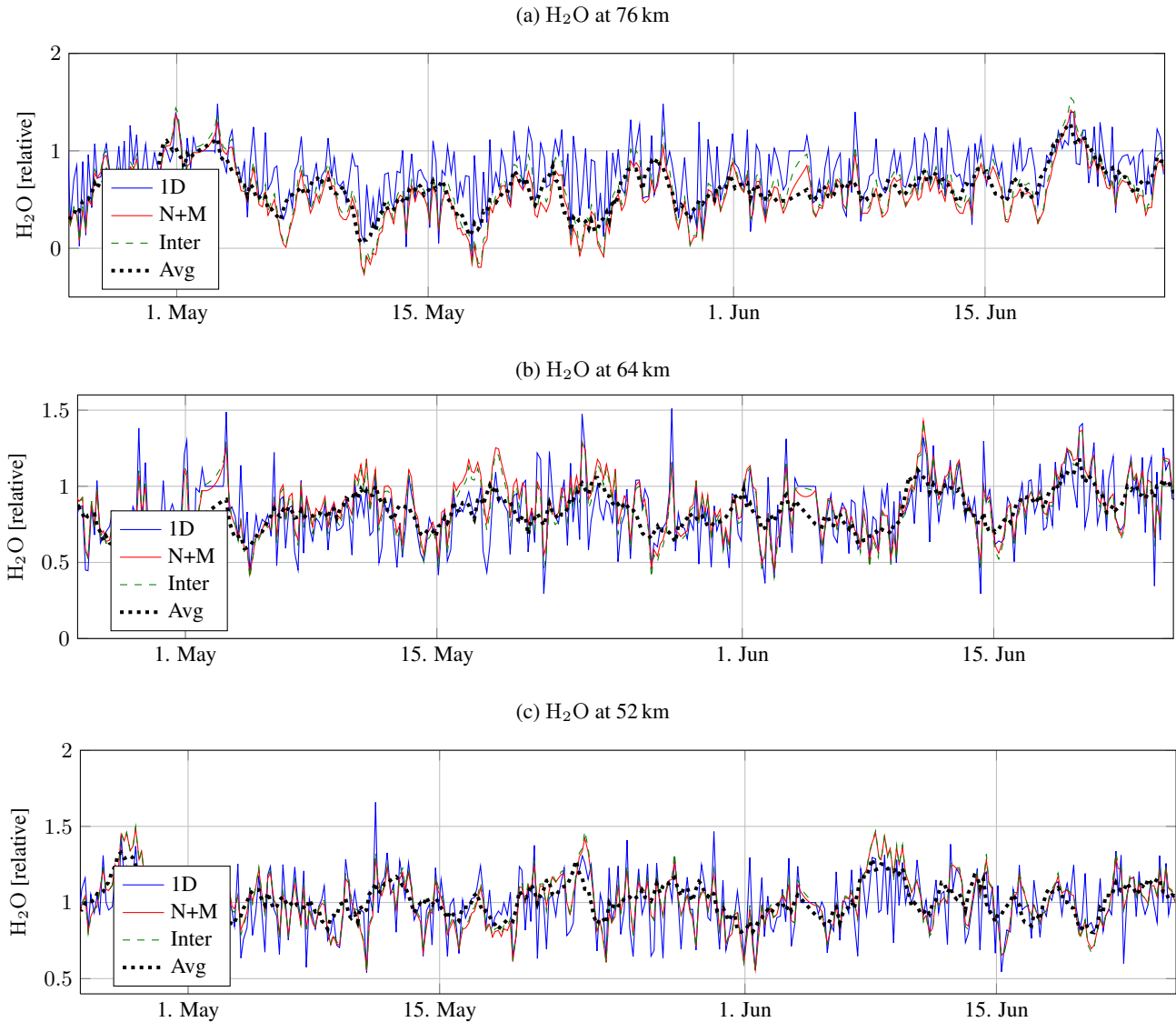


Fig. 6:  $\text{H}_2\text{O}$  retrievals from the summer of 2005 obtained by the OSO radiometer. The result is relative to the a priori concentration and are shown for 76 km (a), 64 km (b) and 52 km (c). The different curves represent the single spectrum inversions (blue), the time series inversions using the N+M (red) and the intermediate covariance matrix (dashed-green), and the inversions using the averaged spectra (black-dashed).

When performing the time series inversions over all days<sup>460</sup> and all channels, the retrieval matrices become large. To reduce the size of the matrices, only a sub-sample of the channels is selected, as in the theoretical test case. In the line-centre, all channels are used, but at the line-wings, the channel separation is increased gradually, reaching 620 kHz<sup>465</sup> at the far ends. In total, 83 of the 800 channels are used. Furthermore, the retrievals are performed in 30 day intervals. To minimise edge effects each interval has a 10 day overlap,<sup>470</sup> which allows for 5 days on each end of the retrieval intervals to be removed. These intervals are then combined to create the complete time series. Further discussion regarding the computational demands can be found in Sect. 5.

Just as in the theoretical test case, the retrievals are performed on each 3 h spectrum separately, with the time series inversion method, and a 48 h moving average of spectra. However, since the thermal noise in the measurements varies with time, the simple averaging is replaced with a weighted average giving measurements with lower noise more weight. In addition, since some gaps exist in the measurements, some 48 h averages have fewer measurements than the nominal 12.

The inversions are set up as described in Sect. 3, except that since the noise level varies with time, the thermal noise in each measurement must be estimated from each corresponding spectrum rather than having a constant noise level as in Sect. 3.3. Additionally, an instrumental baseline

(5<sup>th</sup> order polynomial) is retrieved with a priori uncertainties from 10 K (0<sup>th</sup> order) to 2 K (5<sup>th</sup> order). Since the atmosphere over OSO changes over time, the a priori is also set to vary according to the climatologies (temperature and water vapour) in Sect. 3, rather than have a constant value.

## 4.2 Dealing with measurement gaps

The OSO time series has periods where no measurement data could be recorded. These periods are mainly caused by rain. Data gaps create additional problems when handling measurement series. A time interpolation using neighbouring retrieved data requires the user to select an interpolation strategy (nearest, linear, spline . . .), as well as to make subjective judgements on the validity of these interpolated values based on experience and knowledge of the atmospheric variables measured.

The time series inversion method provides an elegant solution to this problem. To obtain values at the gaps,  $\mathbf{x}$  is expanded to cover the times where measurements are lacking. This increases the size of  $\mathbf{x}$  to  $n \cdot (N + N')$ , where  $N'$  is the number of missing measurements ( $n$ ,  $N$ , and later  $m$  are defined as in Sect. 2.2). The expansion of  $\mathbf{x}$  allows the MAP algorithm to retrieve the missing values, maintaining a consistent inversion methodology over the complete time period.

Since the size of  $\mathbf{x}$  is increased, the number of columns in  $\mathbf{K}$  must increase correspondingly. This gives  $\mathbf{K}$  a size of  $N \cdot m \times (N + N') \cdot n$ . The elements in the  $N'$  extra columns will be zero as no measured spectra exists for this time in  $\mathbf{y}$ . Physically this is equivalent to only using a virtual measurement of the a priori atmosphere at the time of the data gap. However, this does not mean that only a priori information is used for the retrieval of corresponding state. Since  $\mathbf{S}_a$  contains information about the temporal correlation of the atmosphere, the MAP method will automatically use information from neighbouring measurement to “optimally” estimate  $\mathbf{x}$  at the time of the measurement gap.

For an “interpolated” value, the amount of information taken into account from nearby measurements is given by the corresponding measurement response. The measurement response will depend on the a priori uncertainty matrix used and the amount of noise in the adjacent measurements. For the single spectrum inversions the measurement response will be zero at the interpolated values, whereas for the time series inversions it will increase with increasing a priori temporal correlation. The measurement response will provide a value on which the validity of the interpolated value can be determined. This value is based on the underlying statistical properties of the retrievals, and thus a consistent selection scheme can be applied, for example, by only using data points above a certain measurement response threshold (e.g. 0.8).

## 4.3 Result from time series inversions

Retrievals from the OSO instrument were done for the entire measurement period (2002-2012). For comparison of the different inversions methods, an example period from end of April to end of June 2005 was selected for further study as this period offers a long set of continuous measurements, with few measurement gaps. The results of the retrievals at three different altitudes are shown in Fig. 6. These results include estimated values where data gaps occur (13 of 368 times), interpolated using the method discussed in Sect. 4.2.

By comparing the single spectrum retrievals (blue curve) to the retrieval of 48 h averaged spectra (black-dashed curve), the effect of the averaging can be seen. The variability is reduced from  $1\sigma \sim 0.22$  in the single spectrum inversions to  $1\sigma \sim 0.15$  in the averaged ones, with the averaged spectra having a longer temporal correlation. This correlation has two causes. The first one is the temporal correlation of the atmospheric changes over the instrument, the other cause is the thermal noise which, as discussed earlier, will also have a correlation in time when averaging is performed. In addition to the change in variability, the averaged spectra show a clearer deviation from the a priori at higher altitudes. This shows the effect of the increased measurement response at these altitudes.

The time series inversions (red and dashed-green curves) show an increased measurement response at higher altitudes similar to the 48 h averaged inversions, and the variation is correlated over several days. The more longer-term averages, over a couple of days, seems to follow the averaged inversions. At 76 km the measured mean over the entire period is actually lower than the a priori mean concentration. This illustrates why it is important to include the uncertainty in the a priori mean in the inversions. Without this part, the measurement response would be lower and the inversions would not reveal this information. At lower altitudes (52 and 64 km), the time series inversions preserve many of the short-term variations, indicating a high temporal resolution at these altitudes.

It is hard to distinguish whether the short term variations are a result of noise in the instrument or natural variance in the atmosphere. However, the main point of these retrievals is not to determine the true water vapour concentration in the atmosphere, but rather to show that the time series inversions produce similar results to the single spectrum inversions at lower altitudes while reproducing the result from the averaged inversions higher up.

## 4.4 Averaging kernels

Since the thermal noise in the real measurements varies with time, the AVKs vary as well. Thus, to study some typical AVKs, three dates are selected for further inspection. Figure 7 shows the magnitude of the thermal noise in each of the measurements from the time series in Fig. 6, and the se-

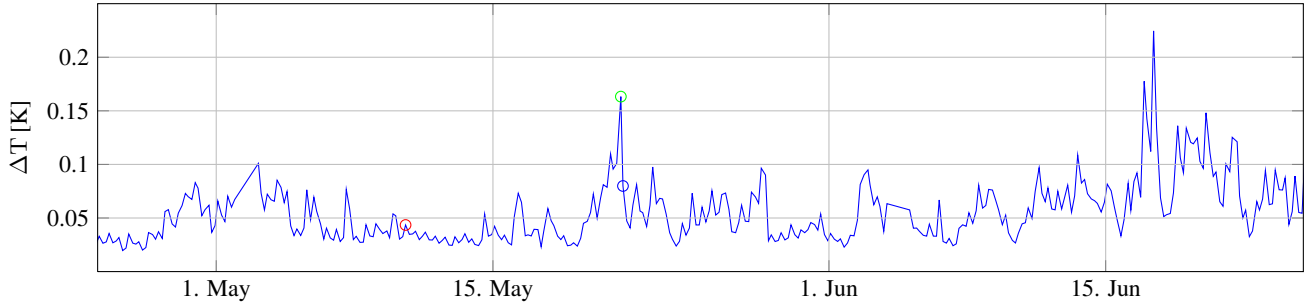


Fig. 7:  $1\sigma$  of the thermal noise from the OSO radiometer from the summer of 2005, estimated as described in the text. The measurements are performed with 3 h integration time. The circles show the three days selected for further AVK analysis.

575 lected measurements are marked by the three circles. The 615  
 first measurement (2005-05-10, red circle) is from a mea-  
 surement with a low noise value. The second (10 May 2005,  
 green circle) and third measurement (10 May 2005, blue circle)  
 are separated by only four hours and have a high and  
 580 intermediate thermal noise value respectively. 620

The measurement response of the three measurements is  
 shown in the top row of Fig. 8. The measurement response  
 of the low noise measurement is similar to the theoretical test  
 case above 60 km. Below 60 km the measurement response  
 585 starts declining due to the fitting of the instrumental baseline  
 polynomials. The similarity above 60 km is not surprising  
 considering that the noise of the measurement is 0.043 K, 625  
 which resembles the noise in the test case of 0.037 K. The  
 two other cases, however, have much higher noise than the  
 test case with values of 0.16 K and 0.07 K. This results in a  
 590 very low measurement response for single spectrum inver-  
 sions, but the time series inversions and the averaged spectra  
 still have a good measurement response between 55-75 km. 630

The amount of information taken from each measurement  
 595 is given by the temporal averaging kernels shown in the sec-  
 ond row of Fig. 8. However, unlike the averaging kernels  
 from the theoretical test case, the temporal averaging kernels  
 635 are not smoothly exponentially-declining (see Fig. 4),  
 but vary depending on the weight placed on each adjacent  
 measurement. This variation comes from the fact that the  
 MAP method puts a lower weight on noisier measurements.  
 In fact, the temporal averaging kernels from the measure- 640  
 ment with intermediate noise (Fig. 8f) show that the inver-  
 sion hardly weighs in the noisy measurement from 3 h ear-  
 605 lier at all. In the high noise case (Fig. 8e), it can be seen  
 that the adjacent measurement is actually weighted more than  
 the central measurement, as the AVK has its peak displaced  
 645 from the centre.

The last row of Fig. 8 shows the FWHM of the temporal  
 610 AVKs. For the low noise measurement (Fig. 8g) the FWHM  
 is similar to the theoretical test case above 60 km having a  
 minimum width at around 60 km before increasing in width 650  
 with increasing altitude. For the measurements with higher  
 noise, however, the irregular shape of the temporal AVKs

means that the interpretation of the FWHM is not as straight-  
 forward as in the theoretical case. The maximum might not  
 be centred at zero, and the position of the half-value point  
 might even be ambiguous. As a result the FWHM of the  
 temporal AVKs from these measurements (Fig. 8h, 8i) dif-  
 600 fers quite a lot from the theoretical test case, especially for  
 the high noise case where it fluctuates at lower altitudes.

## 5 Computational demands

Though there are several advantages of expanding the in-  
 versions into the temporal dimension, a drawback is the in-  
 creased computational demand. The computational demand  
 includes both larger memory usage and the increased number  
 of CPU operations required for the matrix operations. This  
 paper will not go into detail on optimising the efficiency of  
 the retrievals, but a discussion of the major issues is required.

Depending on the retrieval setup, either  $\mathbf{K}$ ,  $\mathbf{S}_\epsilon$  or  $\mathbf{S}_a$  will  
 have the largest memory demand. All three matrices tend  
 to be diagonal heavy (i.e. highest values around the diag-  
 onal), thus considerable memory can be saved storing them  
 as sparse matrices. For  $\mathbf{S}_a$ , this could require some cut-off  
 value for the covariance, as the exponential correlation theo-  
 605 retically never reaches zero.

Considering CPU cycles, the linear algebra can be op-  
 timised for either  $n < m$  (n-form) or  $n > m$  (m-form)  
 (Rodgers, 2000), where  $n$ ,  $m$  (and later  $N$ ) are defined in  
 Sect. 2.2. For the retrievals in this paper  $n < m$ , and the  
 most demanding operations are the calculation of  $\mathbf{K}^T \mathbf{S}_\epsilon^{-1} \mathbf{K}$ ,  
 which scales as  $N^3 n^2 m$ ,  $\mathbf{S}_a^{-1}$ , and  $(\mathbf{K}^T \mathbf{S}_\epsilon^{-1} \mathbf{K} + \mathbf{S}_a^{-1})^{-1}$ ,  
 which both scales as  $N^3 n^3$ .

The available computational power limits the size of  $N$ ,  $n$ ,  
 and  $m$ . In the retrievals from the OSO radiometer,  $N$  is limited  
 to measurements from 30 consecutive days ( $N \sim 180$ ).  
 To limit  $m$ , we use a simple solution of only selecting a 83  
 channel subset of the 800 channels in the spectrometer. Other  
 methods makes it possible to take advantage of all the chan-  
 nels while keeping down the size of  $m$ . These might be as  
 straightforward as binning channels at the line wing, i.e. av-  
 eraging the channels together to reduce the noise, or more

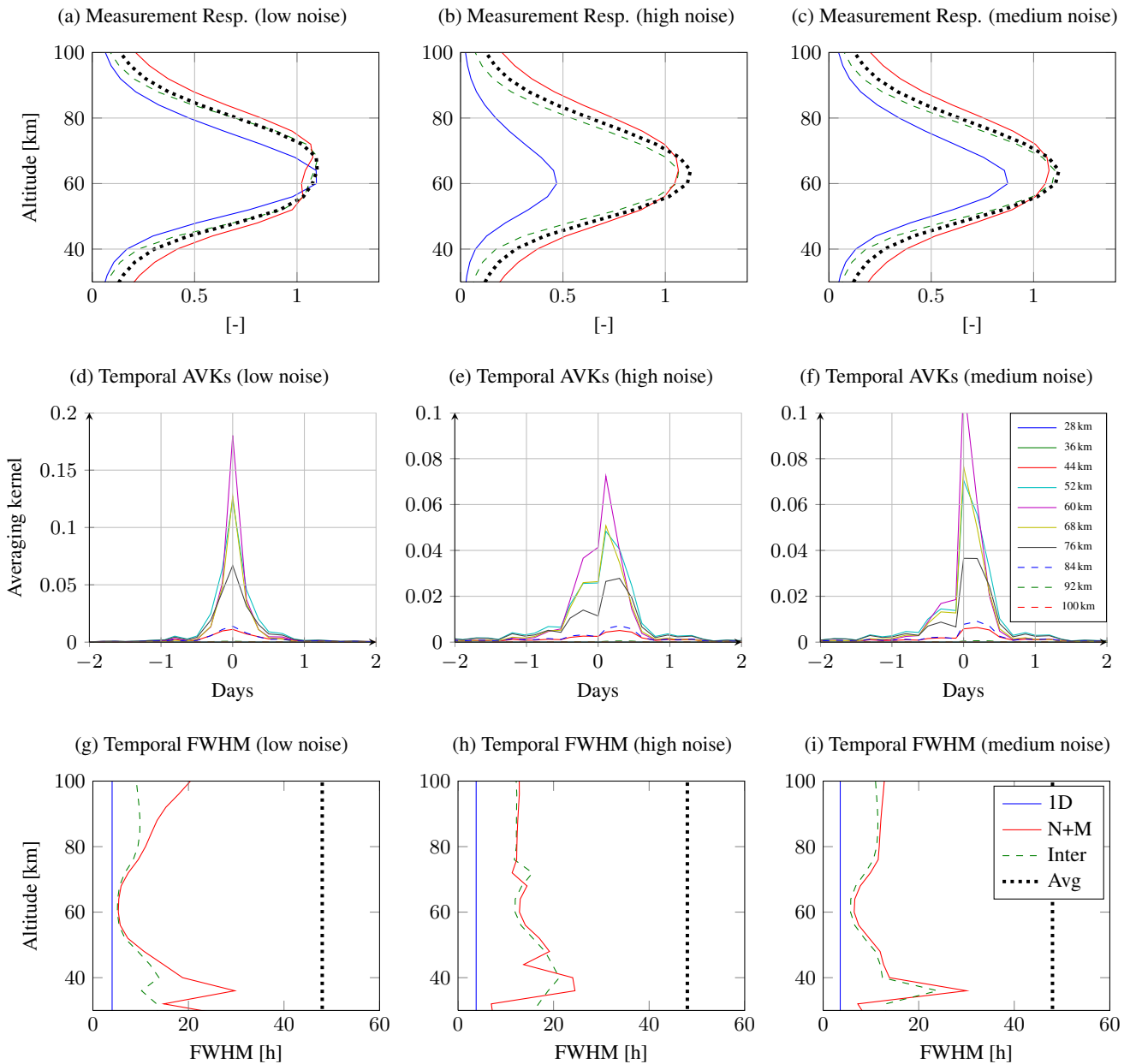


Fig. 8: Properties of the AVKs from three selected measurements from the OSO radiometer. The left column shows the low noise measurement (10 May 2005), the centre column shows the high noise measurement (21 May 2005), and the right column shows the intermediate noise measurement (21 May 2005). The first row (a-c) depicts the measurement response of the respective measurements, the second row (d-f) temporal averaging kernels of different altitudes, and the third row (g-i) the FWHM of the temporal AVKs. The different curves in the first and last row represent the single spectrum inversions (blue), the time series inversions using the N+M (red) and the intermediate covariance matrix (dashed-green), and the inversions using the averaged spectra (black-dashed).

advanced data reduction methods based on eigenvector expansions (e.g. Eriksson et al. (2002)).

655

In addition to reducing the size of the matrices, the algebra itself can be optimised. In particular, the inversion of  $(\mathbf{K}^T \mathbf{S}_\epsilon^{-1} \mathbf{K} + \mathbf{S}_a^{-1})$  can be avoided by solving Eq. 3 directly

660

using methods such as Cholesky decomposition (Livesey et al., 2006) or the Iterative Bi-conjugate Gradient method (Redburn et al., 2000).

Data reduction algorithms and optimisation of the linear algebra might indeed improve the practical use of the time

series inversion methods, but a thorough discussion of such optimisation is beyond the scope of this paper as it will be highly dependent on the specific retrieval setup and needs.

## 6 Discussion and Conclusion

This paper presents a method for inverting time series data from ground-based instruments by extending the retrieval method into the temporal dimension. This is done by directly specifying the correlation of the atmosphere in time to achieve “optimal averaging” at all altitudes. The implications and analysis of the temporal averaging kernels are discussed thoroughly in the paper, including their importance and limitations in describing the temporal resolutions of the retrievals.

To investigate the effect of using different temporal correlations, the time series inversions are performed with two different a priori matrices: one modelled to represent a realistic a priori uncertainty (N+M), and one intermediate matrix with shorter temporal correlation. Interestingly enough, in both the simulated retrievals (Fig. 5c) and the practical example (Figs. 8a, 8b, and 8c), the retrieval using the intermediate covariance matrix shows almost the same increase in measurement response between 60 and 80 km as the retrievals using the realistic covariance matrix. This is confirmed as the difference in the retrieved data from the OSO radiometer between the two matrices (Fig. 6) is minuscule below 80 km.

The similar increase in measurement response for both matrices shows that the major improvement of the time series inversions comes from the basic step of extending the inversions into the temporal dimension rather than to specify the covariance matrix in detail. This is important for the practical use of the method since it means that the method can be applied to cases where the temporal correlation is unknown, or hard to specify using Gaussian statistics.

The practical demonstration of the method retrieves 10 years of water vapour data from the OSO radiometer. This takes less than 24 h to do on a normal desktop computer. The relatively short processing time shows that the computational demands of the method, though higher than for single spectrum inversions, are not insurmountable. For large scale retrievals, however, further optimisation might be advantageous, in particular, the data reduction method for reducing the size of the measurement vector can easily be improved.

The practical inversions also show how the time series method can be used to interpolate data to times where no measurements are performed. The interpolation is carried out directly during the retrieval. It is based on the same underlying a priori statistics of the atmosphere, and it automatically takes into account the quality of the nearby measurements. By using the measurement response, a selection of the valid interpolated values can be made. This selection is consistent with the retrieval, and removes the need for ad hoc, post-processing selection algorithms to fill data gaps.

Some earlier studies have also used the temporal dimension in the retrievals, in particular, the AURA-MLS retrieval of ‘noisy’ products (Livesey et al., 2006) is similar to the time series method suggested here. The difference is that, whereas the MLS retrievals invert all spectra simultaneously into *one* mean profile over the entire time period, the time series inversions uses the MAP method to determine the optimal averaging period and produce a complete time series.

The advantages of using the time series inversion technique will depend on the instrument and species studied. This paper has focused on water vapour retrieval from a microwave radiometer, but the method will similarly benefit instruments retrieving other species such as O<sub>3</sub>, or using other methods, such as FTIR. Another useful applications of the method is the retrieval of several species, or atmospheric variables requiring different averaging times.

An additional, interesting aspect of the approach is the possibility to also consider time correlations of instrument variables. For example, the practical test case used here included the retrieval of polynomial coefficients to describe “baseline ripple”. The a priori variability of these coefficients are set to be the same, independent of integration time, and uncorrelated between measurements. However, if the temporal correlation of baseline changes is determined, it can be incorporated in time series inversion. This would result in an extension of the measurement response downwards compared to retrievals using a single spectrum or 48 h averaged spectra.

The time series inversion technique offers several advantages over traditional averaging. In particular it offers a way to produce a single consistent dataset from retrievals that span a wide set of altitudes, optimising the temporal resolution at each altitude. This removes the need for multiple datasets for variables requiring different integration times.

*Acknowledgements.* We would like to thank Peter Forkman for providing measurement data from the OSO water vapour radiometer and Marston Johnston for valiantly proofreading the manuscript.

## References

- Askne, J. and Westwater, E.: A review of ground-based remote sensing of temperature and moisture by passive microwave radiometers, *IEEE Trans. Geosci. Remote Sensing*, pp. 340–352, 1986.
- Baron, P., Ricaud, P., de La Noë, J., Eriksson, P., Merino, F., and Murtagh, D.: Studies for the Odin sub-millimetre radiometer: Retrieval methodology, *Can. J. Phys.*, 80, 341–356, 2002.
- Bleisch, R., Kämpfer, N., and Haeefele, A.: Retrieval of tropospheric water vapour by using spectra of a 22 GHz radiometer, *Atmos. Meas. Tech.*, 4, 1891–1903, doi:10.5194/amt-4-1891-2011, 2011.
- Clancy, R. T. and Muhleman, D. O.: Ground-based microwave spectroscopy of the earth’s stratosphere and mesosphere, in: *Atmospheric remote sensing by microwave radiometry*, edited by Janssen, M. A., pp. 335–381, John Wiley, 1993.

- Dinelli, B. M., Arnone, E., Brizzi, G., Carlotti, M., Castelli, E., Magnani, L., Papandrea, E., Prevedelli, M., and Ridolfi, M.: The MIPAS2D database of MIPAS/ENVISAT measurements retrieved with a multi-target 2-dimensional tomographic approach, *Atmos. Meas. Tech.*, 3, 355–374, doi:10.5194/amt-3-355-2010, 2010.
- Eriksson, P.: Analysis and comparison of two linear regularization methods for passive atmospheric observations, *J. Geophys. Res.*, 105, 18 157–18 167, doi:10.1029/2000JD900172, 2000.
- Eriksson, P., Jiménez, C., Bühler, S., and Murtagh, D.: A Hotelling transformation approach for rapid inversion of atmospheric spectra, *J. Quant. Spectrosc. Radiat. Transfer*, 73, 529 – 543, doi:10.1016/S0022-4073(01)00175-3, 2002.
- Eriksson, P., Jiménez, C., and Bühler, S. A.: Qpack, a general tool for instrument simulation and retrieval work, *J. Quant. Spectrosc. Radiat. Transfer*, 91, 47 – 64, doi:10.1016/j.jqsrt.2004.05.050, 2005.
- Eriksson, P., Bühler, S., Davis, C., Emde, C., and Lemke, O.: ARTS, the atmospheric radiative transfer simulator, version 2, *J. Quant. Spectrosc. Radiat. Transfer*, 112, 1551 – 1558, doi:10.1016/j.jqsrt.2011.03.001, 2011.
- Forkman, P., Eriksson, P., and Winnberg, A.: The 22 GHz radio-aeronomy receiver at Onsala Space Observatory, *J. Quant. Spectrosc. Radiat. Transfer*, 77, 23 – 42, doi:10.1016/S0022-4073(02)00073-0, 2003.
- Forkman, P., Eriksson, P., and Murtagh, D.: Observing the vertical branch of the mesospheric circulation at lat N60° using ground based measurements of CO and H<sub>2</sub>O, *J. Geophys. Res.*, 110, 107, doi:10.1029/2004JD004916, 2005.
- Haefele, A., Wachter, E. D., Hocke, K., Kämpfer, N., Nedoluha, G. E., Gomez, R. M., Eriksson, P., Forkman, P., Lambert, A., and Schwartz, M. J.: Validation of ground-based microwave radiometers at 22 GHz for stratospheric and mesospheric water vapor, *J. Geophys. Res.*, 114, 305, doi:10.1029/2009JD011997, 2009.
- Hedin, A. E.: Extension of the MSIS thermosphere model into the middle and lower atmosphere, *J. Geophys. Res.*, 96, 1159–1172, doi:10.1029/90JA02125, 1991.
- Livesey, N., Van Snyder, W., Read, W., and Wagner, P.: Retrieval algorithms for the EOS Microwave limb sounder (MLS), *IEEE Trans. Geosci. Remote Sensing*, 44, 1144 – 1155, doi:10.1109/TGRS.2006.872327, 2006.
- Nedoluha, G., Bevilacqua, R., Gomez, R., Hicks, B., Russell III, J., and Connor, B.: An evaluation of trends in middle atmospheric water vapor as measured by HALOE, WVMS, and POAM, *J. Geophys. Res.*, 108, 1821–1835, doi:10.1029/2002JD003332, 2003.
- Nedoluha, G., Gomez, R., Hicks, B., Helmboldt, J., Bevilacqua, R., and Lambert, A.: Ground-based microwave measurements of water vapor from the midstratosphere to the mesosphere, *J. Geophys. Res.*, 116, 309, doi:10.1029/2010JD014728, 2011.
- Parrish, A., De Zafra, R., Solomon, P., Barrett, J., and Carlson, E.: Chlorine oxide in the stratospheric ozone layer: Ground-based detection and measurement, *Science*, 211, 1158–1161, doi:10.1126/science.211.4487.1158, 1981.
- Pickett, H., Poynter, R., Cohen, E., Delitsky, M., Pearson, J., and Muller, H.: Submillimeter, millimeter, and microwave spectral line catalog, *J. Quant. Spectrosc. Radiat. Transfer*, 60, 883–890, 1998.
- Redburn, W. J., Siddans, R., Kerridge, B., Bühler, S., von Engeln, A., Eriksson, P., Kuhn-Sander, T., Künzi, K., and Verdes, C.: Critical assessments in millimetre-wave atmospheric limb sounding, Tech. rep., ESTEC Contract No 13348-98-NL-GD., 2000.
- Rodgers, C.: Inverse methods for atmospheric sounding: Theory and practice, World Scientific, Singapore, 2000.
- Rothman, L., Jacquemart, D., Barbe, A., Chris Benner, D., Birk, M., Brown, L., Carleer, M., Chackerian, C., et al.: The HITRAN 2004 molecular spectroscopic database, *J. Quant. Spectrosc. Radiat. Transfer*, 96, 139–204, 2005.
- Scheiben, D., Straub, C., Hocke, K., Forkman, P., and Kämpfer, N.: Observations of middle atmospheric H<sub>2</sub>O and O<sub>3</sub> during the 2010 major sudden stratospheric warming by a network of microwave radiometers, *ACP*, 12, 7753–7765, doi:10.5194/acp-12-7753-2012, 2012.
- Seele, C. and Hartogh, P.: Water vapor of the polar middle atmosphere: Annual variation and summer mesosphere conditions as observed by ground-based microwave spectroscopy, *Geophys. Res. Lett.*, 26, 1517–1520, doi:10.1029/1999GL900315, 1999.
- Seele, C. and Hartogh, P.: A case study on middle atmospheric water vapor transport during the February 1998 stratospheric warming, *Geophys. Res. Lett.*, 27, 3309–3312, doi:10.1029/2000GL011616, 2000.
- Solomon, P., de Zafra, R., Parrish, A., and Barrett, J.: Diurnal variation of stratospheric chlorine monoxide: a critical test of chlorine chemistry in the ozone layer, *Science*, 224, 1210–1214, doi:10.1126/science.224.4654.1210, 1984.